

## Durham Research Online

---

### Deposited in DRO:

21 November 2018

### Version of attached file:

Accepted Version

### Peer-review status of attached file:

Peer-reviewed

### Citation for published item:

Yang, L.M. and Song, S.G. and Su, L. and Allen, M.B. and Niu, Y.L. and Zhang, G.B. and Zhang, Y.Q. (2019) 'Heterogeneous oceanic arc volcanic rocks in the South Qilian Accretionary Belt (Qilian Orogen, NW China).', *Journal of petrology*, 60 (1). pp. 85-116.

### Further information on publisher's website:

<https://doi.org/10.1093/petrology/egy107>

### Publisher's copyright statement:

This is a pre-copyedited, author-produced PDF of an article accepted for publication in *Journal of petrology* following peer review. The version of record Yang, L.M., Song, S.G., Su, L., Allen, M.B., Niu, Y.L., Zhang, G.B. Zhang, Y.Q. (2019). Heterogeneous oceanic arc volcanic rocks in the South Qilian Accretionary Belt (Qilian Orogen, NW China). *Journal of Petrology* 60(1): 85-116 is available online at: <https://doi.org/10.1093/petrology/egy107>.

### Additional information:

## Use policy

---

The full-text may be used and/or reproduced, and given to third parties in any format or medium, without prior permission or charge, for personal research or study, educational, or not-for-profit purposes provided that:

- a full bibliographic reference is made to the original source
- a [link](#) is made to the metadata record in DRO
- the full-text is not changed in any way

The full-text must not be sold in any format or medium without the formal permission of the copyright holders.

Please consult the [full DRO policy](#) for further details.



Draft Manuscript for Review

## Heterogeneous oceanic arc volcanic rocks in the South Qilian Accretionary Belt (Qilian Orogen, NW China)

Journal:	<i>Journal of Petrology</i>
Manuscript ID	JPET-Jun-18-0063.R1
Manuscript Type:	Original Manuscript
Date Submitted by the Author:	n/a
Complete List of Authors:	Yang, Liming; Peking University Song, Shuguang; Peking University, Department of Geology Su, Li; China University of Geosciences, Allen, Mark; University of Durham, Earth Sciences Niu, Yaoling; The University of Durham, Earth Sciences Zhang, Guibing; Peking University, Zhang, Yuqi; Peking University
Keyword:	intra-oceanic arc, ankaramite, boninite, sanukite, mantle metasomatism by subducted sediments, zircon Hf-O isotope, Qilian Orogen

SCHOLARONE™  
Manuscripts

**Heterogeneous oceanic arc volcanic rocks in the South  
Qilian Accretionary Belt (Qilian Orogen, NW China)**

Liming Yang<sup>1</sup>, Shuguang Song<sup>1\*</sup>, Li Su<sup>2</sup>, Mark B. Allen<sup>3</sup>, Yaoling Niu<sup>2,3</sup>, Guibin  
Zhang<sup>1</sup>, Yuqi Zhang<sup>1</sup>

<sup>1</sup> MOE Key Laboratory of Orogenic Belt and Crustal Evolution, School of Earth and  
Space Sciences, Peking University, Beijing 100871, China

<sup>2</sup> Institute of Earth Sciences, China University of Geosciences, Beijing 100083, China

<sup>3</sup> Department of Earth Sciences, Durham University, Durham DH13LE, UK

MS for *Journal of Petrology*

Corresponding author:

\*Shuguang Song

E-mail: [sgsong@pku.edu.cn](mailto:sgsong@pku.edu.cn)

## ABSTRACT

Primitive arc magmas in oceanic island arcs are probes of sub-arc magmatic processes and are crucial for understanding oceanic subduction. We report an Early Paleozoic oceanic arc volcanic complex in the Lajishan-Yongjing terrane, South Qilian Accretionary Belt (SQAB), Qilian Orogen, with zircon U-Pb dating and Hf-O isotopes, mineral and whole-rock geochemistry, and Sr-Nd isotope compositions. New zircon ages focused on ~455-440 Ma constrain the timing of arc volcanism and the subduction of the Qilian Ocean. Based on petrography and bulk-rock composition, five lithological types have been identified, including (1) ankaramite, (2) high-Mg basaltic andesite, (3) high-Al andesite, (4) boninite, and (5) sanukite. The volcanic sequence thus is one of the few island arcs where three types of simultaneous near-primitive arc rocks including boninite, ankaramite and sanukite have been produced. All these rocks have variously enriched Sr-Nd isotopic compositions, positive to slight negative zircon  $\varepsilon_{\text{Hf}}(t)$  values and elevated zircon  $\delta^{18}\text{O}$  values. Boninites, ankaramites and sanukites are interpreted as contemporary, near-primitive, melts generated from different sources and conditions within an island arc setting. Boninites are characterized by low Ti, REE concentrations and high Cr# chrome spinel, and are interpreted as melts of refractory, Cpx-poor, spinel lherzolite or harzburgite with >25% degree of partial melting. Anomalous zircon  $\delta^{18}\text{O}$  values of 6.57‰-7.61‰ and Sr-Nd mixing calculations suggest less than 2% incorporation of subducted oceanic sediments into their mantle source. The ankaramites are characterized by low  $\text{SiO}_2$ , high MgO (Mg#), Cr, Ni and La/Yb ratios, and have

41 similar isotopic ratios to tectonically-adjacent OIB lavas. The ankaramite lavas are  
42 likely to have derived from mantle sources similar to those of OIB, i.e.,  
43 pyroxenite-bearing garnet peridotite enriched in incompatible elements. High-Mg  
44 basaltic andesites and high-Al andesites may be derived from the parental ankaramite  
45 magma. Sr-Nd-Hf isotopic mixing modeling constrain the amount of silicic melt to  
46 ~1-4% for ankaramite magma. Sanukites are of andesitic-dacitic composition with  
47 high Mg#, Cr and Ni, and enriched LILE and high La/Yb ratios. They are interpreted  
48 as having been generated by reaction of mantle peridotite with a silicic melt, itself  
49 derived from subducted sediments. Enriched Sr-Nd-Hf isotopic compositions  
50 constrain the amount of silicic melts to ~10-15% for sanukite. Large compositional  
51 variations among the volcanic rocks from the same arc reflect heterogeneous mantle  
52 sources and variable degrees of mantle metasomatism by sediment-derived hydrous  
53 fluids or silicic melts, accompanied by secondary AFC processes during ascent to the  
54 surface.

55 The generation of the island arc volcanic sequence in the Lajishan-Yongjing  
56 Terrane is a response to the collision between the Lajishan-Yongjing Oceanic Plateau  
57 (recorded by the Lajishan-Yongjing Ophiolite) and the pre-existing trench/continental  
58 margin. Evolution from a continental margin in the North Qilian Accretionary Belt to  
59 an oceanic island-arc in the SQAB records subduction advance and retreat in the  
60 history of the Qilian Ocean.

61  
62 **Key words:** intra-oceanic arc; ankaramite; boninite; sanukite; mantle metasomatism

by subducted sediments; zircon Hf-O isotope; Qilian Orogen

## INTRODUCTION

In the modern Earth, volcanic arc systems at convergent plate margins can be subdivided into (1) island arcs (e.g. Western Pacific-type Izu-Bonin-Mariana (IBM) oceanic arc) and (2) continental arcs, according to the different types of overriding plate (Gill, 1981). If the overriding plate is oceanic, resulting magmatism forms an island arc, possibly with primitive arc magmas, including primitive andesites (e.g. Kelemen et al., 2003), arc picrites (e.g. Rohrbach et al., 2005), island-arc ankaramite (e.g. Barsdell & Berry, 1990) and boninites (e.g. Crawford et al., 1989). If the overriding plate is continental, the resulting magmatism is typically more evolved, with calc-alkaline/alkaline rocks and less tholeiitic/low-K series volcanic rocks than island arcs (Miyashiro, 1974; Song et al., 2013).

Erupted primitive arc magmas in island arcs are in principle probes of sub-arc mantle sources (Falloon & Danyushevsky, 2000; Green et al., 2004; Mitchell & Grove, 2015), providing direct evidence of sub-arc magmatic processes (Greene et al., 2006). However, a major obstacle to our understanding the sources of island arc magmas is the effect of crustal evolution on volcanic products (Leeman, 1983). In this regard, primitive arc volcanic rocks are extremely useful, whether they occur in modern arcs or ancient island arcs preserved within continents by orogeny and accretion (e.g. Stern et al., 2012; Takashima et al., 2002; Greene et al., 2006).

Subduction accretionary belts in continental orogens record ancient subduction and

84 orogenic process by accretion of microcontinents, oceanic crust (e.g. oceanic plateau,  
85 seamounts), arc magmatic complexes and finally continent-continent collision. The  
86 most abundant petrotectonic assemblage preserved in accretionary orogens is  
87 dominated by the continental arc, with subordinate oceanic terranes (arcs, crust,  
88 mélangé, Large Igneous Provinces, etc.) and older, reworked crust (Condie, 2014). As  
89 most of the juvenile crust in orogens is found in continental arc assemblages produced  
90 during closure of the ocean-basin, Subduction Accretionary Belts play an important  
91 role in directly understanding continental growth and assembly in the Earth's history  
92 (Cawood et al., 2009).

93 The Lajishan-Yongjing Terrane in the middle part of South Qilian Accretionary Belt  
94 is an Early Paleozoic subduction accretionary belt, formed by accretion of ophiolite,  
95 island arc volcanic complexes and intrusion of arc-related plutons (Yang et al., 2002;  
96 Xiao et al., 2009; Yan et al., 2012, 2015; Fu et al., 2014; Wang et al., 2016; Zhang et  
97 al., 2017; Song et al., 2017). Ophiolites in this region are composed of picrites,  
98 ocean-island alkaline and tholeiitic lava, and have been demonstrated to be an oceanic  
99 plateau which was the product of a mantle plume (Zhang et al., 2017; Song et al.,  
100 2017). As subduction proceeded, the oceanic plateau arrived at, then jammed the  
101 trench and finally accreted to the existing continents as an ophiolitic component (Niu  
102 et al., 2003, 2017). Thus, the accretionary complexes provide us with an opportunity  
103 to reveal the tectonic relationship between the collision of an oceanic plateau and  
104 generation of an intra-oceanic arc volcanic complex.

105 In this paper, we examine various rock types of island arc affinity from the

1  
2  
3  
4 106 Lajishan-Yongjing Terrane, and provide an integrated investigation of in situ zircon  
5  
6 107 U-Pb dating and Hf-O isotopes, in combination with mineral and whole-rock  
7  
8 108 chemistry and Sr-Nd isotopes. The aims are to: (1) describe an Early Paleozoic  
9  
10 109 oceanic arc embedded in an ancient continental orogenic belt; (2) characterize the  
11  
12 110 magmatic processes of the volcanic rocks, and place constraints on the nature of  
13  
14 111 parental magmas; (3) precisely date the volcanic rocks of the island arc complex; and  
15  
16 112 (4) decipher its tectonic relations with the collision between the Lajishan-Yongjing  
17  
18 113 Oceanic Plateau and the Central Qilian Continental Margin.  
19  
20  
21  
22  
23

## 24 114 **GEOLOGICAL SETTING**

25  
26  
27 115 The Qilian-Qaidam Orogenic Belt is a wide orogenic collage, with its width  
28  
29 116 exceeding 300 km, presently located on the northern margin of the Tibetan Plateau  
30  
31 117 and adjacent areas, including the Qaidam Basin to the south, the Tarim Basin to the  
32  
33 118 northwest, and the Alax block to the northeast (Fig. 1a). It is offset by the Altyn Tagh  
34  
35 119 fault in the west and merges with the East Kunlun Orogen to the east, and continues  
36  
37 120 farther to the east merging with the Qinling-Dabie orogenic belt (Song et al., 2013,  
38  
39 121 2017). This whole region consists of two subparallel oceanic-type accretionary belts  
40  
41 122 and one continental-type ultrahigh-pressure metamorphic (UHPM) belt, occurring  
42  
43 123 between two Precambrian blocks. From north to south, the Qilian-Qaidam Orogenic  
44  
45 124 Belt can be subdivided into 5 tectonic units, the North Qilian Accretionary Belt  
46  
47 125 (NQAB), the Central Qilian Block, the South Qilian Accretionary Belt (SQAB), the  
48  
49 126 Quanji-Oulongbuluke Block and the North Qaidam UHPM Belt (Fig. 1b; Song et al.,  
50  
51  
52  
53  
54  
55  
56  
57  
58  
59  
60



127 2014).

128 The NQAB is an elongate, NW-trending orogenic belt that lies between the Alax  
129 Block (north) and the Central Qilian Block (south). It is offset by the strike slip Altyn  
130 Tagh Fault for up to 400 km in the northwest (Zhang et al., 2001) and is bounded by  
131 the Longshoushan Fault to the Alax Block. This belt is considered as a material record  
132 of a typical oceanic-type subduction-zone in the early Paleozoic that consists of two  
133 ophiolite suites with zircon U-Pb ages of 560-450 Ma, arc magmatic sequences  
134 including intermediate-felsic volcanic rocks (510-450 Ma) and I-type  
135 granite/granodiorite plutons (510-420 Ma), and high-pressure/low-temperature  
136 (HP/LT) metamorphic rocks with metamorphic ages of 490-440 Ma (Wu et al., 1993;  
137 Liu et al., 2006; Song et al., 2006, 2009, 2013; Zhang et al., 2007). A boninitic  
138 sequence (517-490 Ma) in the back-arc setting was also determined by Xia et al.  
139 (2012).

140 The Central Qilian Block between the NQAB and the SQAB consists mainly of  
141 Paleoproterozoic granitic gneiss, leucogranite and rapakivi granites with  
142 Neoproterozoic granitic intrusions, which has affinities in the geochronological  
143 spectrum of magmatism and rock assemblages with the Yangtze block (Wan et al.,  
144 2001; Gehrels et al., 2003; Song et al., 2010, 2012; 2014; Tung et al., 2007, 2013).

145 The SQAB occurs as discontinuous, NW-SE oriented fault-bounded slivers along  
146 the south margin of Central Qilian Block, and is separated from the  
147 Quanji-Oulongbuluke blocks by thick (more than 5 km) and wide (exceeding 100 km)  
148 Paleozoic sedimentary sequences (Song et al., 2014). It mainly consists of, from NW

to SE, the Yanchiwan Terrane, the Gangcha Terrane, the Lajishan-Yongjing Terrane and the Yongjing Terrane, and extends further east to the West Qinling and East Qinling, collectively forming the Qi-Qin Accretionary Belt (QQAB) with a total length of ~2000 km (Song et al., 2017). The SQAB composed of two sequences: a Cambrian to Ordovician ophiolite sequence and an Ordovician arc-volcanic sequence (Zhang et al., 2017; Song et al., 2017). The ophiolites crop out to the north of the arc sequence and consist of massive and pillow picrite, ocean-island tholeiitic and alkaline basalt with minor ultramafic rocks, gabbro and pelagic chert (Fu et al., 2014; Zhang et al., 2017). The arc-volcanic sequence is mainly composed of pillow metabasalt, volcanoclastic rocks and andesitic porphyry, which are imbricated with chert and minor carbonate (Xiao et al., 2009). Silurian flysch occurs as fault-bounded slices within the accretionary complex. These rocks are unconformably overlain by Devonian molasse and Carboniferous to Triassic sedimentary cover.

## ROCK ASSEMBLAGES

The SQAB arc-volcanic complex occurs in the south part of the accretionary terranes in the NW-SE orientation with an area of ~ 200×20 km<sup>2</sup> (Fig. 1c). It is bounded by thrust faults with the ophiolite sequence, and is unconformably covered by Cretaceous strata. Samples were collected along the extension of the arc-volcanic complex within Lajishan-Yongjing terrane (see Fig. 1c for sampling localities). A cross-section in Zhaba town (Fig. 1d) shows the relations of pillowed and massive basalt-andesite with layered dacitic lava and volcanoclastic rock. The upper-crust

exposures are OIB-type pillow lavas (>500 Ma) as described by Zhang et al. (2017). The lower part of the arc suite (~460-440 Ma) is composed of thick sequence of amphibole-rich diabase, intruded by diorite, and overlain by intermediate-basic volcanics. The intermediate-basic volcanics are dark-colored lavas, massive or pillow structures, which are generally porphyritic and characterized by an essentially glassy groundmass with varying amounts of microlites (Fig. 2a and b). The upper part of the exposures of the arc suite are composed of thick sequences of light-colored lavas ranging from andesite to dacite overlain by tuff and volcaniclastic debris-flow deposits (Fig. 2c and d). Five types of lithologies can be recognized in the field based on their colour and structure: (1) dark-green colored, pyroxene-phenocryst-rich basalt-andesite (ankaramite), (2) dark-green colored, phenocryst-poor basaltic andesite with pillow and massive structures (boninite and high-Mg basaltic andesite) (Fig. 2a); (3) reddish andesite with plagioclase phenocrysts (high-Al andesite) (Fig. 2b); (4) pale-white/grey colored dacite with Pl and/or Qtz phenocrysts (mostly sanukite) (Fig. 2c); and (5) volcanic breccia (Fig. 2d).

**ANALYTICAL METHODS**

**Bulk rock major and trace element analyses**

Bulk-rock major and trace element analyses were carried out at China University of Geosciences, Beijing (CUGB) and the detailed analytical procedures have been given by Song et al. (2010). Bulk-rock major element oxides were determined using inductively coupled plasma-atomic emission spectroscopy (ICP-OES). The analytical

uncertainties are generally less than 1% for most elements with the exception of  $\text{TiO}_2$  (~1.5%) and  $\text{P}_2\text{O}_5$  (~2.0%) based on rock standards GSR-1, and GSR-3 (national geological standard reference material of China), AGV-2, W-2 (U.S. Geological Survey: USGS). Loss on ignition (LOI) was determined by placing 1 g of samples in the furnace at 1000°C for 3 hours before being cooled in a desiccator and reweighed. The trace element analyses were accomplished on an Agilent-7500a inductively coupled plasma mass spectrometer (ICP-MS). About 50 mg powder of each sample was dissolved in equal mixture of distilled HF and  $\text{HNO}_3$  in Teflon digesting vessels and heated at 195 °C for 48 hours using high-pressure bombs for digestion. The sample was then evaporated to incipient dryness, refluxed with 1 ml of 6N  $\text{HNO}_3$  and heated again. The sample was again dissolved in 2 ml of 3N  $\text{HNO}_3$  and heated at 165 °C for further 24 h to guarantee complete dissolution. Finally, they were diluted with Milli-Q water (18M $\Omega$ ) to a dilution factor of 2000 in 2%  $\text{HNO}_3$  solution for analysis. Rock standards AGV-2, W-2, and BHVO-2 (USGS) were used to monitor the analytical accuracy and precision. The analytical accuracy, as indicated by relative difference between measured and recommended values, is better than 5% for most elements, and 10~15% for Cu, Sc, Nb, Ta, Er, Tm, Gd Th, and U.

## Mineral chemistry

In-situ mineral analyses for major element oxides, including clinopyroxene (Cpx) and spinel, were done on a JEOL JXA-8100 Electron Probe Micro Analyzer (EPMA) at Peking University. Analytical conditions were optimized for standard silicates and

oxides at 15 kV accelerating voltage with a 20 nA focused beam current for all the elements. In-situ mineral analyses for trace elements in Cpx were accomplished on an Agilent-7500a inductively coupled plasma mass spectrometer (ICP-MS) coupled with a New Wave UP-193 solid-state LA system in the Geological Lab Center, CUGB. Routine analyses were obtained by counting for 30s at peak and 10s on background. Repeated analysis of natural and synthetic mineral standards yielded precisions better than  $\pm 2\%$  for most elements.

**Bulk rock Sr-Nd isotope analyses**

Separation and purification of Sr-Nd were carried out using conventional two-column ion exchange procedures in the ultraclean laboratory of the MOE Key Laboratory at Peking University. About 300 mg of unknown sample and ~200 mg of standard sample (BCR-2) were dissolved in mixture of HF+HNO<sub>3</sub> in Teflon vessels and heated at 140°C for 7days in order to be completely dissolved. The pure Sr and Nd were separated from the remaining solution by passing through conventional cation columns (AG50W and P507) and the detailed ion exchange procedures include: (1) separation of Sr and light rare earth elements (LREE) group through a cation-exchange column (packed with 200 mesh AG50W resin); (2) purification of Nd through a second cation-exchange column (packed with 200 mesh P507 resin). The bulk-rock Sr-Nd isotope analyses were performed by multi-collector inductively coupled plasma mass spectrometer (MC-ICP-MS) at MOE Key Laboratory of Orogenic Belts and Crustal Evolution, Peking University. The <sup>87</sup>Rb/<sup>86</sup>Sr and

<sup>147</sup>Sm/<sup>144</sup>Nd ratios were calculated based on Rb, Sr, Sm, and Nd contents determined by ICP-MS (CUGB). Mass fractionation corrections for Sr and Nd isotopic compositions were normalized to <sup>86</sup>Sr/<sup>88</sup>Sr = 0.1194 and <sup>146</sup>Nd/<sup>144</sup>Nd = 0.7219, respectively. All <sup>87</sup>Sr/<sup>86</sup>Sr ratios have been adjusted against Sr standard NBS-987 Sr = 0.710250 and the reported <sup>143</sup>Nd/<sup>144</sup>Nd ratios were further adjusted relative to the JNdi-1 standard of 0.512115. Initial <sup>143</sup>Nd/<sup>144</sup>Nd ratios and corresponding  $\epsilon_{Nd}(t)$  values were calculated on the basis of present-day reference values for CHUR: (<sup>143</sup>Nd/<sup>144</sup>Nd)<sub>CHUR</sub> = 0.512638 and (<sup>147</sup>Sm/<sup>144</sup>Nd)<sub>CHUR</sub> = 0.1967 (Jacobsen & Wasserburg, 1984). Rock standard BCR-2 was used to evaluate the separation and purification process of Rb, Sr, Sm, and Nd. Repeated analyses for the Nd and Sr standard samples (JNdi and NBS987) yielded <sup>143</sup>Nd/<sup>144</sup>Nd = 0.512197 ± 11 (2σ, n=7) and <sup>87</sup>Sr/<sup>86</sup>Sr = 0.710229 ± 11 (2σ, n=7), respectively.

#### **Zircon U-Pb dating analysis**

Zircons were separated by using standard density and magnetic separation techniques. Zircon grains were embedded in an epoxy mount and then polished down to expose the inner structure for analysis. Cathodoluminescence (CL) images were acquired to observe the internal structures of zircon grains, using a CL spectrometer (Garton Mono CL<sup>3+</sup>) equipped on a Quanta 200F environmental scanning electron microscope at scanning conditions of 15 kV/120 nA in the School of Earth and Space Sciences, Peking University.

Measurements of U-Th-Pb isotopes for samples LJ15-01, LJ15-70 were conducted

254 using a Cameca IMS-1280 secondary ion mass spectrometry (SIMS) in the Institute of  
255 Geology and Geophysics, Chinese Academy of Sciences, Beijing. The U-Pb dating  
256 analyses were conducted after the O isotope analyses and obtained at the same  
257 domain. Before the U-Pb dating analyses, the mounted zircons were carefully  
258 re-ground and re-polished. The analytical procedures are similar to those reported by  
259 Li et al. (2010a and b). The O<sup>2-</sup> primary ion beam was accelerated at 13 kV, with an  
260 intensity of ca. 8 nA. The ion beam diameter is about 20×30 μm in size. Analysis of  
261 the standard zircon Plésovice (337Ma, Sláma et al., 2008) was interspersed with  
262 analysis of unknowns. Each measurement consisted of seven cycles. Pb/U calibration  
263 was performed relative to zircon standard Plésovice and U, Th concentrations were  
264 calibrated against zircon standard 91500 (Wiedenbeck et al., 1995). An in-house  
265 zircon standard Qinghu (159.5 ± 0.2 Ma, Li et al., 2013b) was alternately analyzed as  
266 an unknown together with other unknown zircons in order to monitor the external  
267 uncertainties of SIMS U-Pb zircon dating calibrated against the Plésovice standard.  
268 The measurements on the Qinghu zircon yield Concordia ages of 161.1 ± 1.3 Ma. The  
269 instrument description and analytical procedure is given by Li et al. (2013a).  
270 Corrections are sufficiently small to be insensitive to the choice of common Pb  
271 composition, and an average of present-day crustal composition (Stacey and Kramers,  
272 1975) was used for the common Pb assuming that the common Pb is largely surface  
273 contamination introduced during sample preparation. Data reduction was carried out  
274 using the Isoplot/Ex v. 3.0 program (Ludwig, 2003). Uncertainties on individual  
275 analyses in data tables are reported at 1σ level; concordia U-Pb ages are quoted with

276 95% confidence interval.

277 Measurements of U-Th-Pb isotopes in zircons for other samples were carried out on  
278 an Agilent-7500a quadrupole inductively coupled plasma mass spectrometry coupled  
279 with a New Wave SS UP193 laser sampler (LA-ICP-MS) at CUGB. Analytical details  
280 were comprehensively described by [Song et al., \(2010\)](#). Laser spot size of 36  $\mu\text{m}$ ,  
281 laser energy density of 8.5 J/cm<sup>2</sup> and a repetition rate of 10 Hz were applied for  
282 analysis. The procedure of laser sampling is 5s pre-ablation, 20s sample-chamber  
283 flushing and 40s sampling ablation. The ablated material is carried into the ICP-MS  
284 by the high-purity Helium gas stream with flux of 0.8 L/min. The whole laser path  
285 was fluxed with N<sub>2</sub> (15 L/min) and Ar (1.15 L/min) in order to increase energy  
286 stability. National Institute of Standards and Technology 610 glass and zircon  
287 standard 91500 ([Wiedenbeck et al., 1995](#)) were used as external standards, Si as  
288 internal standard, and zircon standard Qinghu zircon as the secondary standard. The  
289 software GLITTER (ver. 4.4, Macquarie University) was used to process the isotopic  
290 ratios and element concentrations of zircons. The common lead correction was done  
291 following [Andersen \(2002\)](#). Age calculations and plots of concordia diagrams were  
292 made using Isoplot/Ex v. 3.0 program ([Ludwig, 2003](#)).

### 293 **Zircon Hf-O isotope analysis**

294 In-situ zircon Hf isotope analyses were performed on the zircons previously used  
295 for LA-ICP-MS U-Pb dating using a Geolas Pro laser-ablation system coupled to a  
296 Neptune multiple-collector ICP-MS at the Key Laboratory for the study of focused



Magmatism and Giant ore Deposits, MLR, in Xi'an Center of Geological Survey, China Geological Survey. Details of the instrumental conditions and data acquisition procedures are similar to those described by [Iizuka & Hirata \(2005\)](#), [Wu et al. \(2006\)](#) and [Hou et al. \(2007\)](#). A stationary laser ablation spot with a beam diameter of 44  $\mu\text{m}$  was used for the analyses and the ablation time was 26s. The ablated aerosol was carried by helium and then combined with argon in a mixing chamber before being introduced to the ICP-MS plasma. Before the analysis, standard zircons (TEMORA, GJ1 and FM02) were analyzed and the isotopes  $^{172}\text{Yb}$ ,  $^{173}\text{Yb}$  and  $^{175}\text{Lu}$  were simultaneously monitored during each analysis to correct the interferences of  $^{176}\text{Lu}$  and  $^{176}\text{Yb}$  on  $^{176}\text{Hf}$ . Corrections for  $^{176}\text{Lu}$  and  $^{176}\text{Yb}$  isobaric interferences on readings for  $^{176}\text{Hf}$  used the values of  $^{176}\text{Lu}/^{175}\text{Lu} = 0.02658$  and  $^{176}\text{Yb}/^{173}\text{Yb} = 0.796218$ , respectively ([Chu et al., 2002](#)). Instrumental mass bias was corrected by normalizing Hf isotope ratios to  $^{179}\text{Hf}/^{177}\text{Hf} = 0.7325$  and Yb isotope ratios to  $^{172}\text{Yb}/^{173}\text{Yb} = 1.35274$  ([Chu et al., 2002](#)), using the exponential mass fractionation law. Zircon GJ-1 was used as the reference standard and yielded a weighted mean  $^{176}\text{Hf}/^{177}\text{Hf}$  ratio of  $0.282030 \pm 40$  ( $2\sigma$ ,  $n=30$ ) during this study, identical to their reference values within analytical error ([Morel et al., 2008](#)). A decay constant for  $^{176}\text{Lu}$  of  $1.865 \times 10^{-11} \text{ year}^{-1}$  ([Scherer et al., 2001](#)) and the present-day chondritic ratios of  $^{176}\text{Hf}/^{177}\text{Hf} = 0.282772$  and  $^{176}\text{Lu}/^{177}\text{Hf} = 0.0332$  ([Blichert-Toft & Albarède, 1997](#)) were used for calculating  $\varepsilon_{\text{Hf}}(t)$  values. Depleted mantle model ages ( $T_{\text{DM1}}$ ) were calculated using the measured  $^{176}\text{Lu}/^{177}\text{Hf}$  and  $^{176}\text{Hf}/^{177}\text{Hf}$  ratios with reference to depleted mantle with present-day values of  $^{176}\text{Hf}/^{177}\text{Hf} = 0.28325$  and  $^{176}\text{Lu}/^{177}\text{Hf} = 0.0384$  ([Griffin et al., 2000](#)). The

1  
2  
3  
4 319 initial  $^{176}\text{Hf}/^{177}\text{Hf}$  ratios of the zircon are used to calculate the average continental  
5  
6 320 crust model ages ( $T_{\text{DM}2}$ ) assuming a mean crustal  $^{176}\text{Lu}/^{177}\text{Hf}$  value of 0.015 (Griffin  
7  
8 321 et al., 2004). In-situ zircon O isotope analyses were conducted by Cameca IMS-1280  
9  
10 322 SIMS system at the State Key Laboratory of Lithospheric Evolution in the Institute of  
11  
12 323 Geology and Geophysics, Chinese Academy of Sciences, Beijing. The zircon O  
13  
14 324 isotope analysis was conducted prior to the SIMS U-Pb dating to avoid the influence  
15  
16 325 of oxygen implanted in the zircon surface from the  $\text{O}^{2-}$  beam used for the U-Pb  
17  
18 326 determination. Details of the instrumentation and operating conditions have been  
19  
20 327 given by Li et al. (2010a and b). The  $\text{Cs}^+$  primary ion beam was accelerated at 10 kV,  
21  
22 328 with an intensity of ca. 2 nA (Gaussian mode with a primary beam aperture of 200  $\mu\text{m}$   
23  
24 329 to reduce aberrations) and rastered over a 10  $\mu\text{m}$  area. The analysis spot is about  
25  
26 330 20  $\mu\text{m}$  in diameter. Oxygen isotopes were measured using multi-collection mode on  
27  
28 331 two off-axis Faraday Cups (FC). The NMR (Nuclear Magnetic Resonance) probe was  
29  
30 332 used for magnetic field control with stability better than 2.5 ppm over 16 h on mass  
31  
32 333 17. One analysis takes  $\sim 4$  min including pre-sputtering ( $\sim 120\text{s}$ ), automatic beam  
33  
34 334 centering ( $\sim 60\text{s}$ ) and integration of oxygen isotopes ( $4\text{s} \times 10$  cycles, total 40s). With  
35  
36 335 low noise on the two FC amplifiers, the internal precision of single analysis is  
37  
38 336 generally better than  $\pm 0.2\text{‰}$  for  $\delta^{18}\text{O}$  values. Measured  $^{18}\text{O}/^{16}\text{O}$  is normalized using  
39  
40 337 the Vienna Standard Mean Ocean Water (VSMOW) compositions and reported in  
41  
42 338 standard per mil notation with  $2\sigma$  errors, and then corrected for instrumental mass  
43  
44 339 fractionation factor (IMF) following the methods of Li et al. (2010a). The IMF is  
45  
46 340 corrected using in-house zircon standard Penglai with recommended  $^{18}\text{O}/^{16}\text{O}$  ratio of  
47  
48  
49  
50  
51  
52  
53  
54  
55  
56  
57  
58  
59  
60

0.0020052 and ( $\delta^{18}\text{O}$ )<sub>VSMOW</sub> value of  $5.31 \pm 0.10\text{‰}$  (Li et al., 2010b). Twenty-nine measurements of Penglai yielded a weighted mean  $\delta^{18}\text{O} = 5.27 \pm 0.12 \text{‰}$  ( $2\sigma$  SD,  $n=29$ ), which agrees well with the recommended ( $\delta^{18}\text{O}$ )<sub>VSMOW</sub> value within errors (Li et al., 2010b). During the course of this study, the secondary in-house zircon standard Qinghu was also measured as an unknown to monitor the external precision. Ten measurements of Qinghu yielded a weighted mean  $\delta^{18}\text{O} = 5.52 \pm 0.15 \text{‰}$  ( $2\sigma$  SD,  $n=10$ ), consistent with the recommended ( $\delta^{18}\text{O}$ )<sub>VSMOW</sub> value of  $5.4 \pm 0.2$  within errors (Li et al., 2013b).

**RESULTS**

**Rock classification**

Thin-sections of samples were carefully examined under microscope and most of them experienced, to different degrees, low grade metamorphism (e.g. zeolite or prehnite-pumpellyite facies) (Fig. 2e-i). Bulk rock major and trace element analyses are listed in Table 1 and plotted in Figs. 3 and 4. All major element contents were normalized to 100% on a volatile-free basis before plotting. In particular, a small number of samples with high LOI values (Table 1) show different degrees of alteration and thus have been removed before plotting. Most of the samples fall in the sub-alkaline field with a few samples lying in the transition field between alkaline and sub-alkaline series on the TAS diagram (Fig. 3a) and all the samples plot in the sub-alkaline field on the  $\text{SiO}_2\text{-Zr/TiO}_2$  diagram (Fig. 3b); this can be attributed to a slight influence on the mobile elements (e.g. Na and K) by the low grade

metamorphism or alteration. In addition, they mainly plot in the island arc field on the Hf-Th-Ta diagram (Fig. 3d) and show a calc-alkaline trend on the AFM diagram (Fig. 3c). Accordingly, the lavas can be identified geochemically as (1) boninite, (2) ankaramite, (3) high-Mg basaltic andesite, (4) high-Al andesite and (5) sanukite.

**Boninite.** The boninites are extensively altered with the development of the typical mineral assemblage of low-grade greenschist facies conditions (Fig. 2e). Phenocryst pseudomorphs of pyroxene and/or olivine have been altered to chlorite, serpentinite or tremolite in a groundmass of devitrified glass composed of altered minerals (e.g., chlorite, sericite) and chrome spinel (Fig. 2e). The boninite samples, with moderate SiO<sub>2</sub> (49.7-58.9 wt. %), are characterized by variably high contents of MgO (5.0-19.3 wt. %), Cr (51-2486 ppm) and Ni (47-453 ppm), but low TiO<sub>2</sub> (mostly < 0.5 wt. %), and Zr (< 55 ppm) contents. In chondrite-normalized REE patterns (Fig. 4a), all boninite samples display variably low REE abundances (4.1-17.8×C1), and have slightly LREE depleted to enriched patterns with (La/Sm)<sub>N</sub> ratios of 0.49-1.49, and no to minor negative Eu anomaly (Eu/Eu\* = 0.43-1.07, with an average of 0.87). In the multi-element spider diagrams (Fig. 4b), they are depleted in HFSEs (Nb, Ta, Zr, Hf, P and Ti) and enriched in water-soluble elements (Rb, Ba, U, Pb and Sr).

**Ankaramite.** The ankaramites are porphyritic with abundant, euhedral Ca-rich Cpx phenocrysts in a usually intersertal to intergranular groundmass filled with plagioclase laths, chloritized glass/or diopside microlites, Fe-Ti oxides as well as chrome spinel (Fig. 2f). Chromian spinel grains are visible in the matrix and as inclusions in Cpx grains. The ankaramite samples are characterized by lower SiO<sub>2</sub>

content (48.0-49.2 wt. %), but higher contents of MgO (15.0-15.6 wt. %), Cr and Ni, relative to the boninites. In chondrite-normalized REE patterns (Fig. 4c), all samples display low REE abundances, slight LREE enrichment with (La/Sm)<sub>N</sub> ratios of 2.70-3.09, and no Eu anomaly. In multi-element spider diagrams (Fig. 4d), they are depleted in Nb, Ta, P and Ti and enriched in water-soluble elements (Rb, Ba, U, Pb and Sr).

**High-Mg basaltic andesite.** The high-Mg basaltic andesites are also porphyritic with euhedral Ca-rich Cpx and amphibole phenocrysts in a usually intersertal to intergranular groundmass filled with plagioclase laths (Fig. 2g). They show variable SiO<sub>2</sub> (49.6-55.6 wt. %) and are characterized by low Al<sub>2</sub>O<sub>3</sub> (11.7-17.5 wt. %) content but high contents of MgO (6.7-10.0 wt. %), Fe<sub>2</sub>O<sub>3T</sub> (5.6-10.5 wt. %), CaO (7.7-12.5 wt. %), TiO<sub>2</sub> (0.60-1.21 wt. %), Cr (253-503 ppm) and Ni (72-198 ppm). The chondrite-normalized REE patterns show light rare earth element (LREE) enrichment with (La/Sm)<sub>N</sub> ratios of 2.24-4.26 and no Eu anomalies (Fig. 4c). In the multi-element spider diagrams (Fig. 4d), they are depleted in HFSEs (Nb, Ta, Zr, Hf, P and Ti) and enriched in LILEs (e.g. Rb, Ba, Pb, Sr and Th).

**High-Al andesite.** The high-Al andesites have porphyritic textures with abundant euhedral, lath-shaped plagioclase and minor embayed pyroxene and amphibole pseudomorphs in an intersertal groundmass filled with plagioclase laths and glass as well as opaque minerals (Fig. 2h). They are of basaltic andesite to dacite composition with moderate SiO<sub>2</sub> (48.7-60.5 wt. %) and a relatively large compositional range in terms of other major elements (Table 1; Figs 3). In addition, they are characterized by

high  $\text{Al}_2\text{O}_3$  (16.2-23.1 wt. %) content but low contents of MgO (1.1-5.5 wt. %), Cr (2.0-108.3 ppm) and Ni (1.4-38.4 ppm). The chondrite-normalized REE patterns show light rare earth element (LREE) enrichment with  $(\text{La}/\text{Sm})_{\text{N}}$  ratios of 1.69-5.34 and no to negative Eu anomalies ( $\text{Eu}/\text{Eu}^*=0.90-1.15$ ) (Fig. 4e). In the multi-element spider diagrams, they are depleted in HFSEs (Nb, Ta, Zr, Hf and Ti) and enriched in mobile elements (Rb, Ba, U, Th and Pb) (Fig. 4f). The covariation of negative Sr and Eu anomalies occurred in some samples, and may result from the crystallization of plagioclase.

**Sanukite.** Sanukites show a pale-white color and porphyritic texture in the field with sulfide mineralization. The phenocryst minerals are mainly plagioclase, quartz, plus minor pyroxene pseudomorphs (Fig. 2i). The plagioclase phenocrysts are lath-shaped, and the olivine or pyroxene phenocrysts are euhedral and have altered to chlorite. The matrix is mainly composed of fine-grained plagioclase and glass. Geochemically, they are characterized by andesite to dacite composition of  $\text{SiO}_2$  (54.5-60.7 wt. %), high  $\text{K}_2\text{O}$  (> 1.0 wt. %),  $\text{Mg}\# > 65$  and high Cr (384~521 ppm) and Ni (111~139 ppm). The evolved equivalent of dacite samples ( $\text{Mg}\# = 55\sim 64$ ) contain high  $\text{SiO}_2$  (61.6-65.8 wt. %) and low Cr (46~113 ppm) and Ni (10~26 ppm). The chondrite-normalized REE patterns show light rare earth element (LREE) enrichment with  $(\text{La}/\text{Sm})_{\text{N}}$  ratios of 4.6~6.2 and no to minor negative Eu anomalies ( $\text{Eu}/\text{Eu}^*=0.76-1.04$ ) (Fig. 4g). In the multi-element spider diagrams (Fig. 4h), they are variously depleted in Ba, Sr, HFSEs (Nb, Ta and Ti) and enriched in LILEs (e.g. Rb, Th, U and Pb). Therefore, these lavas have similar major and trace element

compositions to sanukite ( $\text{SiO}_2=55\sim60$  wt. %;  $\text{Mg\#}>0.6$ ;  $\text{K}_2\text{O}>1$  wt. %;  $\text{Cr}>200$  ppm;  $\text{Ni}>100$  ppm;  $\text{Ba}>500$  ppm;  $\text{Sr}>500$  ppm; Stern et al., 1989; Tatsumi, 2006).

**Mineral Chemistry**

Samples of primitive lavas from the Lajishan-Yongjing island-arc volcanic complex were chosen to characterize mineral compositions, including Cr-spinel and Cpx from two Cpx-phyric ankaramites (13QLS-68, 13QLS-72), two high-Mg basaltic andesite (13QLS-124, LJ15-42) and two boninites (LJ15-12, LJ15-15). The representative compositions for major element oxides and trace elements are given in Table 2 and Appendix Table 1-3.

**Chromian spinel.** Spinels from boninite are characterized by high Cr# [ $\text{Cr}/(\text{Cr}+\text{Al})=75.3\text{-}90.6$ ], low  $\text{Al}_2\text{O}_3$  and  $\text{TiO}_2$  contents with normal to evolved Mg# [ $\text{Mg}/(\text{Fe}^{2+} + \text{Mg})$ ] varying from cores of 35.63-52.90 to rims of 1.45-22.60 (Fig. 5). Spinels from ankaramite samples are characterized by relative lower Cr# [ $\text{Cr}/(\text{Cr}+\text{Al})=68.5\text{-}81.9$ ], higher  $\text{Al}_2\text{O}_3$ , and  $\text{TiO}_2$  contents than those from boninite, with normal to evolved Mg# varying from 1.74 to 43.66 (Fig. 5). Spinels from ankaramite can be subdivided in two groups: the chromian spinel grains from matrix and the chromian spinel inclusions in Cpx grains. Spinel grains in the matrix have higher Cr# (69.6-90.6), higher  $\text{TiO}_2$ , and lower Mg# and  $\text{Al}_2\text{O}_3$  than inclusions in Cpx, which may result from mineral-melt interaction (Cao et al., 2016).

**Clinopyroxene.** Cpx phenocrysts are mostly Ca-rich Cpx with a formula of  $\text{Wo}_{(38-47)}\text{En}_{(43-50)}\text{Fs}_{(5-16)}$  and Mg# varying from 76-94. Cpx from primitive samples

(13QLS-68, 13QLS-72, LJ15-42) have high Mg# (87-94), Cr# (12-25), and high contents of SiO<sub>2</sub> (51.74-53.27 wt. %) and CaO (21.94-22.36 wt. %), but low contents of TiO<sub>2</sub> (0.13-0.45 wt. %), Al<sub>2</sub>O<sub>3</sub> (1.75-3.45 wt. %), FeO (3.67-4.67 wt. %) and Na<sub>2</sub>O (0.20-0.29 wt. %). In contrast, two kinds of Cpx grains occur in the evolved sample (13QLS-124), including homogeneous low-Mg# grains and recrystallized Cpx grains exhibiting core-rim structure with high-Mg# core and low-Mg# rim. The cores of the recrystallized Cpx grains have higher Mg#, Cr#, SiO<sub>2</sub> and CaO, but low TiO<sub>2</sub>, Al<sub>2</sub>O<sub>3</sub> and FeO<sub>T</sub> than either rims of recrystallized Cpx or low Mg# Cpx grains, corresponding with the high Mg# Cpx grains in primitive samples (Fig. 6). The Mg# of Cpx shows positive correlation with SiO<sub>2</sub>, CaO and Cr#, and negative correlation with TiO<sub>2</sub>, Al<sub>2</sub>O<sub>3</sub> and Na<sub>2</sub>O contents (Fig. 6).

Trace elements of Cpx grains (Appendix Table 3) are characterized by depletions in light rare earth elements (LREEs) with (La/Sm)<sub>N</sub> = 0.34-0.61, gently fractionated heavy rare earth elements (HREEs) with (Dy/Yb)<sub>N</sub>=(1.12-2.21). Cpx rims from the sample 13QLS-124 (Mg#=69) have higher trace elements contents than the cores (Mg#=89-93), while the Cpx compositions from sample 13QLS-72 (Mg#=77) are relative homogeneous and coincide with (or are slightly higher than) the Cpx cores in sample 13QLS-124. On a primitive mantle-normalized diagram, the Cpx cores are characterized by negative anomalies in Nb, Zr, Hf and Ti, variable enrichments in Rb, Sr, Pb, Th and U, while the rims show strongly negative Sr anomalies (Fig. S1). To further estimate the parental magmas of the Cpx-phyric basaltic andesite, we used the Cpx/basalt partition coefficients to calculate the primary melt compositions as



described by Tang et al. (2012) and references therein. The back-calculated melt concentrations for the Cpx cores with the highest Mg# from sample 13QLS-124 are considered as the primary melt compositions (Appendix Table 3).

**Whole-rock Sr-Nd Isotopes**

We selected samples with the lowest LOI values to minimize the influence on the Sr-isotopes triggered by alteration or low grade metamorphism. Whole-rock Sr-Nd isotopic data for the Lajishan-Yongjing island arc volcanic complex are given in Table 3. Initial Sr isotopic ratios and  $\epsilon_{Nd}(t)$  values are calculated at  $t = 450$  Ma based on the zircon U-Pb dating. Seven boninite samples have variable initial  $^{87}\text{Sr}/^{86}\text{Sr}$  ratios of 0.7041-0.7056 and  $\epsilon_{Nd}(t)$  values of 1.80-8.39. Two ankaramite samples exhibit limited initial  $^{87}\text{Sr}/^{86}\text{Sr}$  ratios of 0.7050-0.7052 and  $\epsilon_{Nd}(t)$  values of 2.46-2.78. Four high-Mg basaltic andesite samples show a narrow range of initial  $^{87}\text{Sr}/^{86}\text{Sr}$  ratios of 0.7046 to 0.7053 and  $\epsilon_{Nd}(t)$  values of 0.95 to 2.78. Two high-Al andesite samples show limited initial  $^{87}\text{Sr}/^{86}\text{Sr}$  ratios of 0.7050 to 0.7053 and  $\epsilon_{Nd}(t)$  values of 1.69-2.7. They exhibit covariation between Sr and Nd isotopes. Six sanukite samples show a range of initial  $^{87}\text{Sr}/^{86}\text{Sr}$  ratios of 0.7061 to 0.7073 and  $\epsilon_{Nd}(t)$  values of -2.07 to -5.66. Two coeval meta-sedimentary samples, occurring as interlayers within volcanic rocks, show a narrow range of initial  $^{87}\text{Sr}/^{86}\text{Sr}$  ratios of 0.7098 and  $\epsilon_{Nd}(t)$  values of -6.73 to -7.40. It should be noted that the relatively high initial Sr isotopic values of some samples indicate that the Sr-isotopes may be influenced by the variable degree of alteration. However, the influence is insignificant, given that these samples form a

1  
2  
3  
4 492 tight cluster in the Sr-Nd diagram (see below). Instead, all the Sr-Nd isotopic data of  
5  
6 493 volcanic samples overlap the transition field, showing the possibility of mixing  
7  
8 494 between an enriched mantle source and oceanic sediments.  
9

#### 10 11 12 495 **Zircon U-Pb ages** 13

14  
15 496 Six volcanic samples from the Lajishan-Yongjing Terrane were selected for  
16  
17 497 LA-ICP-MS and SIMS zircon U-Pb dating, including a boninite (LJ15-01), a high-Mg  
18  
19 498 basaltic andesite (16LJ-27), a high-Al andesite (LJ15-70) and three sanukite samples  
20  
21 499 (12LJ-15, 16LJ-55 and 16LJ-69). The CL images of representative zircon grains are  
22  
23 500 illustrated in Fig. S2, and zircon U-Pb isotope data are presented in Fig. 7 and listed in  
24  
25 501 Appendix Table 4. All zircons are subhedral to euhedral, colorless and transparent,  
26  
27 502 and have grain sizes of 30-300µm with length to width ratios of 1:1 to 3:1. Zircons  
28  
29 503 from sanukite samples (16LJ-55 and 16LJ-69) show oscillatory or banded zoning,  
30  
31 504 whereas zircons from the other samples exhibit broad oscillatory zoning, weak or no  
32  
33 505 obvious zoning in the CL images (Fig. S1). As shown in Appendix Table 4, most  
34  
35 506 zircon U-Pb isotope data are concordant within analytical error.  
36  
37  
38  
39  
40  
41

42 507 Zircon U-Pb isotopic analyses from boninite sample LJ15-01 by SIMS show  
43  
44 508 highly variable Th (118-2693 ppm) and U contents (67-4050 ppm) with high Th/U  
45  
46 509 ratios (0.22-2.79). Nineteen analyses give a weighted  $^{206}\text{Pb}/^{238}\text{U}$  mean age of  $450 \pm 6$   
47  
48 510 Ma (MSWD=2.3, n=16), with three relict zircons aged 523-1701Ma (Fig. 7a).  
49

50  
51 511 Zircons from the high-Mg basaltic andesite sample (16LJ-27) have moderate Th  
52  
53 512 (45-258 ppm) and U (115-472 ppm) contents and high Th/U ratios (0.65-1.35). Thirty  
54  
55  
56  
57  
58  
59  
60

analyses yield a concordia age of  $456 \pm 1$  Ma (MSWD=0.36, n=30) (Fig. 7b).

Zircons from the high-Al andesite sample (LJ15-70) have variable Th (117-1641 ppm) and U contents (222-831 ppm) with Th/U ratios of 0.45-2.66. Seventeen analyses by SIMS give a concordia age of  $452 \pm 1$  Ma (MSWD=0.95, n=17), and one relict zircon grain yields a  $^{206}\text{Pb}/^{238}\text{U}$  age of  $774 \pm 11$  Ma (Fig. 7c).

Zircons from the three sanukite samples (12LJ-15, 16LJ-55 and 16LJ-69) were analyzed by LA-ICP-MS method. They have consistent contents of U (183-570 ppm) and Th (108-394 ppm) with high Th/U ratios of 0.44-1.12. Twenty five analyses on zircon grains from 12LJ-15 yield a concordia age of  $440 \pm 1$  Ma (MSWD=0.61) (Fig. 7d). Twenty six analyses of 29 zircon grains from 16LJ-55 form a concordia age of  $448 \pm 1$  Ma (MSWD=0.54), apart from three strongly discordant ages, which may due to lead loss (Fig. 7e). Twenty two analyses on 25 zircon grains from 16LJ-69 yield a concordia age of  $455 \pm 1$  Ma (MSWD=0.52), with three relict zircon ages (Fig. 7f).

In summary, the U-Pb dating on magmatic zircon domains for the Lajishan-Yongjing arc volcanic complex yields consistent ages of 456 to 440 Ma, implying that the Lajishan-Yongjing island arc was formed in a relatively short period in Late Ordovician, much younger than ages of the adjacent ophiolite complex (~525 Ma, Zhang et al., 2017). Relict zircons are rare, suggesting insignificant assimilation of continental crust.

**Zircon Hf-O Isotopes**

Zircon Hf isotopic data for the Lajishan-Yongjing island arc complex are given

in [Appendix Table 5](#). Zircons of the high-Mg basaltic andesite (sample 16LJ-27) have a narrow range of initial  $^{176}\text{Hf}/^{177}\text{Hf}$  ratios (0.282819-0.282874) and the calculated  $\varepsilon_{\text{Hf}}$  ( $t=456\text{ Ma}$ ) values range from 11.69 to 15.38 with a weighted mean of  $13.72 \pm 0.57$  (MSWD=1.4,  $n = 16$ ). Zircons of the two sanukite samples (16LJ-55, 16LJ-69) have uniform initial  $^{176}\text{Hf}/^{177}\text{Hf}$  ratios (0.282300-0.282569) and the calculated  $\varepsilon_{\text{Hf}}(t)$  values range from -3.22 to 0.44 with a weighted mean of  $-0.27 \pm 0.43$  (MSWD=1.4,  $n = 16$ ) and from -2.11 to 1.62 with a weighted mean of  $-0.60 \pm 0.43$  (MSWD=2.2,  $n = 16$ ), respectively. It is notable that the Hf isotopic compositions of the island arc complex are decoupled from the Nd isotopic compositions, showing various positive  $\Delta \varepsilon_{\text{Hf}}(t)$  values of 10.85 for sample 16LJ-27, 4.20 for sample 16LJ-55, and 4.30 for sample 16LJ-69, respectively [ $\Delta \varepsilon_{\text{Hf}}(t) = \varepsilon_{\text{Hf}}(t) - 1.55\varepsilon_{\text{Nd}}(t) - 1.21$ ; [Vervoort et al., 2011](#)].

Zircon O isotopic data for the Lajishan-Yongjing island arc complex are given in [Table 4](#). The  $\delta^{18}\text{O}$  values for zircons of boninite (LJ15-01) mostly range from 6.57 to 7.61‰ with a weighted mean of  $7.17 \pm 0.13\text{‰}$  (MSWD=9.5,  $n = 17$ ). Zircons of high-Al andesite (LJ15-70) mostly have uniform  $\delta^{18}\text{O}$  values of 5.4-6.24 ‰ with a weighted mean of  $5.90 \pm 0.09\text{‰}$  (MSWD=5.6,  $n = 18$ ). The estimated whole-rock  $\delta^{18}\text{O}$  values roughly range from 7.44‰ to 8.49‰ (the mean of  $8.05 \pm 0.13\text{‰}$ ) for LJ15-01, and from 6.23 ‰ to 7.06‰ (the mean of  $6.73 \pm 0.09\text{‰}$ ) for LJ15-70 [ $\delta^{18}\text{O}_{\text{WR}} = \delta^{18}\text{O}_{\text{Zir}} + 0.0612 (\text{wt. \% SiO}_2) - 2.5$ ; [Valley et al., 2005](#)].

553 **DISCUSSION**

554 **Petrogenesis of the arc volcanic complex**

555 **Crustal assimilation/source mixing**

556       The compositions of primitive arc magmas are determined by the composition of  
557 the mantle source, the slab-derived components (including fluids and melts) and the  
558 P-T conditions of partial melting, and can be influenced by a number of factors, such  
559 as shallow-level crustal assimilation and fractional crystallization (AFC). Generally,  
560 source mixing and crustal assimilation are the two fundamental mechanisms for  
561 incorporation of crustal components into mantle-derived magmas, and thus are  
562 capable of producing variations in elemental and isotopic compositions of arc  
563 magmas (Zheng & Hermann, 2014; Bezard et al., 2015). In contrast, fractional  
564 crystallization can also occur during arc magma ascent that produces rock types with  
565 variations in the major and trace element compositions, but do not affect the isotopic  
566 compositions.

567       As shown in Figs. 8 and 9, boninite samples have distinct characteristics (e.g.  
568 low La/Sm and TiO<sub>2</sub>) and evolutionary trend from the other rock types, suggesting  
569 they derived from different sources of the mantle wedge. The other four types of rocks  
570 show positive correlations between La/Sm ratios versus La and SiO<sub>2</sub> content (Fig. 8a  
571 and b), indicating that the partial melting of metasomatized mantle or crustal  
572 contamination during ascent altogether readily explain the petrogenesis of the  
573 volcanic rocks. The sanukite has lowest ε<sub>Nd</sub> (t) and highest (<sup>87</sup>Sr/<sup>86</sup>Sr)<sub>i</sub>, and is likely to

have undergone a high degree of source metasomatism or crustal assimilation relative to other samples (Fig. 8c and d). In contrast, the boninite lavas exhibit high  $\epsilon_{\text{Nd}}(t)$ , low La/Sm ratios relative to other rock-types, suggesting that they are derived from more depleted mantle source with the least source metasomatism or crustal contamination. The ankaramite, high-Mg basaltic andesite and high-Al andesite exhibit similar La/Sm ratios,  $\epsilon_{\text{Nd}}(t)$  and  $(^{87}\text{Sr}/^{86}\text{Sr})_i$ , indicating that the degree of mantle metasomatism may be comparable. Based on the variations of  $\epsilon_{\text{Nd}}(t)$ ,  $(^{87}\text{Sr}/^{86}\text{Sr})_i$ , La/Sm ratios (Fig. 8a and b) and zircon Hf-O isotopes, all the rocks can be categorized into three independent magmatic series, including (1) boninite, (2) ankaramite-high-Mg basaltic andesite-high-Al andesite and (3) sanukite. Besides, the lithological assemblage of this region suggests an intra-oceanic arc setting, and thus crustal assimilation is likely to be insignificant during their ascent *en route* to the surface. In addition, a high degree of crustal contamination can be precluded by (1) the small range of Hf-O isotope and only few xenocrystal zircons in the grain population from the studied rocks (Fig. 7); and (2) the lack of enclaves in the outcrops. Therefore, the source metasomatism between subducted sediments and mantle wedge is likely to be the dominant mechanism responsible for the chemical variation among different rock groups.

## **Petrogenesis of boninite**

The boninite lavas, with low  $\text{TiO}_2$ , low  $\text{Al}_2\text{O}_3$ , high contents of MgO and  $(\text{Fe}_2\text{O}_3)_T$ , do not show covariations between major-trace elements and  $\text{SiO}_2$  with other

1  
2  
3  
4 595 lavas, suggesting that the boninites are unlikely to be the evolved products of the  
5  
6 596 parent magma of other lavas. Correlations between  $\text{Si}_2\text{O-MgO}$ ,  $\text{Si}_2\text{O-CaO}$  and Cr-V  
7  
8 597 suggest that the parental boninite magmas might have undergone pyroxene  
9  
10  
11 598 ( $\pm\text{Ol}$ )-dominated fractionation (Fig. 9).

12  
13 599 Boninites may be produced by hydrous re-melting of refractory lherzolite which  
14  
15  
16 600 is fluxed by slab-derived hydrous fluids/melts at high temperature and low pressure  
17  
18 601 (spinel domain) (Green et al., 2004). In the Th/Yb-Nb/Yb proxy (Pearce, 2008) for  
19  
20 602 recycled crustal components and selective Th and Nd addition, samples mainly plot  
21  
22 603 above the MORB-OIB array (Fig. 10a). As shown in Fig. 10b-c, the boninite was  
23  
24 604 replenished by a fluid-like slab-derived component enriched in mobile elements (e.g.  
25  
26 605 U and Ba), and relatively lacking in less fluid-soluble elements (e.g. Th and LREE).  
27  
28  
29 606 Although a role of slab-derived fluid in the generation of the boninite is evident from  
30  
31 607 Fig. 10b-c, the slight LREE and Th-Nd (Fig. 10a) enrichment cannot be explained by  
32  
33 608 fluid-like subduction components alone, and also requires the presence of melt-like  
34  
35 609 subduction components. Zircon  $\delta^{18}\text{O}$  values of 6.57‰-7.61‰ from boninite (LJ15-01)  
36  
37 610 are higher than that of primary mantle ( $\delta^{18}\text{O} = 5.3 \pm 0.3\text{‰}$ , Valley, 2003) (Fig. 11a).  
38  
39 611 Similarly, the calculated whole-rock  $\delta^{18}\text{O}$  range from 6.23‰ to 8.49‰, higher than  
40  
41 612 the  $\delta^{18}\text{O}$  values of depleted mantle (5.7‰) and uncontaminated oceanic plume source  
42  
43 613 (~6‰) (Condie, 2001 and references therein). The sediment-derived fluids with  
44  
45 614 elevated  $\delta^{18}\text{O}$  values can be triggered by a contamination of the pelagic sediments  
46  
47 615 ( $\delta^{18}\text{O}$  values of ca. 9~20‰) (Bindeman et al., 2005), and thus provide an appropriate  
48  
49 616 candidate. Here, we employed a simple two-end-member (peridotite plus oceanic  
50  
51  
52  
53  
54  
55  
56  
57  
58  
59  
60

sediments) mixing model of Sr-Nd isotopes for boninite samples, restricting the amount of sediment-derived fluids in the mantle source to less than 2% (Fig. 11b). Therefore, we argue that the involvement of silica-rich fluids derived from the recycled pelagic sediments plays a crucial role in the formation of the boninite lavas.

Lines of evidence for the nature of depleted harzburgitic residues of boninite includes the low contents of  $\text{Al}_2\text{O}_3$  and high Cr# in Cr-spinel and the very low whole rock HREE abundances. The average value of our boninite samples is consistent with average boninite compositions worldwide (Fig. 12a). We use the depleted DMM from Workman & Hart. (2005) as a model mantle source for the boninite. About 10-15% re-melting of depleted DMM produces a good fit to the boninite glass sample except for a large discrepancy in Rb, Ba, Th, U and Sr due to input from slab-derived components (Fig. 12a). Experimental studies indicate that progressive melting of fertile spinel lherzolite rapidly eliminates Cpx and gradually reduces the proportion of Opx at 10-20 kbar (Kelemen et al., 1995). Primary Cpx is normally exhausted after 20-30% partial melting of lherzolite (e.g., Niu, 1997, 2004). Thus, we argue for the mantle source of boninite as refractory, spinel-bearing, Cpx-poor lherzolite or harzburgite.

#### **Formation of ankaramite-high-Mg basaltic andesite-high-Al andesite**

The rock series of ankaramite, high-Mg basaltic andesite and high-Al andesite exhibits large  $\text{SiO}_2$  variation with relatively limited ranges of Sr-Nd isotope compositions (Fig. 8c and d). Also, they show a general linear trend between



major-trace elements and  $\text{SiO}_2$  (Fig. 9), suggesting that they may share a common magmatic lineage. The variation of Cpx compositions between ankaramite and high-Mg basaltic andesite is consistent with magma evolution. With the increase of  $\text{SiO}_2$ , the evolved samples show increases of  $\text{TiO}_2$ ,  $\text{Al}_2\text{O}_3$  and decreases of MgO (Mg#),  $(\text{Fe}_2\text{O}_3)_\text{T}$ , CaO, Cr and Ni. Combined with the correlations between V and Cr, the parental magmas might have undergone Cpx-dominated fractionation from ankaramite to high-Mg basaltic andesite. High-Al basaltic lavas are volumetrically important lavas in many intra-oceanic island arcs and often considered as derivative lavas (with plagioclase accumulation) of more primitive magmas containing 10-15% MgO, derived by partial melting of peridotite in the mantle wedge above the subducted slab (Crawford et al., 1987). Importantly, the negative correlation between  $\text{SiO}_2$  and MgO,  $(\text{Fe}_2\text{O}_3)_\text{T}$ , CaO,  $\text{Al}_2\text{O}_3$  contents and Sr/Y ratio, as well as the presence of both negative and positive Eu anomalies, indicate that plagioclase does become an important phase in the fractionating assemblage (Fig. 9). The decreases of MgO, Ni,  $(\text{Fe}_2\text{O}_3)_\text{T}$ , CaO from ankaramite, and high-Mg basaltic andesite to high-Al andesite suggest a process from pyroxene-dominated fractionation to plagioclase accumulation (Fig. 9). Crystallization of V-rich, Fe-Ti oxides within the studied rocks is reflected by a trend of decreasing V/Ti and V versus  $\text{SiO}_2$  (e.g. Nielsen et al., 1994), and positive correlation between  $(\text{Fe}_2\text{O}_3)_\text{T}$  and  $\text{TiO}_2$  (not shown).

The ankaramite-high-Mg basaltic andesite-high-Al andesite, as mentioned above, are likely to be of arc basaltic magmatic lineage with various degrees of Cpx fractional crystallization and Pl accumulation; the ankaramite lavas thus might be the

nearest to the parental magma. Island arc ankaramites (nepheline-normative, CaO-rich and silica-poor) have been identified from many volcanic arcs worldwide (e.g. Schiano et al., 2000; Green et al., 2004). The ankaramite samples, together with the high-Mg basaltic andesite, display enrichment of less fluid-soluble elements in Fig. 10a-c (e.g. Th and LREE), reflecting source input from subducted sediment-derived melts rather than fluids. Since Hf is also generally regarded as immobile in slab-derived fluids, a selective enrichment of Nd relative to Hf could be expected, thereby leading to a decoupling of Hf-Nd compositions toward less radiogenic  $\epsilon_{\text{Nd}}$  (Pearce et al., 1999) and positive  $\Delta\epsilon_{\text{Hf}}(t)$  values (Vervoort et al., 2011). The positive  $\Delta\epsilon_{\text{Hf}}(t)$  value of high-Mg basaltic andesite (10.85) thus can be imparted through source contamination of zircon-barren pelagic sediments (Chauvel et al., 2008; Choi et al., 2013) or selective melting of a mantle source with high Lu/Hf minerals (e.g. Bizimis et al. 2003; Choi & Mukasa, 2012), the latter of which cannot lead to the conspicuous elevation of O isotopic compositions (Wang et al., 2014). Given that the zircons from high-Al andesite sample have elevated  $\delta^{18}\text{O}$  values (Fig. 11a) relative to primary mantle ( $\delta^{18}\text{O} = 5.3 \pm 0.3\%$ , Valley, 2003), we argue that the positive  $\Delta\epsilon_{\text{Hf}}(t)$  value of high-Mg basaltic andesite (10.85) may be due to the contamination of zircon-barren pelagic sediments. Figure 11 illustrates the results of Sr-Nd-Hf mixing calculations in the case of slab dehydration and slab melting, respectively (Hanyu et al., 2006). The Sr-Nd data for ankaramite, high-Mg basaltic andesite and high-Al samples are well accounted for by the addition of ~2-4% of sediment-derived melts/fluids into the mantle wedge, consistent with the results of the Hf-Nd mixing

calculation (1-3%) for high-Mg basaltic andesite (Fig. 11b and c).

The primitive features of ankaramites, including high Mg#, Cr, Ni contents and Cr-rich spinel, are shared with other primitive arc magmas like boninites (e.g.  $F_o$  (Ol)>90; Cr# (Sp)>70: Crawford et al., 1989). Previous experimental work has shown that the primitive island-arc ankaramitic lavas are segregated from residual harzburgite at 1.5GPa, ~1320-1350 °C, fluxed by dolomitic carbonatite melts (C-H-O melts) (Green et al., 2004); Only high-pressure melts (above 1.5-1.8GPa) from peridotite are silica-undersaturated (e.g. Till et al., 2012). However, others have argued against this scenario on account of the high pressure experimental melts with insufficiently high CaO/Al<sub>2</sub>O<sub>3</sub> ratios and nepheline-normative contents, as well as the presence of residual garnet in the source, which contradicts the observation of ankaramitic melt inclusions with high CaO/Al<sub>2</sub>O<sub>3</sub> ratios and flat REE spectra (Elburg et al., 2007; Sorbadere et al., 2012). Therefore, another mechanism is required for the genesis of the ankaramitic melt inclusions that involves partial melting of amphibole-bearing, Cpx-rich cumulative pyroxenite lithologies at lower crustal or shallow upper mantle pressures (e.g. Schiano et al., 2000; Médard et al., 2006; Sorbadere et al., 2012). The high temperatures, however, needed to form nepheline-normative arc melt inclusions (up to 1300 °C; Schiano et al., 2000; Sorbadere et al., 2012) are difficult to reconcile with arc crust melting, which argues against the melting of lower-crustal cumulates as directly responsible for the common pyroxenitic signature of primitive arc magmas. Thus, both the peridotite melts and clinopyroxenite melts in the mantle wedge are indispensable. The recent experimental

1  
2  
3  
4 705 results also argue for the involvement of a heterogeneous hydrous mantle source  
5  
6 706 composed of lherzolite mixed with amphibole-bearing clinopyroxenites as a more  
7  
8 707 realistic model for the formation of arc ankaramitic melt inclusions (Sorbadere et al.,  
9  
10 708 2013).

11  
12  
13 709 Oscillatory zoning and variation of Mg# in Cpx grains and compositional  
14  
15 710 changes of the Cr-spinels in Cpx phenocrysts and in the matrix indicate several stages  
16  
17 711 of disequilibrium melt evolution. Thus, it is reasonable to use the high Mg# Cpx cores  
18  
19 712 to back-calculate the parental melts of ankaramite. The back-calculated melt  
20  
21 713 concentrations of trace element for the Cpx cores with the highest Mg# are used for  
22  
23 714 consideration as the parental magmas of the ankaramite, and illustrated in Fig. 12b.  
24  
25 715 The calculated parental magmas possess low REE contents with slightly right inclined  
26  
27 716 patterns of HREE (Fig. 12b), suggesting their derivation from the source region with  
28  
29 717 the presence of garnet as a residual phase. Thermobarometer calculations from the  
30  
31 718 Cpx compositions result in the potential temperature ( $T_p$ ) of the mantle source ranging  
32  
33 719 from 1267 to 1316°C (1296°C on average) and pressures of 11.6-20.0 kbar (16.6 kbar  
34  
35 720 on average), using the equation of Putirka. (2008). Thus, we propose that this rock  
36  
37 721 series is likely to be derived from a heterogeneous hydrous, garnet-hosted, mantle  
38  
39 722 source composed of lherzolite and clinopyroxenites.

### 40 723 ***Formation of sanukite***

41  
42 724 The sanukite lavas have nearly constant  $Al_2O_3$  and Sr/Y ratios over a wide range  
43  
44 725 of  $SiO_2$ . The absence of an obvious Eu negative anomaly suggests insignificant

fractional crystallization of plagioclase. However, the decreased MgO, (Fe<sub>2</sub>O<sub>3</sub>)<sub>T</sub>, and CaO with increasing SiO<sub>2</sub>, together with the correlations between Cr-Ni, and Cr-V, are consistent with the fractional crystallization of pyroxene and hornblende (Fig. 9).

Sanukite and the equivalent of sanukitoids found in Setouchi volcanic belt, SW Japan, are one type of the known high-Mg andesite (Mg#>64, Tatsumi, 2006). They are likely to represent little differentiated, near-primitive andesite magmas generated in the presence of sufficient H<sub>2</sub>O by equilibrium reaction of a hot mantle peridotite with a silicic melt derived from partial melting of a subducting sediments and/or the oceanic slab (e.g., Yogodzinski et al., 1994; Shimoda et al., 1998). As mentioned above, the studied sanukite lavas are similar in major and trace element composition to sanukite or sanukitoids. As shown in Fig. 10a-c, the addition of sediment-derived silicic melts rather than aqueous fluids are required for the petrogenesis of the sanukite samples. Furthermore, sanukite samples tend to have more radiogenic Sr-Nd-Hf isotopic compositions than other lavas in this study, suggesting a higher degree of source mixing with a metasomatic agent. The two-end-member mixing model of Sr-Nd isotopes for sanukite samples restrict the amount of additional sediment-derived melts in the mantle source to 8-12% (Fig. 11b). Meanwhile, the Hf-Nd isotopical data are consistent with the mixing model of Sr-Nd isotopes between the sediment-derived melts and the mantle wedge, requiring 10-15% addition of metasomatic melts with 9:1 mixture of sediments vs. altered oceanic crust (Fig. 11c). Compared with adakites, the sanukite samples have transitional Sr/Y ratios of 17.5-39.9 (Fig. 9f) between adakites and typical arc magmas, implying that the

subducted slab or sediments may have melted at depths shallower than the garnet stability field.

### **The heterogeneity of the mantle source: depleted vs. plume-enriched**

Primitive arc magmas, i.e. the boninites, ankaramites and sanukites of this study, are in principle ideal probes of sub-arc mantle sources (Falloon & Danyushevsky, 2000; Green et al., 2004; Mitchell & Grove, 2015; B  nard et al., 2017). Although the Lajishan-Yongjing volcanic rocks exhibit large variations in major and trace element compositions, most primitive samples have obvious geochemical signatures including high MgO contents with corresponding Mg# values, Cr and Ni concentrations, implying their derivation from partial melting of mantle source(s). Elemental and isotopic variations show the heterogeneity of mantle sources among the different rock series. The boninite lavas are derived from a depleted mantle source composed of refractory, spinel-hosted, Cpx-poor lherzolite or harzburgite. In contrast, the ankaramite lavas are derived from a heterogeneous garnet-hosted, mantle lherzolite mixed with amphibole-bearing clinopyroxenites.

Pyroxenites have been widely described either in an arc environment or in a plume-enriched intraplate mantle, and are interpreted either as lower crustal Cpx-rich cumulates from the deep arc crust, or as metasomatic rocks in the mantle on account of metasomatism from slab-derived components or plume-related components (e.g. Greene et al., 2006; Berly et al., 2006; Ishikawa et al., 2004; Sobolev et al., 2005). Specifically, the OIB-type enriched mantle source that had melt components

incorporated into it before onset of subduction would form a secondary pyroxenitic source (Sobolev et al., 2005), which is consistent with the observed coarse-grained pyroxenite in the lower part of the Lajishan-Yongjing lithologic sequence (not shown). Such situations are documented for the mantle sources beneath the Ontong Java Plateau (Ishikawa et al., 2004) and Hawaii (Sobolev et al., 2005). Even though the mechanism of Amphibole-clinopyroxenites heterogeneities in the mantle wedge could originate by density-driven delamination of lower crustal cumulates consisting of clinopyroxene + amphibole  $\pm$  olivine (Sorbadere et al., 2013), there is geochemical evidence that the Cpx-phyric ankaramite-basaltic andesites are derived from the same or similar plume-enriched mantle source for lavas from the adjacent Lajishan-Yongjing Oceanic Plateau (Zhang et al., 2017). The direct evidence is that the ankaramites plot between the alkaline basalt and picrite samples from the Lajishan-Yongjing Ophiolite and show similar patterns except for the Nb-Ta depletion and U enrichment; their La/Nb-La/Ta ratios show transitional values between OIB-MORB and normal intra-oceanic arc basalt worldwide (Fig. 12b). The high TiO<sub>2</sub> contents of both Cr-spinel inclusion and Cpx (Fig. 5a and 6a), relative to those from normal forearc peridotite and island-arc volcanics, suggest that the primitive magmas are derived from a Ti-rich mantle source. In addition, the positive correlation for TiO<sub>2</sub> and Al<sub>2</sub>O<sub>3</sub> contents of Cr-spinel from boninite (15LJ-12), enriched-boninite (15LJ-15) to ankaramite (13QLS-68, 72) form an obvious trend toward the Lajishan-Yongjing Oceanic Plateau (Fig. 5a), showing increasing influence of the plume-enriched mantle source. In contrast, the decreased Cr# of chrome spinel from those samples show the

1  
2  
3  
4 791 decreased degree of partial melting of mantle source. In terms of whole rock Sr-Nd  
5  
6 792 isotopic compositions, the  $\epsilon_{\text{Nd}}(t)$  values of ankaramite (and the derivative high-Mg  
7  
8 793 basaltic andesite and high-Al andesite lavas) are slightly lower than those from  
9  
10  
11 794 boninite lavas (Fig. 11b), which may reflect an enriched mantle source prior to or  
12  
13 795 during the contamination of slab-derived component.

14  
15  
16 796 In conclusion, we have identified three primitive melt compositions from the  
17  
18 797 same arc: boninite, ankaramite, and sanukite - all of which were generated at roughly  
19  
20 798 the same time interval. The diversity of the studied primitive rocks can be attributed  
21  
22 799 to heterogeneous mantle sources and variable degrees of mantle metasomatism by  
23  
24 800 sediment-derived hydrous fluids or silicic melts. Partial melting of the oceanic crust  
25  
26  
27 801 and its overlying oceanic sediments would produce the aqueous fluids or silicic melts,  
28  
29 802 which are enriched in fluid mobile incompatible elements solely (e.g. U, Ba) or with  
30  
31 803 less fluid-soluble incompatible elements (e.g. Th, LREE), with various radiogenic  
32  
33 804 Sr-Nd-Hf-O isotope compositions. Different amounts of slab-derived components in  
34  
35  
36 805 different proportions of fluids versus melts would incorporate into, and then react  
37  
38 806 with the overlying mantle wedge. Due to the plume-related metasomatism before the  
39  
40  
41 807 onset of subduction, the subarc mantle source(s) in SQAB is likely to be of spatially  
42  
43 808 compositional heterogeneity, and thus capable of producing various primitive arc  
44  
45  
46 809 magmas. Subsequently, the primitive arc magmas are likely to have undergone  
47  
48  
49 810 secondary AFC process during their ascent *en route* to the surface.



811     **Tectonic implications**

812     *The geodynamic setting of intra-oceanic island arc: interaction between oceanic arc*  
813     *and oceanic plateaus*

814         Accretion of an oceanic plateau to a continental margin would require that it was  
815         transferred from an oceanic to a continental setting by a subduction zone tectonic  
816         process (Coffin and Eldholm, 2001). Several different tectonic scenarios ranging from  
817         an entirely subducted model, partly preserved model to a totally accreted model have  
818         been proposed for the fate of oceanic plateaus on reaching subduction zones (e.g.,  
819         Saunders et al., 1996; Petterson et al., 1999; Kerr et al., 2000). The western Pacific  
820         ocean region provides abundant examples of the interaction between oceanic arcs and  
821         oceanic plateaus; the Cenozoic Circum-Pacific oceanic plateaus are now placed into  
822         intraplate settings and trapped settings where plateaus are now trapped in an  
823         intercontinental or continental margin setting by an outward subduction (Mann and  
824         Taira, 2004; Song et al., 2017). Thus, oceanic plateaus, due to their widespread  
825         distribution on the seafloor and continental-like crustal thicknesses, might be expected  
826         to behave more like continents upon reaching subduction zones, and thus accrete  
827         rather than subduct (Nur and Ben-Avraham, 1982; Niu et al., 2017). Transference and  
828         polarity reversal are distinguished as two subclasses of the induced nucleation model  
829         where the newly formed subduction zone(s) were respectively moved to the outboard  
830         of the failed ones and behind the magmatic arc (Stern 2004, 2010). Accordingly, an  
831         oceanic plateau is an important candidate for the formation of an intra-oceanic island  
832         arc and can be preserved as fragments (Niu et al., 2003, 2017).

The geodynamic setting of the Lajishan-Yongjing Terrane of the Qi-Qin Accretionary Belt, where an extensive ophiolite fragment, island arc volcanic complex and arc-related plutonism are juxtaposed, has long been the subject of research and debate. Recent investigations suggest this accretionary belt composes two distinct components (1) the Cambrian (>500 Ma) ophiolite complex with picrites and OIB-type lavas that represent an oceanic plateau (Hou et al., 2005; Zhang et al., 2017; Song et al., 2017; Yang et al., 2018); and (2) the Ordovician (< 470 Ma) island arc complex in this study. As shown in Fig. 13, the Lajishan-Yongjing ophiolites were the products of a Cambrian mantle plume as an oceanic plateau in the Proto-Tethys Ocean, and were accreted as an ophiolitic component in the accretionary belt (Zhang et al., 2017; Song et al., 2017). Subsequently, as argued above, the Lajishan-Yongjing arc volcanic system could be considered as a newly-formed island arc system erupting along the oceanic plateau margins in response to the collision between the oceanic plateau and the pre-existing trench/continental margin. In situ zircon U-Pb data reveal that the Lajishan-Yongjing arc volcanic system formed at ~460-440 Ma, much younger than the ophiolite fragments, and thus constrains the ages of volcanism and intra-oceanic subduction of the South Qilian Ocean.

#### **Tectonic evolution from continental arc to intra-oceanic arc in North Qilian and South Qilian**

The mechanisms of evolution from continental arc to intra-oceanic arc include: (1) trench retreat with the corresponding extension of overriding plate and subsequent opening of a back-arc basin resulting from slab rollback, and (2) trench jamming

related to the incorporation of an oceanic plateau or a microcontinent. In Fig. 13, based on the studied rock assemblages, the NQAB was determined to be an Andean-type active continental margin with the development of a back-arc basin in the Early Paleozoic era, recording a subduction history of the Qilian Ocean beneath the Alax Block (Wu et al., 1993; Song et al., 2006, 2009, 2013; Zhang et al., 2007). The development of a back-arc basin in NQAB (~510-450 Ma) is due to the separation of continental fragments as a result of slab rollback at the continental margin (Xia et al., 2012; Song et al., 2013). In contrast, the SQAB is recognized as an Early Paleozoic subduction accretionary belt, formed by accretion of plume-type ophiolite fragments (LYOP: Zhang et al., 2017) with outward eruption of intra-oceanic arc volcanics as well as intrusion of arc-related plutons at ca. 460-440 Ma. The accretion of oceanic plateau and trench jamming are the main reason for the cessation of the existing subduction zone and initiation of a new intra-oceanic island arc. Therefore, in the Early Paleozoic subduction history of the Qilian Ocean, evolution from continental margin to oceanic island-arc can be attributed to trench retreat in the NQAB and trench jamming in the SQAB, respectively.

**CONCLUSIONS**

Five distinct rock lineages are recorded in the volcanic sequence in the Lajishan-Yongjing Terrane, including boninite, ankaramite, high-Mg basaltic andesite, high-Al andesite and sanukite. The assemblage shows arc-like trace element distributions and suggests an IBM-type oceanic island arc in the Early Paleozoic era.

1  
2  
3  
4 876 The enriched Sr-Nd and decoupled Hf-Nd isotopic systems, as well as anomalous  
5  
6 877 zircon  $\delta^{18}\text{O}$  values suggest the incorporation of subducted oceanic sediments into their  
7  
8 878 mantle source. The boninites are derived from the refractory, Cpx-poor spinel  
9  
10  
11 879 lherzolite or harzburgite. The ankaramite and high-Mg basaltic andesite, are likely to  
12  
13 880 be derived from OIB- enriched, garnet-hosted, pyroxenitic-peridotitic mixed mantle;  
14  
15 881 the high-Al andesite is the evolved magma after precipitation of Cpx. The sanukite  
16  
17 882 could be generated by the equilibrium reaction of a mantle peridotite with a silicic  
18  
19 883 melt derived from partial melting of subducted sediments. Large compositional  
20  
21 884 variations in the volcanic sequence from the same arc over such a short time interval  
22  
23 885 show that oceanic-arc magmas derived from a significantly heterogeneous mantle  
24  
25 886 source simultaneously, accompanied by secondary AFC process during their ascent *en*  
26  
27 887 *route* to the surface.

28  
29  
30  
31  
32  
33 888 The generation of the arc volcanic sequence in the Lajishan-Yongjing accretionary  
34  
35 889 belt is a response to the collision between the Lajishan-Yongjing ocean plateau and  
36  
37 890 the pre-existing trench/continental margin. Zircon ages of ~440-460 Ma constrain the  
38  
39 891 age of volcanism, as well as the intra-oceanic subduction of Qilian Ocean. In the early  
40  
41 892 Paleozoic subduction history of the Qilian Ocean, two mechanisms can be responsible  
42  
43 893 for the evolution from continental margin to oceanic island-arc, including trench  
44  
45 894 retreating in NQAB and trench jamming in SQAB, respectively.

## 50 51 895 **ACKNOWLEDGEMENTS**

52  
53  
54 896 The authors wish to thank H. Y. Zhang for helping with whole-rock analyses, G.B.

897 Zhang and W. P. Zhu for helping with Sr-Nd isotope analyses, J. Li and Y. G. Li for  
898 helping with zircon SIMS/LA-ICP-MS U-Pb dating analysis and zircon Hf-O isotope  
899 analysis, X. L. Li and H.Y. Zhang for helping with mineral analysis. The authors are  
900 grateful to Editor John Gamble, Rod Sewell and one anonymous reviewer for their  
901 detailed and constructive peer-review comments, which greatly improved the quality  
902 of this paper.

903 **FUNDING**

904 This study was supported by the National Natural Science Foundation of China  
905 (Grant 40572040), and the Major State Basic Research Development Program  
906 (2015CB856105).

907 **REFERENCES**

908 Andersen, T. (2002). Correction of common lead in U-Pb analyses that do not report  
909 <sup>204</sup>Pb. *Chemical Geology* **192**, 59-79.

910 Barsdell, M. & Berry, R. F. (1990). Origin and evolution of primitive island-arc  
911 ankaramites from Western Epi, Vanuatu. *Journal of Petrology* **31**, 747-777.

912 Bebout, G.E. (2014). Chemical and Isotopic Cycling in Subduction Zones. In:  
913 Turekian, K. K. & Holland, H. D. (eds) *Treatise of Geochemistry, The Crust*, 2nd  
914 ed. Elsevier, pp. 703-747.

915 Bénard, A., Nebel, O., Ionov, D.A., Arculus, R.J., Shimizu, N. & Métrich, N. (2017).  
916 Primary silica-rich picrite and high-Ca boninite melt inclusions in pyroxenite

- veins from the Kamchatka sub-arc mantle. *Journal of Petrology* **57**, 1955-1982.
- Berly, T.J., Hermann, J., Arculus, R.J. & Lapierre, H. (2006). Supra-subduction Zone Pyroxenites from San Jorge and Santa Isabel (Solomon Islands). *Journal of Petrology* **47**, 1531-1555.
- Bezard, R., Turner, S., Davidson, J. P., Macpherson, C. G. & Lindsay, J. M. (2015). Seeing through the effects of crustal assimilation to assess the source composition beneath the Southern Lesser Antilles Arc. *Journal of Petrology* **56**, 815-844.
- Bindeman, I. N., Eiler, J. M., Yogodzinski, G. M., Tatsumi, Y., Stern, C. R., Grove, T. L., Portnyagin, M., Hoernle, K. & Danyushevsky, L. V. (2005). Oxygen isotope evidence for slab melting in modern and ancient subduction zones. *Earth and Planetary Science Letters* **235**, 480-496.
- Bizimis, M., Salters, V. J. M. & Dawson, J. B. (2003). The brevity of carbonatite sources in the mantle: evidence from Hf isotopes. *Contributions to Mineralogy and Petrology* **145**, 281-300.
- Blichert-Toft, J. & Albarède, F. (1997). The Lu-Hf isotope geochemistry of chondrites and the evolution of the mantle-crust system. *Earth and Planetary Science Letters* **148**, 243-258.
- Cao, Y., Song, S. G., Su, L., Jung, H. & Niu, Y. L. (2016). Highly refractory peridotites in Songshugou, Qinling orogen: Insights into partial melting and melt/fluid-rock reactions in forearc mantle. *Lithos* **252-253**, 234-254.

- 938 Cawood, P.A., Kroner, A., Collins, W.J., Kusky, T.M., Mooney, W.D. & Windley, B.F.  
939 (2009). Accretionary orogens through Earth history: *Geological Society of*  
940 *London Special Publications* **318**, 1-36.
- 941 Chauvel, C., Lewin, E., Carpentier, M., Arndt, N. T. & Marini, J. C. (2008). Role of  
942 recycled oceanic basalt and sediment in generating the Hf-Nd mantle array.  
943 *Nature Geoscience* **1**, 64-67.
- 944 Choi, H. O., Choi, S. H., Lee, D. C. & Kang, H. C. (2013). Geochemical evolution of  
945 basaltic volcanism within the Tertiary basins of southeastern Korea and the  
946 opening of the East Sea (Sea of Japan). *Journal of Volcanology & Geothermal*  
947 *Research* **249**, 109-122.
- 948 Choi, S. H. & Mukasa, S. B. (2012). Lu-Hf and Sm-Nd isotope systematics of Korean  
949 spinel peridotites: A case for metasomatically induced Nd-Hf decoupling. *Lithos*  
950 **154**, 263-276.
- 951 Chu, N. C., Taylor, R. N., Chavagnac, V., Nesbitt, R. W., Boella, R. M., Milton, J. A.,  
952 Germain, C. R., Bayon, G. & Burton, K. (2002). Hf isotope ratio analysis using  
953 multi-collector inductively coupled plasma mass spectrometry: An evaluation of  
954 isobaric interference corrections. *Journal of Analytical Atomic Spectrometry* **17**,  
955 1567-1574.
- 956 Coffin, M. & Eldholm, O. (2001). Large igneous provinces: progenitors of some  
957 ophiolites? In: Ernst, R., Buchan, K. (Eds.), *Mantle Plumes: Their Identification*  
958 *through Time. Geological Society of America Special Paper* **352**, 59-70.

- 959 Condie, K.C. (2001). Mantle Plumes and their Record in Earth History. Cambridge:  
960 Cambridge University Press, 306 pp.
- 961 Condie K., C. (2014). Growth of continental crust: a balance between preservation  
962 and recycling. *Mineralogical Magazine* **78**, 623-638.
- 963 Crawford, A.J., Falloon, T.J. & Eggins, S. (1987). The origin of island arc  
964 high-alumina basalts. *Contributions to Mineralogy and Petrology* **97**, 417-430.
- 965 Crawford, A. J., Falloon, T. J. & Green, D. H. (1989). Classification, petrogenesis and  
966 tectonic setting of boninites. In: Crawford, A. J. (ed.) Boninites and Related  
967 Rocks. Unwin Hyman, pp. 1-49.
- 968 Dick, H.J.B. & Bullen, T. (1984). Chromian spinel as a petrogenetic indicator in  
969 abyssal and alpine-type peridotites and spatially associated lavas. *Contributions*  
970 *to Mineralogy and Petrology* **86**, 54-76.
- 971 Elburg, M.A., Kamenetsky, V.S., Foden, J.D. & Sobolev, A. (2007). The origin of  
972 medium-K ankaramitic arc magmas from Lombok (Sunda arc, Indonesia):  
973 Mineral and melt inclusion evidence. *Chemical Geology* **240**, 260-279.
- 974 Falloon, T. J. & Danyushevsky, L. V. (2000). Melting of refractory mantle at 1.5, 2.0  
975 and 2.5 GPa under H<sub>2</sub>O-undersaturated conditions: implications for the  
976 petrogenesis of high-Ca boninites and the influence of subduction components  
977 on mantle melting. *Journal of Petrology* **41**, 257-283.
- 978 Fu, C. L., Yan, Z., Guo, X. Q., Niu, M. L., Xia, W. J., Wang, Z. Q. & Li, J. L. (2014).



- 979 Geochemistry and SHRIMP zircon U-Pb age of diabases in the Lajishankou  
980 ophiolitic mélange, South Qilian terrane. *Acta Petrologica Sinica* **30**, 1695-1706  
981 (in Chinese with English abstract).
- 982 Gehrels, G. E., Yin, A. & Wang, X. F. (2003). Detrital-zircon geochronology of the  
983 northeastern Tibetan plateau. *Geological Society of America Bulletin* **115**,  
984 881-896.
- 985 Gill, J. B. (1981). Orogenic andesites and plate tectonics. In: El Goresy, A., von  
986 Engelhardt, W. & Hahn, T. (eds) Minerals and Rocks. Springer, 390 pp.
- 987 Green, D. H., Schmidt, M. W. & Hibberson, W. O. (2004). Island-arc ankaramites:  
988 primitive melts from fluxed refractory lherzolitic mantle. *Journal of Petrology* **45**,  
989 391-403.
- 990 Greene, A. R., Debari, S. M., Kelemen, P. B., Blusztajn, J. & Clift, P. D. (2006). A  
991 detailed geochemical study of island arc crust: the Talkeetna arc section,  
992 South-Central Alaska. *Journal of Petrology* **47**, 1051-10093.
- 993 Griffin, W.L., Belousova, E.A., Shee, S.R., Pearson, N.J. & O'Reilly, S.Y. (2004).  
994 Archean crustal evolution in the northern Yilgarn Craton: U-Pb and Hf-isotope  
995 evidence from detrital zircons. *Precambrian Research* **131**, 231-282.
- 996 Griffin, W. L., Pearson, N. J., Belousova, E., Jackson, S. E., van Acherbergh, E.,  
997 O'Reilly, S. Y., & Shee, S. R. (2000). The Hf isotope composition of cratonic  
998 mantle: LA-MC-ICP-MS analysis of zircon megacrysts in kimberlites.  
999 *Geochimica et Cosmochimica Acta* **64**, 133-147.

- 1  
2  
3  
4 1000 Hanyu, T., Tatsumi, Y., Nakai, S. I., Chang, Q., Miyazaki, T., Sato, K., Tani, K.,  
5  
6 1001 Shibata, T. & Yoshida, T. (2006). Contribution of slab melting and slab  
7  
8 1002 dehydration to magmatism in the NE Japan arc for the last 25 Myr: Constraints  
9  
10 1003 from geochemistry. *Geochemistry Geophysics Geosystems* **7**, 1-29.  
11  
12  
13  
14 1004 Hou, K. J., Li, Y. H., Zou, T. R., Qu, X. M., Shi, Y. R. & Xie, G. Q. (2007). Laser  
15  
16 1005 ablation-MC-ICP-MS technique for Hf isotope microanalysis of zircon and its  
17  
18 1006 geological applications. *Acta Petrologica Sinica* **23**, 2595-2604 (in Chinese with  
19  
20 1007 English abstract)  
21  
22  
23  
24 1008 Hou Q. Y., Zhao, Z.D., Zhang, H. F., Zhang, B. R., Zhang, L. & Chen, Y. L. (2005).  
25  
26 1009 Discussion on the tectonic affinity of ancient oceanic mantle in Western  
27  
28 1010 Qinling-Songpan continental tectonic node, China: From elemental and  
29  
30 1011 Sr-Nd-Pb isotopic evidences, *Acta Petrologica Sinica* **22**, 2901-2909 (in Chinese  
31  
32 1012 with English abstract).  
33  
34  
35  
36  
37 1013 Iizuka, T., & Hirata, T. (2005). Improvements of precision and accuracy in in situ hf  
38  
39 1014 isotope microanalysis of zircon using the laser ablation-MC-ICPMS technique.  
40  
41 1015 *Chemical Geology* **220**, 121-137.  
42  
43  
44  
45 1016 Ishikawa, A., Maruyama, S. & Komiya, T. (2004). Layered lithospheric mantle  
46  
47 1017 beneath the Ontong Java Plateau: Implications from xenoliths in alnoite, Malaita,  
48  
49 1018 Solomon Islands. *Journal of Petrology* **45**, 2011-2044.  
50  
51  
52  
53 1019 Jacobsen, S. B., & Wasserburg, G. J. (1984). Sm-Nd isotopic evolution of chondrites.  
54  
55 1020 *Earth and Planetary Science Letters* **50**, 139-155.  
56  
57  
58  
59  
60

- 1  
2  
3  
4 1021 Kamenetsky, V.S., Crawford, A.J. & Meffre, S. (2001). Factors controlling chemistry  
5  
6 1022 of magmatic spinel: an empirical study of associated olivine, Cr-spinel and melt  
7  
8 1023 inclusions from primitive rocks. *Journal of Petrology* **42**, 655-671.  
9  
10  
11 1024 Kelemen, P. B., Hanghøj, K. & Greene, A. R. (2003). One view of the geochemistry  
12  
13 1025 of subduction-related magmatic arcs with an emphasis on primitive andesite and  
14  
15 1026 lower crust. In: Holland, H. D. & Turekian, K. K. (eds) *Treatise on Geochemistry*,  
16  
17 1027 Vol. 4, the Crust. Elsevier, pp. 749-806.  
18  
19  
20  
21 1028 Kelemen, P. B., Shimizu, N. & Salters, V. M. (1995). Extraction of mid-ocean-ridge  
22  
23 1029 basalt from the upwelling mantle by focused flow of melt in dunite channels.  
24  
25 1030 *Nature* **375**, 747-753.  
26  
27  
28  
29 1031 Kerr, A., White, R. & Saunders, A. (2000). LIP reading: recognizing oceanic plateau  
30  
31 1032 in the geological record. *Journal of Petrology* **41**, 1041-1056  
32  
33  
34  
35 1033 Le Maitre, R. W. (2002). *Igneous Rocks: a Classification and Glossary of Terms:*  
36  
37 1034 *Recommendations of the International Union of Geological Sciences*  
38  
39 1035 *Subcommission on the Systematics of Igneous Rocks*. Cambridge: Cambridge  
40  
41 1036 University Press, 236 pp.  
42  
43  
44  
45 1037 Leeman, W. P. (1983). The influence of crustal structure on compositions of  
46  
47 1038 subduction-related magmas. *Journal of Volcanology & Geothermal Research* **18**,  
48  
49 1039 561-588.  
50  
51  
52  
53 1040 Li, X. H., Liu, Y., Li, Q. L., Guo, C. & Chamberlain, K. R. (2013a). Correction to  
54  
55 1041 "Precise determination of Phanerozoic zircon Pb/Pb age by multi collector SIMS  
56  
57  
58  
59  
60

- without external standardization". *Geochemistry Geophysics Geosystems* **10**, 573-575.
- Li, X. H., Tang, G. Q., Gong, B., Yang, Y. H., Hou, K. J., Hu, Z. C., Li, Q. L., Liu, Y. & Li, W. X. (2013b). Qinghu zircon: A working reference for micro beam analysis of U-Pb age and Hf and O isotopes. *Science Bulletin* **58**, 4647-4654.
- Li, X. H., Li, W. X., Li, Q. L., Wang, X. C., Liu, Y. & Yang, Y. H. (2010a). Petrogenesis and tectonic significance of the 850 Ma Gangbian alkaline complex in South China: evidence from in situ zircon U-Pb dating, Hf-O isotopes and whole rock geochemistry. *Lithos* **114**, 1-15.
- Li, X. H., Long, W. G., Li, Q. L., Liu, Y., Zheng, Y. F., Yang, Y. H., Chamberlain, K. R., Wan, D. F., Guo, C. H., Wang, X. C. & Tao, H. (2010b). Penglai zircon megacrysts: a potential new working reference material for microbeam determination of Hf-O isotopes and U-Pb age. *Geostandards and Geoanalytical Research* **34**, 117-134.
- Liu, Y.J., Neubauer, F., Genser, J., Takasu, A., Ge, X. H. & Handler, R. (2006).  $^{40}\text{Ar}/^{39}\text{Ar}$  ages of blueschist facies pelitic schists from Qingshuigou in the Northern Qilian Mountains, western China. *Island Arc* **15**, 187-198.
- Ludwig, K. R. (2003), User's Manual for Isoplot 3.00: A Geochronological Toolkit for Microsoft Excel, Spec. Publ., vol. 4, Berkeley Geochronology Center, Berkeley.
- Mann, P. & Taira, A. (2004). Global tectonic significance of the Solomon Islands and Ontong Java Plateau convergent zone. *Tectonophysics* **389**, 137-190.

- 1063 Marchesi, C., Garrido, C. J., Godard, M., Belley, F. & Ferré, E. (2009). Migration and  
1064 accumulation of ultra-depleted subduction-related melts in the Massif du Sud  
1065 ophiolite (New Caledonia). *Chemical Geology* **266**, 171-186.
- 1066 Médard, E., Schmidt, M.W., Schiano, P. & Ottolini, L. (2006). Melting of  
1067 Amphibole-bearing Wehrlites: an Experimental Study on the Origin of  
1068 Ultra-calcic Nepheline-normative Melts. *Journal of Petrology* **47**, 481-504.
- 1069 Mitchell A. L. & Grove T. L. (2015). Melting the hydrous, subarc mantle: the origin  
1070 of primitive andesites. *Contributions to Mineralogy and Petrology* **170**, 13, doi:  
1071 10.1007/s00410-015-1161-4.
- 1072 Miyashiro, A. (1974). Volcanic rock series in island arcs and active continental  
1073 margins. *American Journal of Science* **274**, 321-355.
- 1074 Morel, M. L. A., Nebel, O., Nebel-Jacobsen, Y. J., Miller, J. S. & Vroon, P. Z. (2008).  
1075 Hafnium isotope characterization of the GJ-1 zircon reference material by  
1076 solution and laser ablation MC-ICPMS. *Chemical Geology* **255**, 231-235.
- 1077 Nielsen, R. L., Forsythe, L. M., Gallahan, W. E. & Fisk, M. R. (1994). Major- and  
1078 trace-element magnetite-melt equilibria. *Chemical Geology* **117**, 167-191.
- 1079 Niu, Y. L. (1997). Mantle melting and melt extraction processes beneath ocean ridges:  
1080 Evidence from abyssal peridotites. *Journal of Petrology* **38**, 1047-1074.
- 1081 Niu, Y. L. (2004). Bulk-rock major and trace element compositions of abyssal  
1082 peridotites: Implications for mantle melting, melt extraction and post-melting

- 1083 processes beneath mid-ocean ridges. *Journal of Petrology* **45**, 2423-2458.
- 1084 Niu, Y. L., Shi, X. F., Li, T. G., Wu, S. G., Sun, W. D. & Zhu R.X. (2017). Testing the  
1085 mantle plume hypothesis: An IODP effort to drill into the Kamchatka-Okhotsk  
1086 Sea basement. *Science Bulletin* **62**, 1464-1472.
- 1087 Niu, Y. L., O'Hara, M. J. & Pearce, J. A. (2003). Initiation of subduction zones as a  
1088 consequence of lateral compositional buoyancy contrast within the lithosphere: a  
1089 petrological perspective. *Journal of Petrology* **44**, 764-778.
- 1090 Nur, A. & Ben-Avraham, Z. (1982). Oceanic plateaus, the fragmentation of continents,  
1091 and mountain building. *Journal of Geophysical Research* **87**, 3644-3661.
- 1092 Pearce, J. A. (2008). Geochemical fingerprinting of oceanic basalts with applications  
1093 to ophiolite classification and the search for Archean oceanic crust. *Lithos* **100**,  
1094 14-48.
- 1095 Pearce, J. A., Kempton, P. D., Nowell, G. M. & Noble, S. R. (1999). Hf-Nd element  
1096 and isotope perspective on the nature and provenance of mantle and subduction  
1097 components in Western Pacific arc-basin systems. *Journal of Petrology* **40**,  
1098 1579-1611.
- 1099 Pearce, T. H., Gorman, B. E. & Birkett, T. C. (1977). The relationship between major  
1100 element chemistry and tectonic environment of basic and intermediate volcanic  
1101 rocks. *Earth and Planetary Science Letters* **36**, 121-132.
- 1102 Petterson, M., Babbs, T., Neal, C., Mahoney, J., Saunders, A., Duncan, R., Tolia, D.,

- 1103 Magu, R., Qopoto, C., Mahoa, H. & Natogga, D. (1999). Geological-tectonic  
1104 framework of Solomon Islands, SW Pacific: crustal accretion and growth within  
1105 an intra-oceanic setting. *Tectonophysics* **301**, 35-60.
- 1106 Rohrbach, A., Schuth, S., Ballhaus, C., Münker, C., Matveev, S. & Qopoto, C. (2005).  
1107 Petrological constraints on the origin of arc picrites, New Georgia Group,  
1108 Solomon Islands. *Contributions to Mineralogy and Petrology* **149**, 685-698.
- 1109 Putirka, K.D. (2008). Thermometers and Barometers for Volcanic Systems. In: Putirka,  
1110 K. D. & Tepley, F. J., 3rd (eds) Mineral, Inclusions and Volcanic Process.  
1111 Mineralogical Society of America and Geochemical Society, *Reviews in*  
1112 *Mineralogy and Geochemistry* **69**, 61-120.
- 1113 Rudnick, R. L. & Gao, S. (2003). Composition of the continental crust. In: Rudnick, R.  
1114 L. (ed.) The Crust. vol. 3, Elsevier, pp. 1-64.
- 1115 Saunders, A., Tarney, J., Kerr, A. & Kent, R. (1996). The formation and fate of large  
1116 oceanic, igneous provinces. *Lithos* **37**, 81-95.
- 1117 Scherer, E., Munker, C. & Mezger, K. (2001). Calibration of the lutetium-hafnium  
1118 clock. *Science* **293**, 683-687.
- 1119 Schiano, P., Eiler, J.M., Hutcheon, I.D. & Stolper, E.M. (2000). Primitive CaO - rich,  
1120 silica - undersaturated melts in island arcs: Evidence for the involvement of  
1121 clinopyroxene - rich lithologies in the petrogenesis of arc magmas.  
1122 *Geochemistry Geophysics Geosystems*, **1**, doi: 10.1029/1999GC000032.

- 1123 Shimoda, G., Tatsumi, Y., Nohda, S., Ishizaka, K. & Jahn, B.M. (1998). Setouchi  
1124 high-Mg andesites revisited: geochemical evidence for melting of subducting  
1125 sediments. *Earth and Planetary Science Letters* **160**, 479-492.
- 1126 Sláma, J., Košler, J., Condon, D.J., Crowley, J.L., Gerdes, A., Hanchar, J.M.,  
1127 Horstwood, M.S.A., Morris, G.A., Nasdala, L. & Norberg, N. (2008). Plešovice  
1128 zircon - A new natural reference material for U–Pb and Hf isotopic microanalysis.  
1129 *Chemical Geology* **249**, 1-35.
- 1130 Sobolev, A. V., Hofmann, Albrecht, W., Stephan, V., Nikogosian & Igor, K. (2005).  
1131 An olivine-free mantle source of Hawaiian shield basalts. *Nature* **434**, 590-597.
- 1132 Song, S. G., Zhang, L. F., Niu, Y. L., Su, L., Song, B. & Liu, D. Y. (2006). Evolution  
1133 from oceanic subduction to continental collision: a case study of the Northern  
1134 Tibetan Plateau inferred from geochemical and geochronological data. *Journal of*  
1135 *Petrology* **47**, 435-455.
- 1136 Song, S. G., Niu, Y. L., Zhang, L. F., Wei, C. J., Liou, J. & Su, L. (2009). Tectonic  
1137 evolution of Early Paleozoic HP metamorphic rocks in the North Qilian  
1138 Mountains, NW China: new perspectives. *Journal of Asian Earth Sciences* **35**,  
1139 334-353.
- 1140 Song, S. G., Su, L., Li, X. H., Zhang, G. B., Niu, Y. L. & Zhang, L. F. (2010). Tracing  
1141 the 850-Ma continental flood basalts from a piece of subducted continental crust  
1142 in the North Qaidam UHPM belt, NW China. *Precambrian Research* **183**,  
1143 805-816.



1144 Song, S. G., Su, L., Li, X. H., Niu, Y. L. & Zhang, L. F. (2012). Grenville-age  
1145 orogenesis in the Qaidam-Qilian block: The link between South China and Tarim.  
1146 *Precambrian Research* **220-221**, 9-22.

1147 Song, S.G., Niu, Y. L., Su, L. & Xia, X. H. (2013). Tectonics of the North Qilian  
1148 orogen, NW China. *Gondwana Research* **23**, 1378-1401.

1149 Song, S. G., Niu, Y. L., Su, L., Zhang, C. & Zhang, L. F. (2014). Continental  
1150 orogenesis from ocean subduction, continent collision/subduction, to orogen  
1151 collapse, and orogen recycling: The example of the North Qaidam UHPM belt,  
1152 NW China. *Earth-Science Reviews* **129**, 59-84.

1153 Song, S. G., Yang, L. M., Zhang, Y. Q., Niu, Y. L., Wang, C., Su, L. & Gao, Y. L.  
1154 (2017). Qi-Qin Accretionary Belt in Central China Orogen: accretion by trench  
1155 jam of oceanic plateau and formation of intra-oceanic arc in the Early Paleozoic  
1156 Qin-Qi-Kun Ocean. *Science Bulletin* **62**, 1035-1038.

1157 Sorbadere, F., Médard, E., Laporte, D. & Schiano, P. (2013). Experimental melting of  
1158 hydrous peridotite-pyroxenite mixed sources: Constraints on the genesis of  
1159 silica-undersaturated magmas beneath volcanic arcs. *Earth and Planetary  
1160 Science Letters* **384**, 42-56.

1161 Sorbadere, F., Schiano, P. & Métrich, N. (2012). Constraints on the origin of  
1162 nepheline-normative primitive magmas in island arcs inferred from  
1163 olivine-hosted melt inclusion compositions. *Journal of Petrology* **54**, 215-233.

1164 Stacey, J. S. & Kramers, J. D. (1975). Approximation of terrestrial lead isotope

- 1  
2  
3  
4 1165 evolution by a two-stage model. *Earth and Planetary Science Letters* **26**,  
5  
6 1166 207-221.  
7  
8  
9 1167 Stern, R. J. (2004). Subduction initiation: spontaneous and induced. *Earth and*  
10  
11 1168 *Planetary Science Letters* **226**, 275-292.  
12  
13  
14 1169 Stern, R. J. (2010). The anatomy and ontogeny of modern intra-oceanic arc systems.  
15  
16  
17 1170 *Geological Society London Special Publications* **338**, 7-34.  
18  
19  
20 1171 Stern, R. A., Hanson, G. N. & Shirey, S. B. (1989). Petrogenesis of mantle-derived,  
21  
22 1172 LILE-enriched Archean monzodiorites and trachyandesites (Sanukitoids) in  
23  
24 1173 southwestern Superior Province. *Canadian Journal of Earth Sciences* **26**,  
25  
26 1174 1688-1712.  
27  
28  
29  
30 1175 Stern, R. J., Reagan, M., Ishizuka, O., Ohara, Y. & Whattam, S. (2012). To understand  
31  
32 1176 subduction initiation, study forearc crust: To understand forearc crust, study  
33  
34 1177 ophiolites. *Lithosphere* **4**, 469-483.  
35  
36  
37  
38 1178 Sun, S.S. & McDonough, W.F. (1989). Chemical and Isotopic Systematics of Oceanic  
39  
40 1179 Basalts; Implications for Mantle Composition and Processes. *Geological Society*  
41  
42 1180 *London Special Publications* **42**, 313-345.  
43  
44  
45  
46 1181 Takashima, R., Nishi, H. & Yoshida, T. (2002). Geology, petrology and tectonic  
47  
48 1182 setting of the Late Jurassic ophiolite in Hokkaido, Japan. *Journal of Asian Earth*  
49  
50 1183 *Sciences* **21**, 197-215.  
51  
52  
53  
54 1184 Tang, G. J., Wang, Q., Wyman, D. A., Li, Z. X., Xu, Y. G. & Zhao, Z. H. (2012).  
55  
56  
57  
58  
59  
60

- 1185 Metasomatized lithosphere-asthenosphere interaction during slab roll-back:  
1186 Evidence from Late Carboniferous gabbros in the Luotuogou area, Central  
1187 Tianshan. *Lithos* **155**, 67-80.
- 1188 Tatsumi, Y. (2006). High-Mg andesites in the Setouchi Volcanic Belt, Southwest  
1189 Japan: analogy to Archean magmatism and continental crust formation? *Annual  
1190 Review of Earth & Planetary Sciences* **34**, 467-499.
- 1191 Tatsumi, Y. & Hanyu, T. (2003). Geochemical modeling of dehydration and partial  
1192 melting of subducting lithosphere: Toward a comprehensive understanding of  
1193 high-Mg andesite formation in the Setouchi volcanic belt, SW Japan.  
1194 *Geochemistry, Geophysics, Geosystems* **4**, 1081, doi: 10.1029/2003GC000530,  
1195 9.
- 1196 Till, C.B. & Withers, A.C. (2012). The beginnings of hydrous mantle wedge melting.  
1197 *Contributions to Mineralogy and Petrology* **163**, 669-688.
- 1198 Tung, K. A., Yang, H. Y., Liu, D. Y., Zhang, J. X., Yang, H. J., Shau, Y. H. & Tseng, C.  
1199 Y. (2013). The Neoproterozoic granitoids from the Qilian block, NW China:  
1200 Evidence for a link between the Qilian and South China blocks. *Precambrian  
1201 Research* **235**, 163-189.
- 1202 Tung, K., Yang, H. J., Yang, H. Y., Liu, D. Y., Zhang, J. X., Wan, Y. S. & Tseng, C. Y.  
1203 (2007). SHRIMP U-Pb geochronology of the zircons from the Precambrian  
1204 basement of the Qilian Block and its geological significances. *Chinese Science  
1205 Bulletin* **52**, 2687-2701.

- 1  
2  
3  
4 1206 Valley, J. W., Lackey, J. S., Cavosie, A. J., Clechenko, C. C., Spicuzza, M. J., Basei,  
5  
6 1207 M. A. S., Bindeman, I. N., Ferreira, V. P., Sial, A. N. & King, E. M. (2005). 4.4  
7  
8 1208 billion years of crustal maturation: oxygen isotope ratios of magmatic zircon.  
9  
10  
11 1209 *Contributions to Mineralogy and Petrology* **150**, 561-580.  
12  
13  
14 1210 Valley, J.W. (2003). Oxygen isotopes in zircon. In: Hanchar, J.M., Hoskin, P.W.O.  
15  
16 1211 (Eds.), *Zircon. Reviews to Mineralogy and Geochemistry* **53**, pp. 343-385.  
17  
18  
19 1212 Vervoort, J. D., Plank, T. & Prytulak, J. (2011). The Hf-Nd isotopic composition of  
20  
21 1213 marine sediments. *Geochimica et Cosmochimica Acta* **75**, 5903-5926.  
22  
23  
24 1214 Villa, I.M., De Bièvre, P., Holden, N.E. & Renne, P.R. (2015). IUPAC-IUGS  
25  
26 1215 recommendation on the half life of <sup>87</sup>Rb. *Geochimica et Cosmochimica Acta*  
27  
28 1216 **164**, 382-385.  
29  
30  
31  
32 1217 Wan, Y. S., Xu, Z. Q., Yang, J. S. & Zhang, J. X. (2001). Ages and compositions of  
33  
34 1218 the Precambrian high-grade basement of the Qilian terrane and its adjacent areas.  
35  
36 1219 *Acta Geological Sinica (English edition)* **75**, 375-384.  
37  
38  
39  
40 1220 Wang, H., Wu, Y. B., Li, C. R., Zhao, T. Y., Qin, Z. W., Zhu, L. Q., Gao, S., Zheng, J.  
41  
42 1221 P., Liu, X. M. & Zhou, L. (2014). Recycling of sediment into the mantle source  
43  
44 1222 of K-rich mafic rocks: Sr-Nd-Hf-O isotopic evidence from the Fushui complex  
45  
46 1223 in the Qinling orogen. *Contributions to Mineralogy and Petrology* **168**, 1062, doi  
47  
48 1224 10.1007/s00410-014-1062-y.  
49  
50  
51  
52  
53 1225 Wang, T., Wang, Z. Q., Yan, Z., Ma, Z. H., He, S. F., Fu, C. L. & Wang, D. S. (2016).  
54  
55 1226 Geochronological and Geochemical evidence of amphibolite from the Hualong  
56  
57  
58  
59  
60

- 1227 Group, northwest China: Implication for the early Paleozoic accretionary  
1228 tectonics of the Central Qilian belt. *Lithos* **248-251**, 12-21.
- 1229 White, W. M. (2010). Oceanic Island Basalts and Mantle Plumes: The Geochemical  
1230 Perspective. *Annual Review of Earth & Planetary Sciences* **38**, 133-160.
- 1231 Wiedenbeck, M., Allé, P., Corfu, F., Griffin, W. L., Meier, M., Oberli, F., Quadt, A. V.,  
1232 Roddick, J. C. & Spiegel, W. (1995). Three natural zircon standards for U–Th–  
1233 Pb, Lu–Hf, trace-element and REE analyses. *Geostandards Newsletter* **19**, 1-23.
- 1234 Winchester, J. A. & Floyd, P. A. (1977). Geochemical discrimination of different  
1235 magma series and their differentiation products using immobile elements.  
1236 *Chemical Geology* **20**, 325-343.
- 1237 Wood, D. A. (1980). The application of a Th Hf Ta diagram to problems of  
1238 tectonomagmatic classification and to establishing the nature of crustal  
1239 contamination of basaltic lavas of the British Tertiary Volcanic Province. *Earth  
1240 and Planetary Science Letters* **50**, 11-30.
- 1241 Workman, R. K. & Hart, S. R. (2005). Major and trace element composition of the  
1242 depleted MORB mantle (DMM). *Earth and Planetary Science Letters* **231**,  
1243 53-72.
- 1244 Wu, F. Y., Yang, Y. H., Xie, L. W., Yang, J. H. & Xu, P. (2006). Hf isotopic  
1245 compositions of the standard zircons and baddeleyites used in U–Pb  
1246 geochronology. *Chemical Geology* **234**, 105-126.

- 1247 Wu, H.Q., Feng, Y.M. & Song, S.G., 1993. Metamorphism and deformation of  
1248 blueschist belts and their tectonic implications, North Qilian Mountains, China.  
1249 *Journal of Metamorphic Geology* **11**, 523-536.
- 1250 Wu, Y. B., Gao, S., Zhang, H. F., Yang, S. H., Jiao, W. F., Liu, Y. S. & Yuan, H. L.  
1251 (2008). Timing of UHP metamorphism in the Hong'an area, western Dabie  
1252 Mountains, China: evidence from zircon U-Pb age, trace element and Hf isotope  
1253 composition. *Contributions to Mineralogy and Petrology* **155**, 123-133.
- 1254 Xia, X. H., Song, S. G. & Niu, Y. L. (2012). Tholeiite-Boninite terrane in the North  
1255 Qilian suture zone: Implications for subduction initiation and back-arc basin  
1256 development. *Chemical Geology* **328**, 259-277.
- 1257 Xiao, W. J., Windley, B. F., Yong, Y., Yan, Z., Yuan, C., Liu, C. Z. & Li, J. L. (2009).  
1258 Early Paleozoic to Devonian multiple-accretionary model for the Qilian Shan,  
1259 NW China. *Journal of Asian Earth Sciences* **35**, 323-333.
- 1260 Yan, Z., Aitchison, J., Fu, C. L., Guo, X. Q., Niu, M. L., Xia, W. J. & Li, J. L. (2015).  
1261 Hualong Complex, South Qilian terrane: U-Pb and Lu-Hf constraints on  
1262 Neoproterozoic micro-continental fragments accreted to the northern  
1263 Proto-Tethyan margin. *Precambrian Research* **266**, 65-85.
- 1264 Yan, Z., Wang, Z. & Li, J. L. (2012). Tectonic settings and accretionary orogenesis of  
1265 the West Qinling Terrane, northeastern margin of the Tibet Plateau. *Acta*  
1266 *Petrologica Sinica* **28**, 1808-1828.
- 1267 Yang, J. S., Xu, Z. Q., Zhang, J. X., Song, S. G., Wu, C., Shi, R. D., Li, H. & Brunel,

- 1268 M. (2002). Early Palaeozoic North Qaidam UHP metamorphic belt on the  
1269 north-eastern Tibetan plateau and a paired subduction model. *Terra Nova* **14**,  
1270 397-404.
- 1271 Yang, L.M., Song, S.G., Allen, M. B., Su, L., Dong, J.L. & Wang, C. (2018). Oceanic  
1272 accretionary belt in the West Qinling Orogen: Links between the Qinling and  
1273 Qilian orogens, China. *Gondwana Research* **64**, 137-162.
- 1274 Yogodzinski, G.M., Volynets, O.N., Koloskov, A.V., Seliverstov, N.I. & Matvenkov,  
1275 V.V. (1994). Magnesian Andesites and the Subduction Component in a Strongly  
1276 Calc-Alkaline Series at Piip Volcano, Far Western Aleutians. *Journal of*  
1277 *Petrology* **35**, 163-204.
- 1278 Zhang, J. X., Meng, F. C. & Wan, Y. S. (2007). A cold Early Palaeozoic subduction  
1279 zone in the North Qilian Mountains, NW China: petrological and U-Pb  
1280 geochronological constraints. *Journal of Metamorphic Geology* **25**, 285-304.
- 1281 Zhang, J. X., Wan, Y. S., Xu, Z. Q., Yang, J. S. & Meng, F. C. (2001). Discovery of  
1282 basic granulite and its formation age in Delingha area, North Qaidam Mountains.  
1283 *Acta Petrologica Sinica* **17**, 453-458
- 1284 Zhang, Y. Q., Song, S. G., Yang, L. M., Su, L., Niu, Y. L., Allen, M. B. & Xu, X.  
1285 (2017). Basalts and picrites from a plume-type ophiolite in the South Qilian  
1286 Accretionary Belt, Qilian Orogen: Accretion of a Cambrian Oceanic Plateau?  
1287 *Lithos* **278-281**, 97-110.
- 1288 Zheng, Y. -F. & Hermann, J. (2014). Geochemistry of continental subduction-zone

1289 fluids. *Earth, Planets and Space* **66**, 93; doi: 10.1186/1880-5981-66-93.

1290

For Peer Review



**Figures and figure captions**

**Fig. 1.** (a) Schematic map showing major tectonic units of China [modified after Song et al. (2017)]. (b) Simplified geological map of the Central China Orogenic Belt [modified after Song et al. (2017)]. (c) Simplified geological map of the Lajishan-Yongjing Terrane and sample locations: LK-Lajishankou, XX-Xiongxiang, CP-Chapu, ZB-Zhaba, SHN-Sihaning, MC-Machang, YCT-Yaocaotai and YJ-Yongjing. (d) Zhaba cross-section of the Lajishan Terrane.

**Fig. 2.** Representative field photographs and microphotographs of island-arc volcanic rocks from the Lajishan-Yongjing Terrane: (a) Pillow boninite; (b) Reddish, massive andesite with plagioclase phenocrysts; (c) Dark-colored intermediate-basic lavas overlain by light-colored felsic lavas (sanukite); (d) Volcanic breccia; (e) Boninite (sample LJ15-12); (f) Ankaramite (sample 13QLS-71); (g) High-Mg basaltic andesite (sample LJ15-40); (h) High-Al andesite (sample LJ15-18); and (i) Sanukite (sample 12LJ-13). Cpx-clinopyroxene; Sp-spinel; Pl-plagioclase.

**Fig. 3.** (a) TAS diagram (Le Maitre, 2002); (b) SiO<sub>2</sub>- Zr/TiO<sub>2</sub> diagram (Winchester & Floyd, 1977); (c) AFM diagram (Pearce et al., 1977); and (d) Hf-Th-Ta diagram (Wood, 1980).

**Fig. 4.** Chondrite-normalized REE patterns (a, c, e and g) and Primitive mantle (PM)-normalized multi-element patterns (b, d, f and h) for the Lajishan-Yongjing island-arc volcanic rocks. Normalization and OIB values are from Sun & McDonough, (1989). Values of sanukitoids in Setouchi Volcanic Belt (SVB) for comparison are from Tatsumi et al. (2003).

**Fig. 5.** Compositional variations of Cr-spinel in island-arc volcanic rocks from the Lajishan-Yongjing Terrane. (a)  $\text{Al}_2\text{O}_3$  vs.  $\text{TiO}_2$  diagram (Kamenetsky et al., 2001) and (b) Cr# vs. Mg# diagram (Dick and Bullen, 1984). Cr-Spinel data of Lajishan-Yongjing Ophiolite (LYO), Hawaiian OIB (HO) are from Zhang et al. (2017) and reference therein.

**Fig. 6.** Compositional variations of Cpx in island-arc volcanic rocks from the Lajishan-Yongjing Terrane. Fields of Cpx compositions for ocean ridge cumulates, Izu-Bonin arc volcanic rocks, island-arc cumulates (lower crustal gabbro-norites) and depleted fore-arc peridotites are from Marchesi et al. (2009) and references therein.

**Fig. 7.** Concordia diagrams of zircon U-Pb isotope data analyzed with SIMS and LA-ICP-MS for island-arc volcanic rocks from the Lajishan-Yongjing Terrane.

**Fig. 8.** (a) La/Sm vs. La (ppm); (b) La/Sm vs.  $\text{SiO}_2$  (wt. %); (c)  $(^{87}\text{Sr}/^{86}\text{Sr})_i$  -  $\text{SiO}_2$  (wt. %); and (d)  $\epsilon_{\text{Nd}}(t)$  -  $\text{SiO}_2$  (wt. %). Data of UCC (upper continental crust) and GLOSS (Global Subducting Sediments) for comparison are respective from Rudnick and Gao, (2003) and Bebout, (2014). The grey squares are the average sediment data from different island arc systems (Bebout, 2014).

**Fig. 9.** Bulk-rock major and trace element (ratios) variation diagrams for island-arc volcanic rocks from the Lajishan-Yongjing Terrane. The information to device the vectors on these figures is from Beier et al. (2016) and Greene et al. (2006).

**Fig. 10.** (a) Th/Yb-Nb/Yb diagram (Pearce, 2008); Plots of Ba/Th (b) and U/Th (c) vs. chondrite-normalized La/Sm.

1335

**Fig. 11.** (a) Zircon O isotopic compositions for island-arc volcanic rocks from the Lajishan-Yongjing Terrane. Data source: the mantle  $\delta^{18}\text{O}$  value ( $5.3 \pm 0.3\%$ , [Valley, 2003](#)); Pelagic sediments and Terrigenous sediments ( $\delta^{18}\text{O} = 9\text{-}20\%$ , [Bindeman et al., 2005](#); [Chauvel et al., 2008](#); [Vervoort et al., 2011](#)). (b) Sr-Nd isotopic compositions for the Lajishan-Yongjing volcanic rocks in the two-component mixing models. Data sources: field labelled MORB and sediments from Barbados, DSDP sites 144 and 543 are from [Bezard et al. \(2015\)](#) and reference therein. The OIB data are from [White, \(2010\)](#). The Lajishan OPB data without the altered samples are from [Zhang et al. \(2017\)](#). (c) Nd-Hf isotopic compositions for the Lajishan-Yongjing volcanic rocks in the mixing model between the mantle wedge (MW), subducted altered oceanic crust (AOC) and oceanic sediments assuming slab dehydration and melting. The dashed mixing trajectories are between mantle wedge and these different fluxing agents. The pink area is restricted by the mixing trajectories of zircon-barren pelagic sediment-derived fluids and melts. The blue area is restricted by the mixing trajectories of terrigenous sediment-derived melts and 90% terrigenous sediment-derived melts + 10% AOC-derived melts. Numbers along the pink and blue mixing trajectories are the amount of the crust-derived input and numbers along the gray lines are the proportion of AOC component. The end-member compositions are from [Hanyu et al. \(2006\)](#) and listed in Appendix Table 6. The  $I_{\text{Sr}}$  and  $\epsilon_{\text{Nd}}(t)$  values of sediments are from the measured interlayered sedimentary rocks from the Lajishan-Yongjing volcanic rocks, and the  $\epsilon_{\text{Hf}}(t)$  values for the pelagic clay sediments

(PS:  $\varepsilon_{\text{Hf}}(t)=0.99 \times \varepsilon_{\text{Nd}}(t)+5.34$ ) and terrigenous sediments (TS:  $\varepsilon_{\text{Hf}}(t)=1.55 \times \varepsilon_{\text{Nd}}(t)+1.21$ ) are calculated using the sediments arrays recommended by [Vervoort et al. \(2011\)](#) and [Wang et al. \(2014\)](#), respectively. Symbols are bigger than the maximum analytical error isotope on isotope data, except where shown.

1361

**Fig. 12.** Primitive mantle (PM)-normalized trace element patterns for the average compositions of (a) boninite, (b) primitive ankaramite and the calculated parental magmas of Cpx-phyric basaltic andesite in Lajishan-Yongjing Terrane. The average compositions of boninite are from near-primitive samples (15LJ-13, 16LJ-07, 09 and 15) with high Mg# of 74-80; the average compositions of ankaramite are from samples of 13QLS-68-72 (Mg#=77-79). (a) Grey dashed lines represent the liquids produced by aggregated fractional melting of the depleted DMM source and the numbers represent melting degree of mantle ([Workman & Hart, 2005](#)). Data for comparison are: the OIB, E-MORB, N-MORB ([Sun & McDonough., 1989](#)) and the average composition of boninite worldwide ([Kelemen et al., 2003](#)). (b) The calculated parental magmas are based on the trace element data of high Mg# Cpx phenocryst from Cpx-phyric basaltic andesite sample (13QLS-124); the amounts of Cpx phenocryst are assumed to range from 0 to 40 wt. %, and Clinopyroxene/melt partition coefficients ( $K_D$ ) and their references are listed in [Appendix Table 3](#). Data for comparison are the island arc volcanics ([Kelemen et al., 2003](#)), and the LYO (Lajishan-Yongjing Ophiolite) picrites and alkaline basalts ([Zhang et al., 2017](#)).

**Fig. 13.** Schematic cartoons illustrating the tectonic evolution of the South Qilian

1379 Accretionary Belt in the Qilian Orogen.

1380

1381 **Table 1:** Major and trace element data for volcanic rocks from the Lajishan-Yongjing

1382 Terrane.

1383 **Table 2:** Average electron microprobe analyses of Cpx for volcanic rocks from the

1384 Lajishan-Yongjing Terrane.

1385 **Table 3:** Whole-rock Sr-Nd isotopic compositions for volcanic rocks from the

1386 Lajishan-Yongjing Terrane.

1387 **Table 4:** In situ zircon O isotopic compositions for volcanic rocks from the

1388 Lajishan-Yongjing Terrane.

1389 **Appendix Table 1.** Electron microprobe analyses of Cpx for volcanic rocks from the

1390 Lajishan-Yongjing Terrane.

1391 **Appendix Table 2.** Electron microprobe analyses of Cr-spinel for volcanic rocks from

1392 the Lajishan-Yongjing Terrane.

1393 **Appendix Table 3.** LA-ICP-MS analysis of Cpx and Calculated primitive magmas

1394 for volcanic rocks from the Lajishan-Yongjing Terrane.

1395 **Appendix Table 4.** In situ U-Pb data of zircons for volcanic rocks from the

1396 Lajishan-Yongjing Terrane.

1397 **Appendix Table 5.** Zircon Hf isotopic data for volcanic rocks from the

1398 Lajishan-Yongjing Terrane.

1399 **Appendix Table 6.** The elemental and isotopic compositions of end-members using

1400 for the Sr-Nd-Hf mixing modeling.

1401 **Appendix Table 7.** Standard analyses for Major elements.

1402 **Appendix table 8.** Standard analyses for Trace elements

1403

1404 **Fig. S1.** Primitive mantle (PM)-normalized trace element patterns for the Cpx  
1405 phenocrysts of ankaramite (13QLS-72) and high-Mg basaltic andesite (13QLS-124)  
1406 from Lajishan-Yongjing Terrane.

1407 **Fig. S2.** Representative zircon Cathodoluminescence (CL) images for volcanic rocks  
1408 from the Lajishan-Yongjing Terrane. The ovals and circles on the CL images are the  
1409 respective SIMS and LA-ICPMS spots of in situ zircon U-Pb dating analyses. Also  
1410 shown are the  $^{206}\text{Pb}/^{238}\text{U}$  ages of the zircons.

1  
2  
3  
4  
5  
6  
7  
8  
9  
10  
11  
12  
13  
14  
15  
16  
17  
18  
19  
20  
21  
22  
23  
24  
25  
26  
27  
28  
29  
30  
31  
32  
33  
34  
35  
36  
37  
38  
39  
40  
41  
42  
43  
44  
45  
46  
47  
48  
49  
50  
51  
52  
53  
54  
55  
56  
57  
58  
59  
60

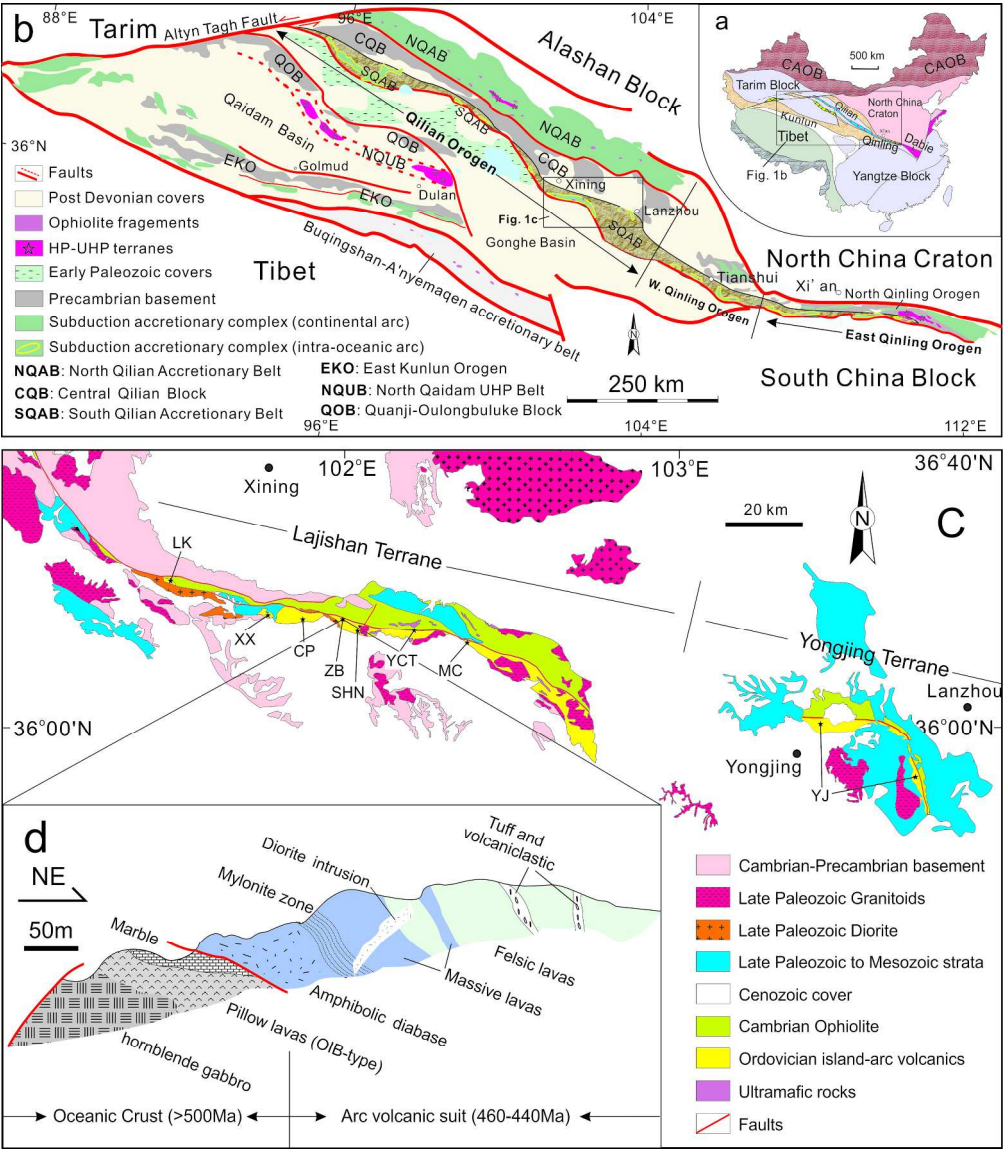


Fig. 1. (a) Schematic map showing major tectonic units of China [modified after Song et al. (2017)]. (b) Simplified geological map of the Central China Orogenic Belt [modified after Song et al. (2017)]. (c) Simplified geological map of the Lajishan-Yongjing Terrane and sample locations: LK-Lajishankou, XX-Xiong-xian, CP-Chapu, ZB-Zhaba, SHN-Sihaning, MC-Machang, YCT-Yaocaotai and YJ-Yongjing. (d) Zhaba cross-section of the Lajishan Terrane.

247x282mm (300 x 300 DPI)



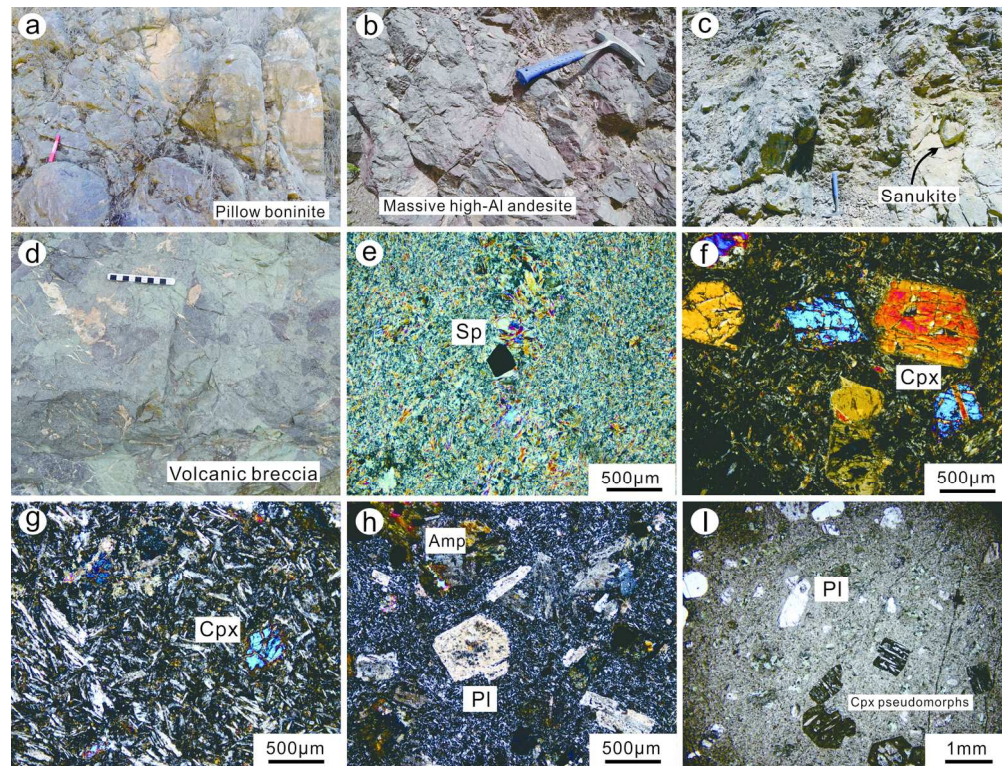


Fig. 2. Representative field photographs and microphotographs of island-arc volcanic rocks from the Lajishan-Yongjing Terrane: (a) Pillow boninite; (b) Reddish, massive andesite with plagioclase phenocrysts; (c) Dark-colored intermediate-basic lavas overlain by light-colored felsic lavas (sanukite); (d) Volcanic breccia; (e) Boninite (sample LJ15-12); (f) Ankaramite (sample 13QLS-71); (g) High-Mg basaltic andesite (sample LJ15-40); (h) High-Al andesite (sample LJ15-18); and (i) Sanukite (sample 12LJ-13). Cpx-clinopyroxene; Sp-spinel; Pl-plagioclase.

154x116mm (300 x 300 DPI)



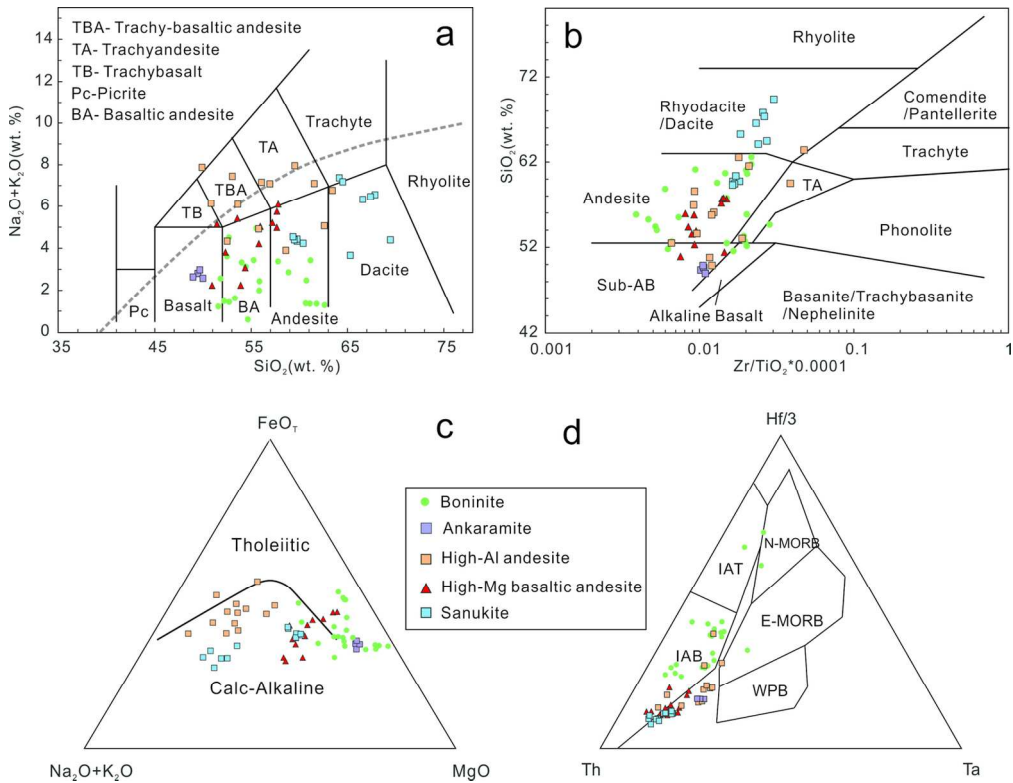


Fig. 3. (a) TAS diagram (Le Maitre, 2002); (b)  $\text{SiO}_2$ -Zr/TiO<sub>2</sub> diagram (Winchester & Floyd, 1977); (c) AFM diagram (Pearce et al., 1977); and (d) Hf-Th-Ta diagram (Wood, 1980).

140x108mm (300 x 300 DPI)

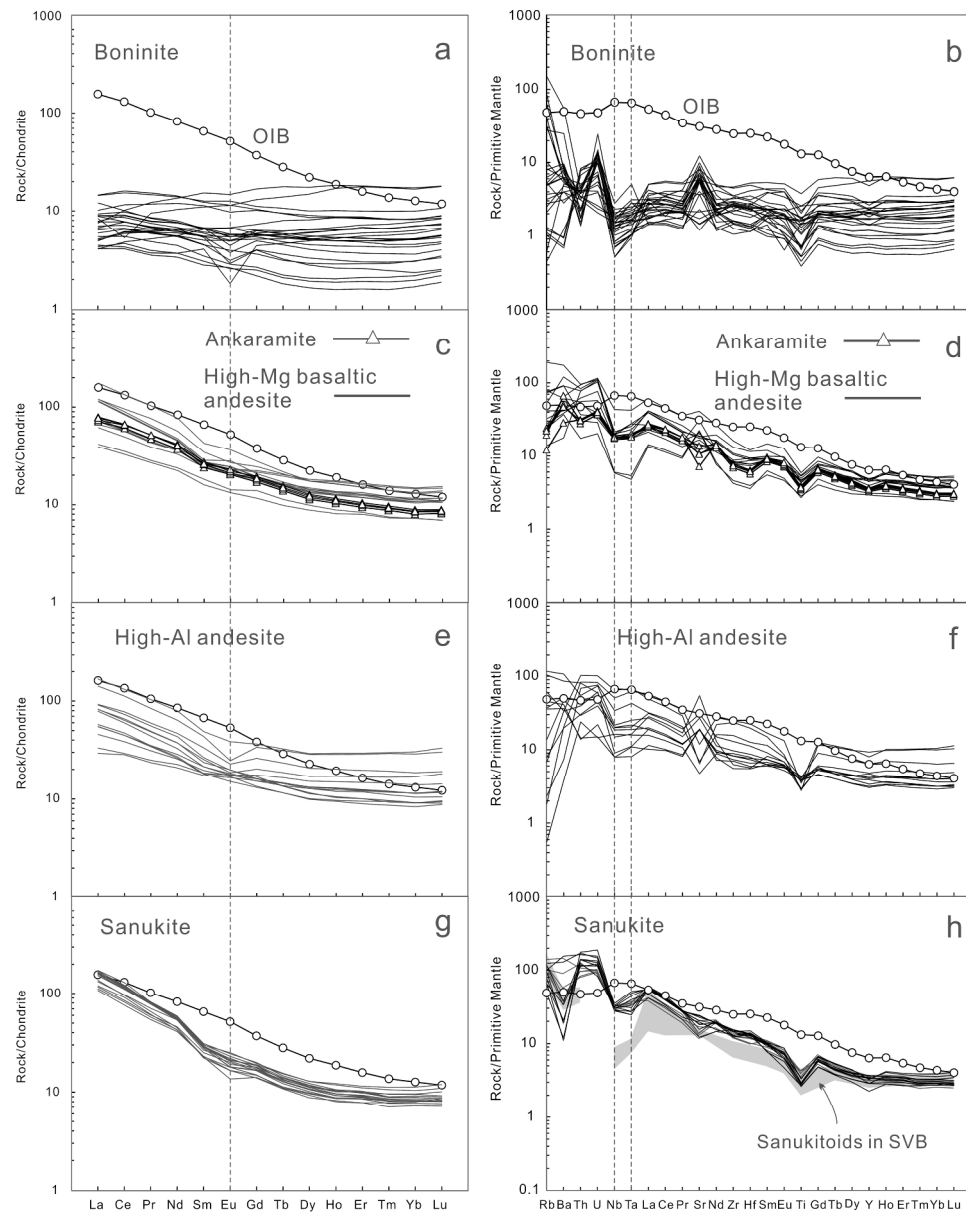


Fig. 4. Chondrite-normalized REE patterns (a, c, e and g) and Primitive mantle (PM)-normalized multi-element patterns (b, d, f and h) for the Lajishan-Yongjing island-arc volcanic rocks. Normalization and OIB values are from Sun & McDonough, (1989). Values of sanukitoids in Setouchi Volcanic Belt (SVB) for comparison are from Tatsumi et al. (2003).

251x315mm (300 x 300 DPI)

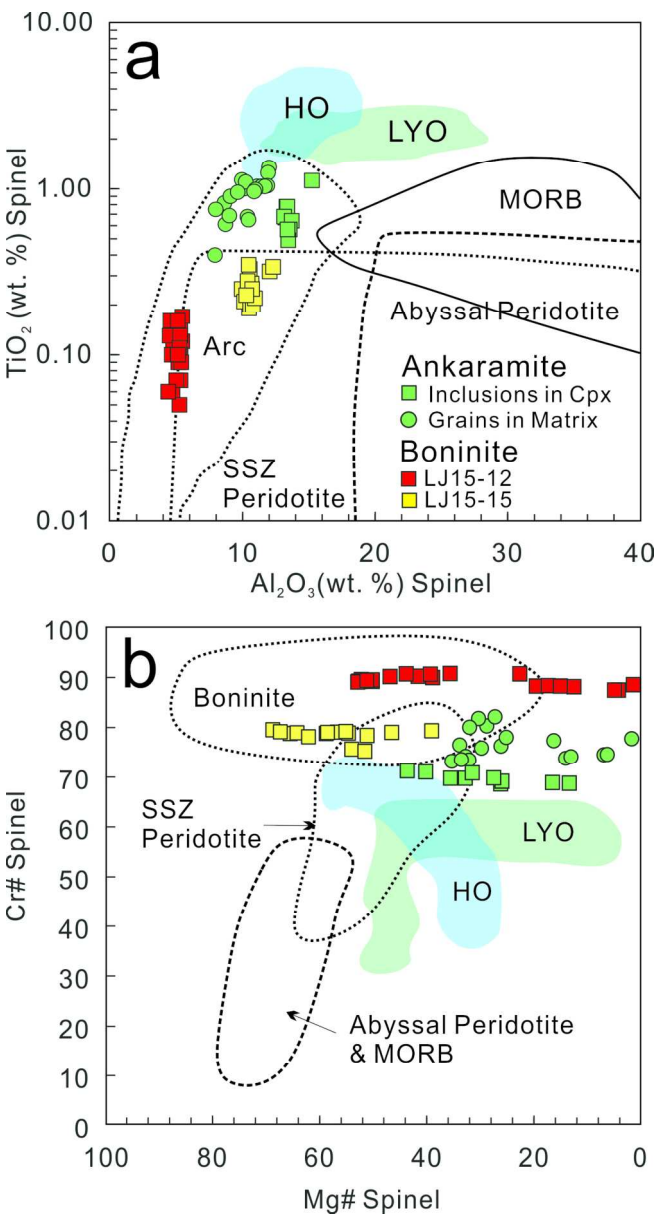


Fig. 5. Compositional variations of Cr-spinel in island-arc volcanic rocks from the Lajishan-Yongjing Terrane. (a) Al<sub>2</sub>O<sub>3</sub> vs. TiO<sub>2</sub> diagram (Kamenetsky et al., 2001) and (b) Cr# vs. Mg# diagram (Dick and Bullen, 1984). Cr-Spinel data of Lajishan-Yongjing Ophiolite (LYO), Hawaiian OIB (HO) are from Zhang et al. (2017) and reference therein.

147x274mm (300 x 300 DPI)

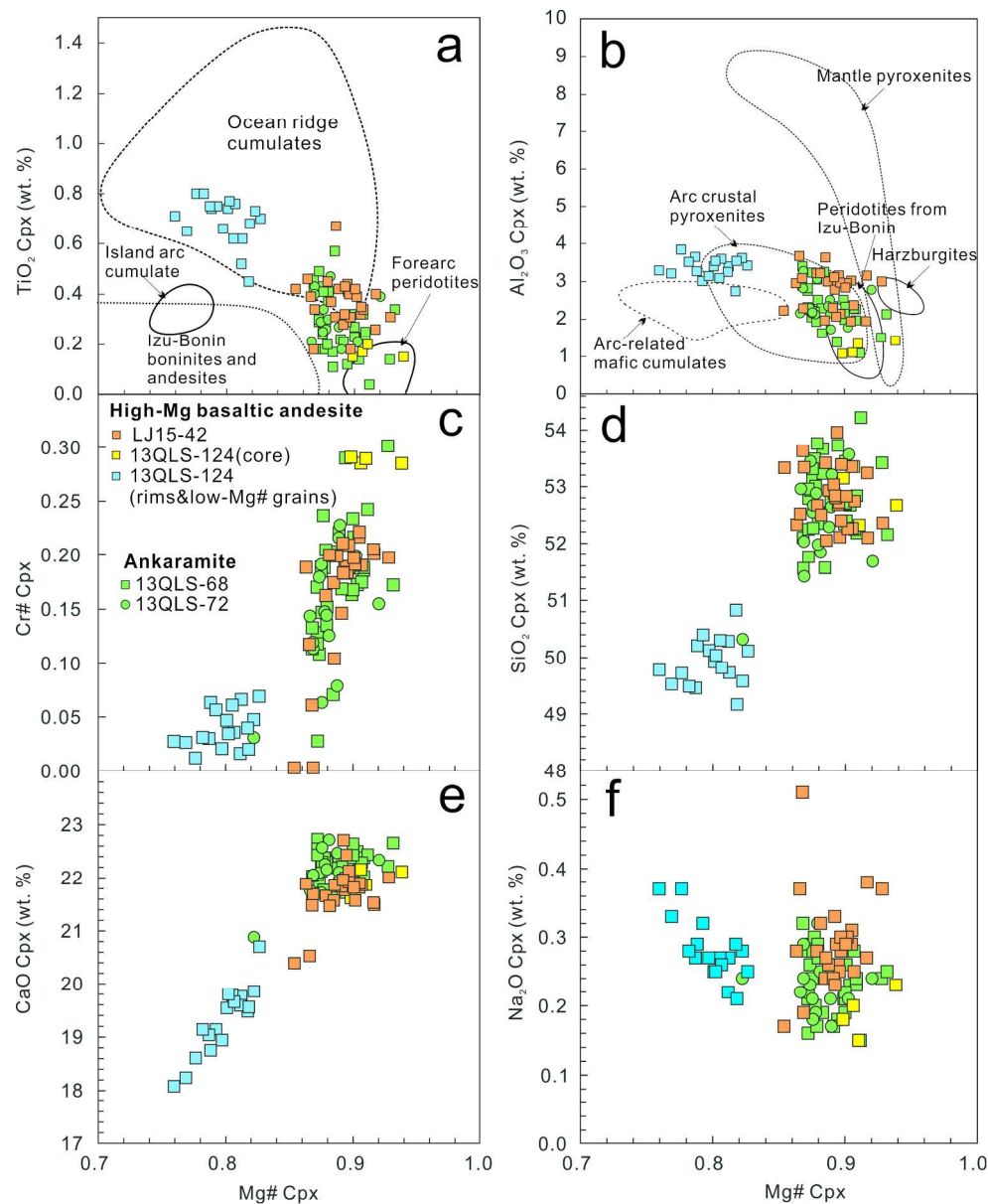


Fig. 6. Compositional variations of Cpx in island-arc volcanic rocks from the Lajishan-Yongjing Terrane. Fields of Cpx compositions for ocean ridge cumulates, Izu-Bonin arc volcanic rocks, island-arc cumulates (lower crustal gabbronorites) and depleted fore-arc peridotites are from Marchesi et al. (2009) and references therein.

221x271mm (300 x 300 DPI)

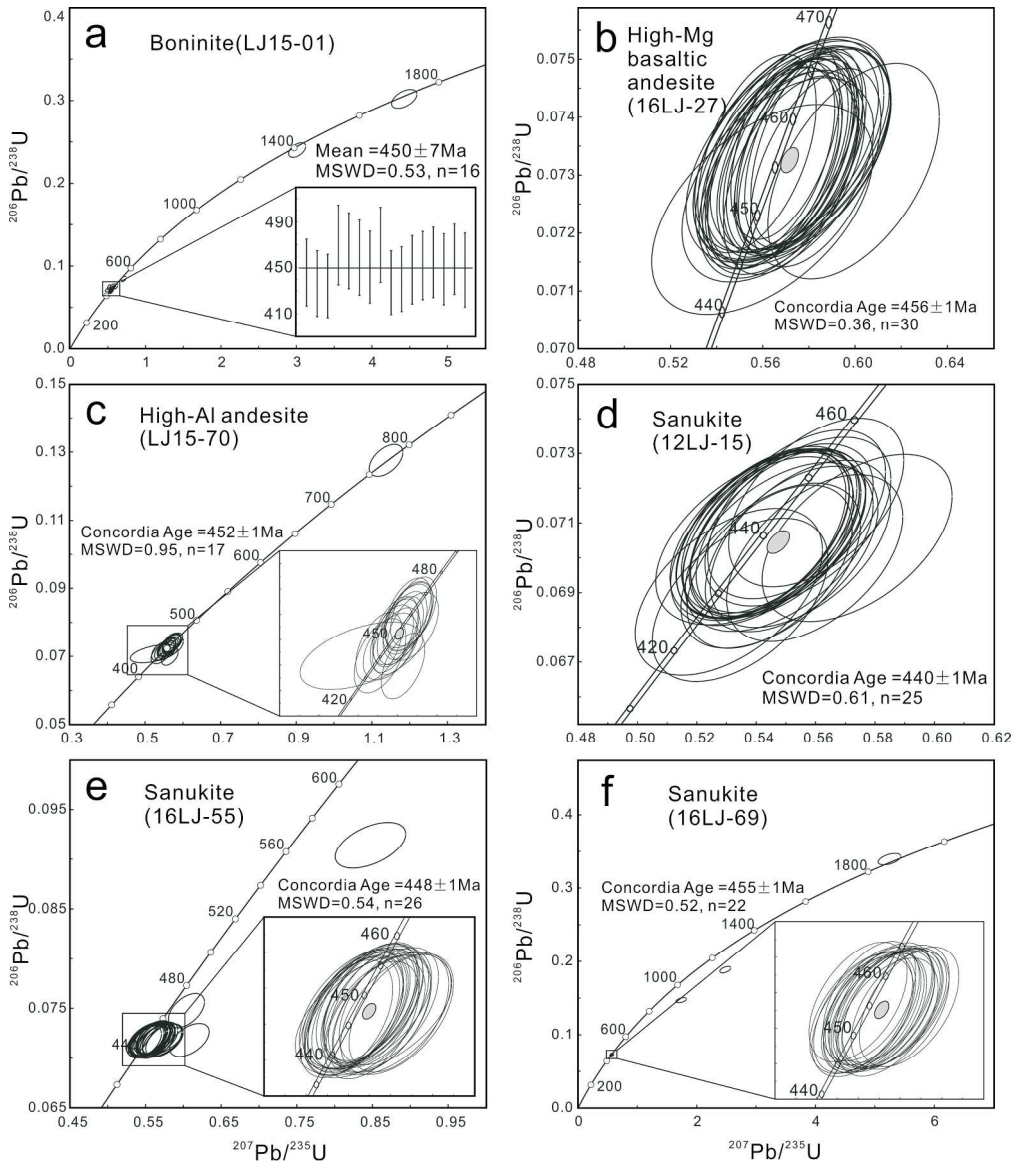


Fig. 7. Concordia diagrams of zircon U-Pb isotope data analyzed with SIMS and LA-ICP-MS for island-arc volcanic rocks from the Lajishan-Yongjing Terrane.

232x268mm (300 x 300 DPI)

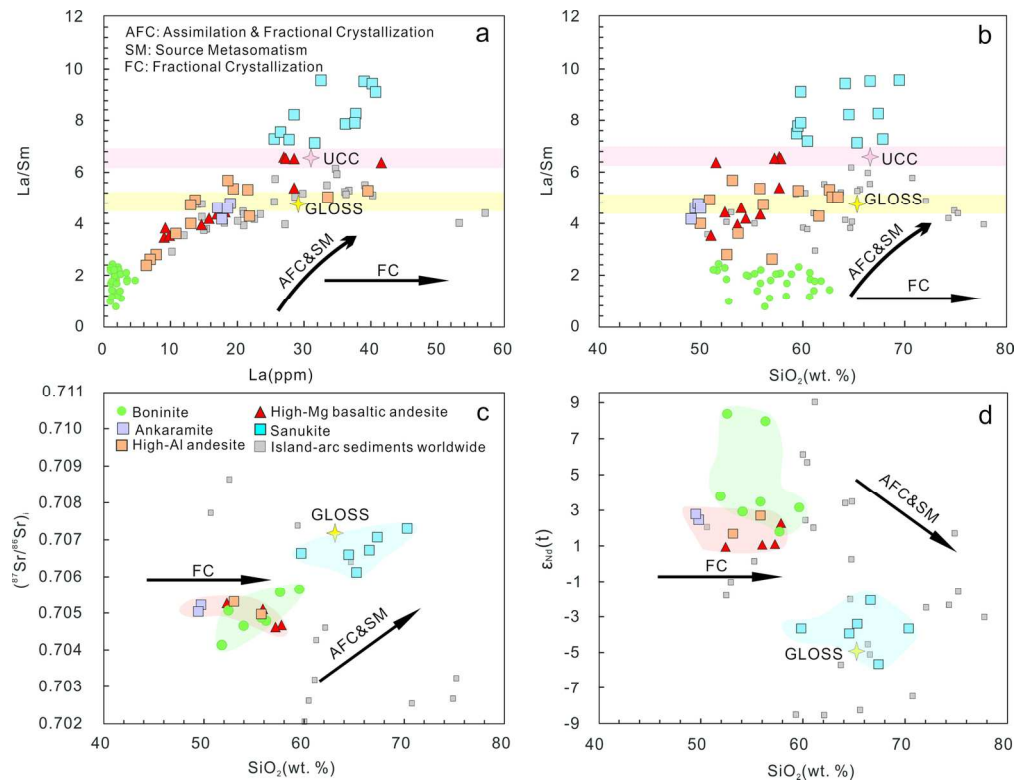


Fig. 8. (a) La/Sm vs. La (ppm); (b) La/Sm vs. SiO<sub>2</sub> (wt. %); (c) (87Sr/86Sr)<sub>i</sub> - SiO<sub>2</sub> (wt. %); and (d) ε<sub>Nd</sub>(t) - SiO<sub>2</sub> (wt. %). Data of UCC (upper continental crust) and GLOSS (Global Subducting Sediments) for comparison are respective from Rudnick and Gao, (2003) and Bebout, (2014). The grey squares are the average sediment data from different island arc systems (Bebout, 2014).

155x119mm (300 x 300 DPI)

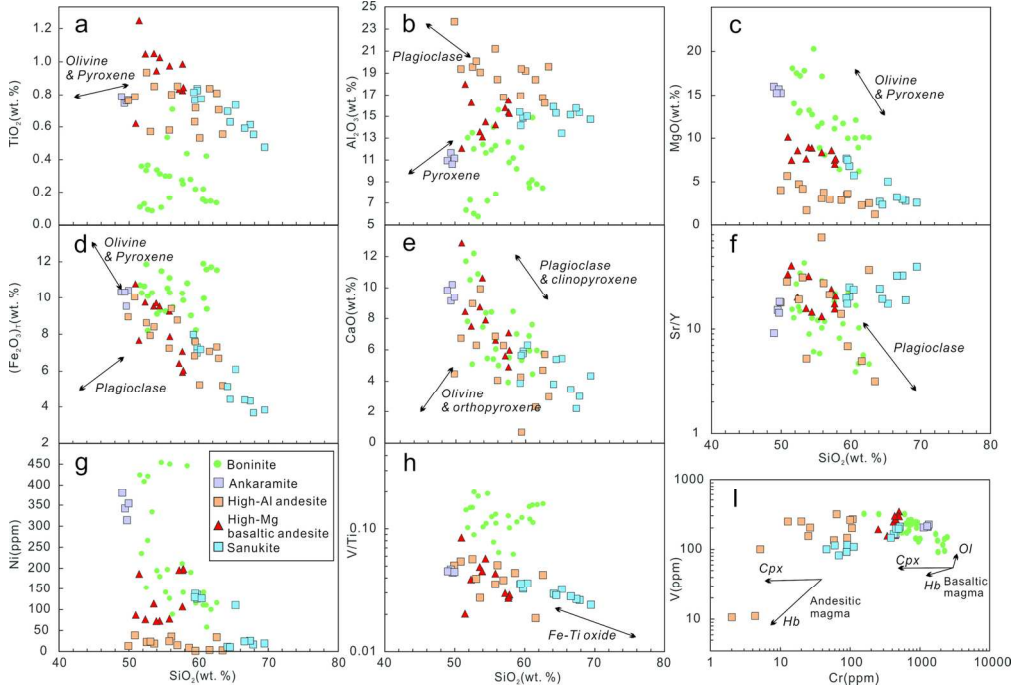


Fig. 9. Bulk-rock major and trace element (ratios) variation diagrams for island-arc volcanic rocks from the Lajishan-Yongjing Terrane. The information to devise the vectors on these figures is from Beier et al. (2016) and Greene et al. (2006).

157x107mm (300 x 300 DPI)



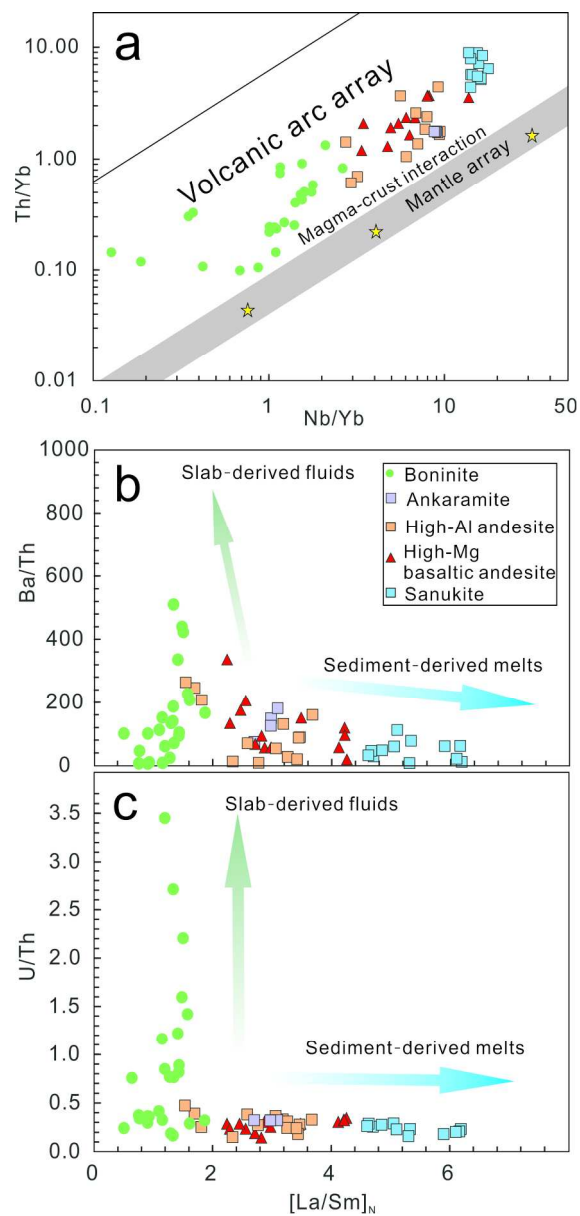


Fig. 10. (a) Th/Yb-Nb/Yb diagram (Pearce, 2008); Plots of Ba/Th (b) and U/Th (c) vs. chondrite-normalized La/Sm.

203x435mm (300 x 300 DPI)



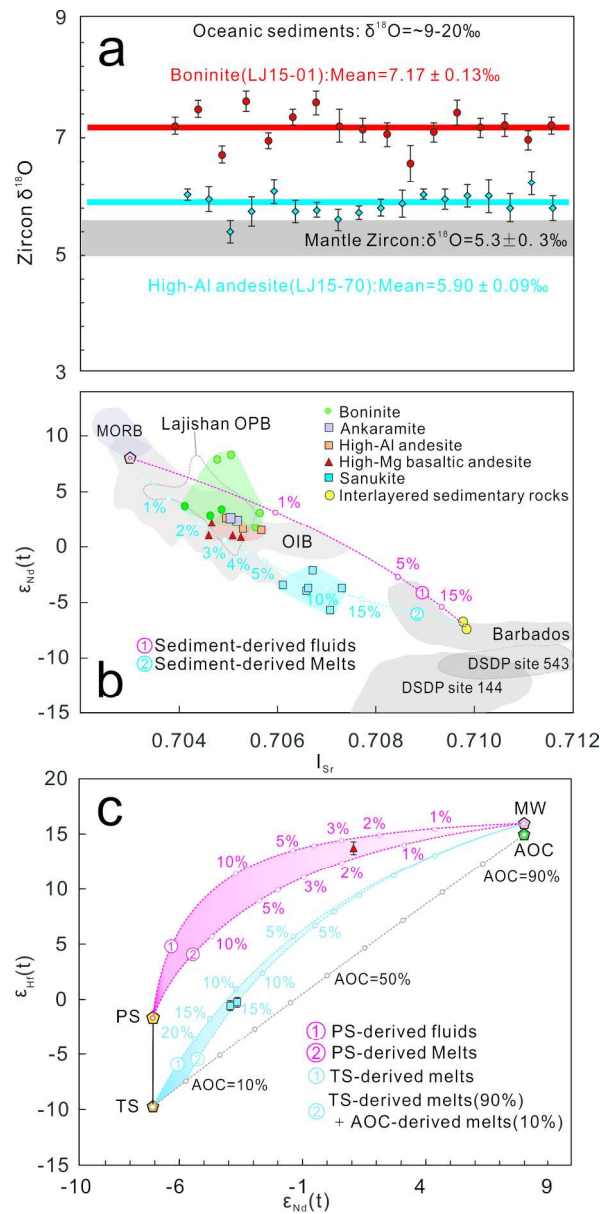


Fig. 11. (a) Zircon O isotopic compositions for island-arc volcanic rocks from the Lajishan-Yongjing Terrane. Data source: the mantle  $\delta^{18}\text{O}$  value ( $5.3 \pm 0.3\text{‰}$ , Valley, 2003); Pelagic sediments and Terrigenous sediments ( $\delta^{18}\text{O} = 9\text{--}20\text{‰}$ , Bindeman et al., 2005; Chauvel et al., 2008; Vervoort et al., 2011). (b) Sr-Nd isotopic compositions for the Lajishan-Yongjing volcanic rocks in the two-component mixing models. Data sources: field labelled MORB and sediments from Barbados, DSDP sites 144 and 543 are from Bezard et al. (2015) and reference therein. The OIB data are from White, (2010). The Lajishan OPB data without the altered samples are from Zhang et al. (2017). (c) Nd-Hf isotopic compositions for the Lajishan-Yongjing volcanic rocks in the mixing model between the mantle wedge (MW), subducted altered oceanic crust (AOC) and oceanic sediments assuming slab dehydration and melting. The dashed mixing trajectories are between mantle wedge and these different fluxing agents. The pink area is restricted by the mixing trajectories of zircon-barren pelagic sediment-derived fluids and melts. The blue area is restricted by the mixing trajectories of terrigenous sediment-derived melts and 90% terrigenous sediment-derived melts + 10% AOC-derived melts. Numbers along the pink and blue mixing trajectories are the amount of the crust-

derived input and numbers along the gray lines are the proportion of AOC component. The end-member compositions are from Hanyu et al. (2006) and listed in Appendix Table 6. The  $\text{ISr}$  and  $\epsilon\text{Nd}(t)$  values of sediments are from the measured interlayered sedimentary rocks from the Lajishan-Yongjing volcanic rocks, and the  $\epsilon\text{Hf}(t)$  values for the pelagic clay sediments (PS:  $\epsilon\text{Hf}(t)=0.99\times\epsilon\text{Nd}(t)+5.34$ ) and terrigenous sediments (TS:  $\epsilon\text{Hf}(t)=1.55\times\epsilon\text{Nd}(t)+1.21$ ) are calculated using the sediments arrays recommended by Vervoort et al. (2011) and Wang et al. (2014), respectively. Symbols are bigger than the maximum analytical error isotope on isotope data, except where shown.

195x400mm (300 x 300 DPI)

For Peer Review

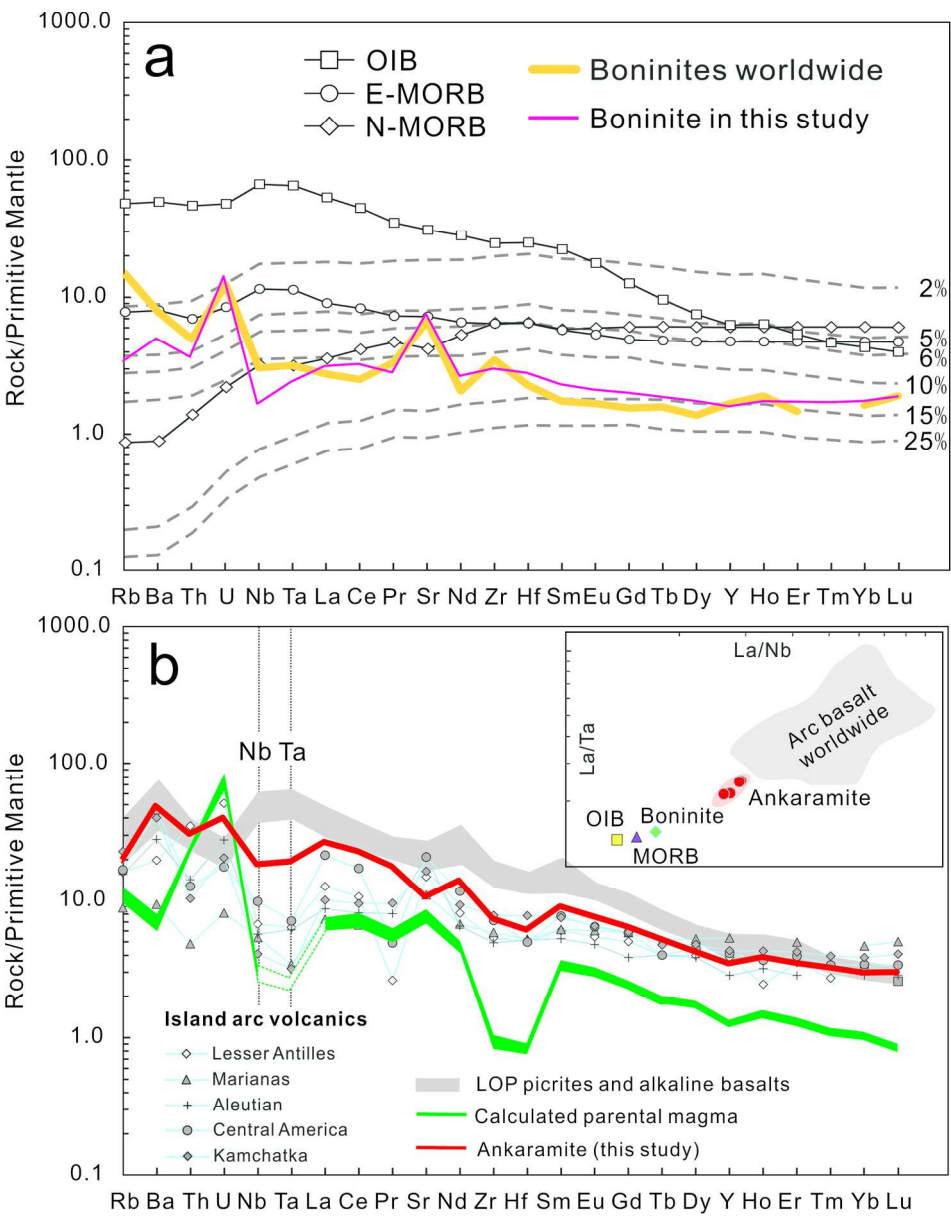


Fig. 12. Primitive mantle (PM)-normalized trace element patterns for the average compositions of (a) boninite, (b) primitive ankaramite and the calculated parental magmas of Cpx-phyric basaltic andesite in Lajishan-Yongjing Terrane. The average compositions of boninite are from near-primitive samples (15LJ-13, 16LJ-07, 09 and 15) with high Mg# of 74-80; the average compositions of ankaramite are from samples of 13QLS-68-72 (Mg#=77-79). (a) Grey dashed lines represent the liquids produced by aggregated fractional melting of the depleted DMM source and the numbers represent melting degree of mantle (Workman & Hart, 2005). Data for comparison are: the OIB, E-MORB, N-MORB (Sun & McDonough., 1989) and the average composition of boninite worldwide (Kelemen et al., 2003). (b) The calculated parental magmas are based on the trace element data of high Mg# Cpx phenocryst from Cpx-phyric basaltic andesite sample (13QLS-124); the amounts of Cpx phenocryst are assumed to range from 0 to 40 wt. %, and Clinopyroxene/melt partition coefficients (KD) and their references are listed in Appendix Table 3. Data for comparison are the island arc volcanics (Kelemen et al., 2003), and the LYO (Lajishan-Yongjing Ophiolite) picrites and alkaline basalts (Zhang et al., 2017).

172x218mm (300 x 300 DPI)

For Peer Review

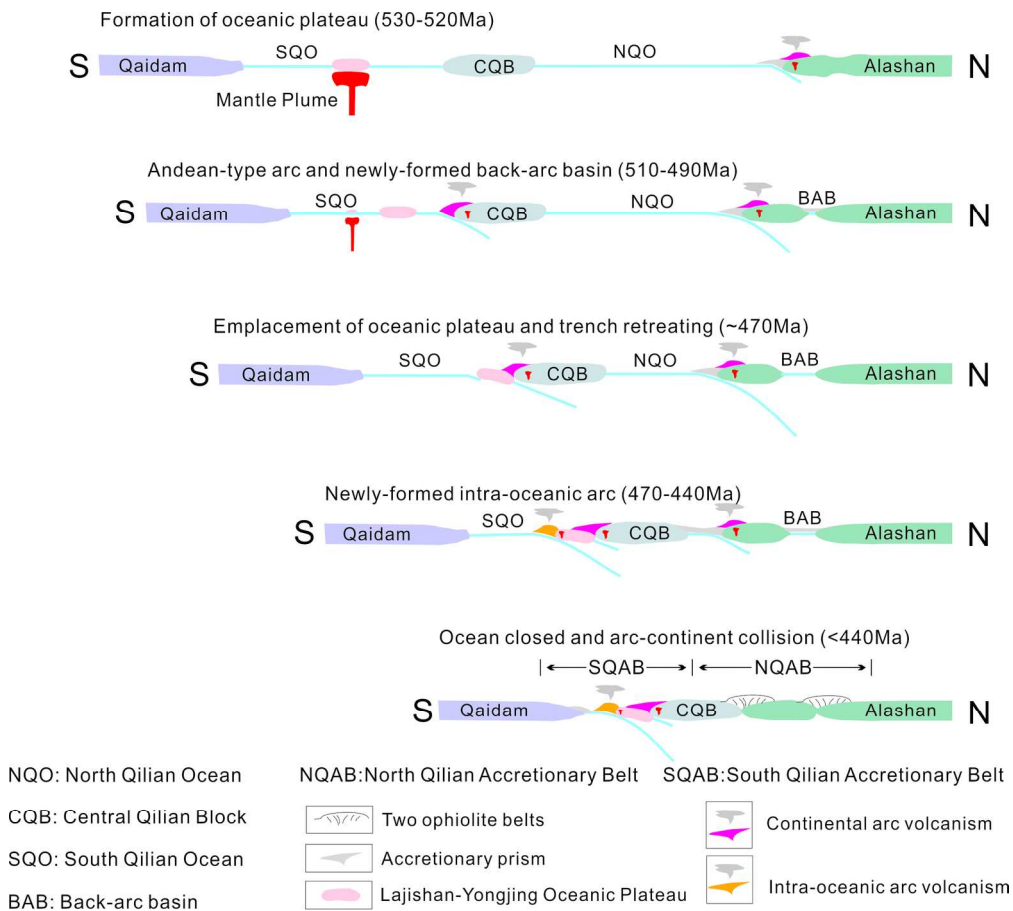


Fig. 13. Schematic cartoons illustrating the tectonic evolution of the South Qilian Accretionary Belt in the Qilian Orogen.

172x154mm (300 x 300 DPI)

Table 1. Major and trace element data for Lajishan-Yongjing arc volcanics

Sample	16LJ-10	16LJ-16	16LJ-18	16LJ-26	12LJ-07	12LJ-09	LJ15-09	LJ15-12	LJ15-13	LJ15-14	LJ15-15	LJ15-108	16LJ-07	16LJ-08
Rocktype	Boninite	Boninite	Boninite	Boninite	Boninite	Boninite	Boninite	Boninite	Boninite	Boninite	Boninite	Boninite	Boninite	Boninite
Location	XX	XX	XX	XX	ZB	ZB	LK	LK	LK	LK	LK	YCT	XX	XX
Major element (wt.%)														
SiO <sub>2</sub>	51.56	50.96	50.59	52.33	51.94	49.71	51.52	50.94	57.37	54.80	54.15	55.84	56.11	52.03
TiO <sub>2</sub>	0.09	0.12	0.11	0.08	0.32	0.35	0.36	0.32	0.21	0.69	0.40	0.27	0.25	0.10
Al <sub>2</sub> O <sub>3</sub>	5.89	7.10	6.22	5.67	11.93	12.49	11.73	13.07	11.68	15.18	10.36	12.23	10.45	6.85
Fe <sub>2</sub> O <sub>3t</sub>	9.87	10.40	10.51	10.08	8.75	9.84	8.00	11.51	7.91	9.23	10.04	9.93	9.56	10.93
MnO	0.18	0.19	0.20	0.19	0.14	0.16	0.15	0.18	0.15	0.15	0.17	0.15	0.15	0.15
MgO	16.84	17.12	17.74	17.48	12.67	13.37	12.79	12.50	9.57	7.81	5.91	10.70	11.93	19.31
CaO	11.91	10.25	11.46	10.67	7.15	7.48	8.75	4.92	5.12	4.85	7.83	3.78	5.32	5.17
Na <sub>2</sub> O	1.19	1.32	0.93	1.35	2.31	1.32	2.04	2.83	4.06	4.62	3.67	3.62	3.19	0.56
K <sub>2</sub> O	0.23	0.14	0.29	0.25	0.90	1.16	2.39	0.70	0.19	0.04	0.12	0.31	0.11	0.04
P <sub>2</sub> O <sub>5</sub>	0.02	0.02	0.02	0.03	0.03	0.04	0.03	0.06	0.03	0.06	0.14	0.04	0.03	0.03
LOI	1.30	1.52	1.64	1.44	3.12	3.44	2.56	3.13	3.30	2.49	6.85	2.81	1.79	3.73
Total	99.1	99.1	99.7	99.6	99.3	99.4	100.3	100.2	99.6	99.9	99.6	99.7	98.9	98.9
Mg#	79.9	79.3	79.7	80.2	77.1	76.0	78.8	71.7	73.8	66.3	57.8	71.5	74.4	80.5
Trace element (ppm)														
Sc	25.9	31.8	24.7	22.6	43.3	49.1	35.5	47.6	41.9	50.5	39.0	40.3	30.8	26.7
Ti	586.2	953.2	673.2	502.6	2140	2348	2268	2136	1417	4930	2662	1883	1701	691.8
V	116.2	141.0	95.5	92.3	221.0	239.6	202.8	316.8	174.3	316.8	165.7	239.2	172.8	133.3
Cr	2150.0	2270.0	2282.0	1839.0	721.6	934.8	903.8	608.2	556.8	259.8	1702.6	823.2	653.0	1806.0
Co	59.1	70.0	64.0	67.3	40.2	46.6	49.2	54.5	43.8	46.7	78.3	53.7	46.1	71.4
Ni	420.6	408.0	423.6	333.0	193.9	234.4	265.2	152.3	114.2	87.8	445.6	210.2	140.4	453.6
Cu	5.5	12.6	2.0	33.5	135.8	144.7	82.0	56.6	86.6	116.3	1.7	70.2	119.8	19.8
Zn	61.2	65.3	63.2	59.5	52.3	63.6	88.0	93.5	65.5	76.1	65.6	80.5	50.1	68.5
Ga	6.3	8.5	6.8	5.5	8.8	10.5	9.8	14.7	10.5	14.0	7.2	12.9	11.0	8.3
Rb	3.1	2.4	5.1	3.3	41.3	55.5	95.4	17.6	3.1	0.4	3.4	4.0	2.0	0.3
Sr	120.1	122.8	48.8	115.1	85.9	122.0	152.5	171.4	140.4	261.2	211.0	152.0	169.2	25.2
Y	3.5	4.5	3.2	2.7	9.6	9.6	10.4	10.6	6.4	22.2	25.8	8.4	7.8	4.1
Zr	18.1	25.8	17.8	16.4	18.0	22.6	24.4	50.5	28.7	52.4	26.8	36.0	38.0	30.0
Nb	0.6	0.8	0.6	0.5	1.3	1.5	2.0	1.2	1.0	0.6	0.4	0.8	1.4	1.1
Cs	0.1	0.2	0.2	0.1	1.7	2.3	1.6	0.8	0.4	0.1	0.3	0.3	0.1	0.3
Ba	43.6	27.8	67.0	65.2	59.6	54.9	390.0	174.8	54.5	36.2	19.7	59.5	27.9	8.6
La	1.3	1.5	1.0	1.0	2.1	2.9	1.0	3.5	2.2	1.8	2.0	2.6	2.2	1.6
Ce	3.4	4.1	2.9	2.5	4.8	6.3	3.0	10.0	5.4	6.3	3.3	6.7	5.7	4.8
Pr	0.5	0.6	0.4	0.3	0.6	0.8	0.5	1.5	0.7	1.2	0.9	0.9	0.8	0.7
Nd	2.1	2.6	1.7	1.6	2.9	3.6	2.6	6.8	3.2	6.4	4.9	4.3	3.6	3.1
Sm	0.5	0.7	0.5	0.4	0.9	1.0	1.0	1.9	0.9	2.4	1.7	1.3	1.0	0.8
Eu	0.2	0.2	0.2	0.2	0.3	0.4	0.4	0.7	0.3	0.9	0.7	0.4	0.4	0.2
Gd	0.6	0.8	0.5	0.5	1.2	1.3	1.5	2.2	1.2	3.5	2.7	1.6	1.2	0.8
Tb	0.1	0.1	0.1	0.1	0.2	0.2	0.3	0.4	0.2	0.7	0.5	0.3	0.2	0.1
Dy	0.5	0.8	0.5	0.4	1.6	1.6	2.1	2.2	1.3	4.5	3.8	1.7	1.3	0.7
Ho	0.1	0.2	0.1	0.1	0.4	0.4	0.5	0.5	0.3	1.1	1.0	0.4	0.3	0.2
Er	0.4	0.5	0.3	0.3	1.1	1.1	1.4	1.4	0.9	3.0	3.0	1.1	0.8	0.4
Tm	0.1	0.1	0.0	0.0	0.2	0.2	0.2	0.2	0.1	0.5	0.4	0.2	0.1	0.1
Yb	0.4	0.5	0.3	0.3	1.2	1.2	1.4	1.4	0.9	3.0	2.9	1.2	0.9	0.4
Lu	0.1	0.1	0.1	0.0	0.2	0.2	0.2	0.2	0.1	0.5	0.5	0.2	0.1	0.1
Hf	0.4	0.6	0.4	0.4	0.4	0.6	0.8	1.5	0.9	1.6	0.8	1.1	0.9	0.7
Ta	0.0	0.1	0.1	0.0	0.1	0.1	0.2	0.1	0.1	0.0	0.0	0.1	0.1	0.1
Pb	0.8	0.8	0.7	0.6	1.2	1.8	2.1	2.5	5.7	2.8	4.8	3.4	1.8	0.3
Th	0.2	0.3	0.2	0.1	0.3	0.3	0.4	0.1	0.1	0.4	0.4	0.1	0.4	0.3
U	0.3	0.2	0.2	0.2	0.1	0.1	0.3	0.5	0.3	0.1	0.1	0.3	0.3	0.3

Ank = ankaramite, HMBA = high-Mg basaltic andesite, HAA = high-Al andesite; LK-Lajishankou, XX-Xiongxiang, CP-Chapu, ZB-Zhaba, SHN-Sihaning, MC-Machang, YCT-Yaocaotai and YJ-Yongjing.

Table 2. Continued

Sampleno.	16LJ-09	16LJ-15	16LJ-47	16LJ-48	16LJ-56	16LJ-57	16LJ-58	16LJ-59	16LJ-61	16LJ-62	16LJ-63	LJ15-106
Rocktype	Boninite	Boninite	Boninite	Boninite	Boninite	Boninite	Boninite	Boninite	Boninite	Boninite	Boninite	Boninite
Location	XX	XX	ZB	ZB	ZB	ZB	ZB	ZB	ZB	ZB	ZB	YCT
Major element (wt.%)												
SiO <sub>2</sub>	58.93	53.99	51.38	54.39	56.20	56.59	57.96	58.82	57.20	54.03	53.21	57.73
TiO <sub>2</sub>	0.21	0.16	0.28	0.52	0.13	0.14	0.14	0.13	0.27	0.29	0.31	0.40
Al <sub>2</sub> O <sub>3</sub>	8.21	7.59	11.31	13.69	8.43	8.28	8.24	7.92	9.88	11.65	11.37	14.02
Fe <sub>2</sub> O <sub>3t</sub>	9.66	9.93	10.23	10.32	10.65	11.09	10.97	10.83	8.76	9.04	9.09	8.84
MnO	0.14	0.14	0.15	0.17	0.17	0.18	0.17	0.17	0.11	0.10	0.11	0.12
MgO	11.68	16.59	10.75	8.65	8.16	9.29	9.46	9.41	11.32	11.03	12.38	5.80
CaO	5.76	5.84	6.08	5.29	6.99	6.40	5.58	5.43	6.79	8.21	8.14	4.19
Na <sub>2</sub> O	2.32	2.25	1.50	4.63	1.23	1.26	1.25	1.19	2.45	2.87	2.57	3.17
K <sub>2</sub> O	0.09	0.12	0.35	0.23	0.03	0.04	0.03	0.04	0.34	0.51	0.50	0.09
P <sub>2</sub> O <sub>5</sub>	0.04	0.04	0.02	0.06	0.02	0.02	0.03	0.02	0.04	0.04	0.04	0.05
LOI	1.56	2.22	7.68	1.76	7.30	5.99	5.40	5.21	2.32	1.98	2.06	5.15
Total	98.6	98.9	99.7	99.7	99.3	99.3	99.2	99.2	99.5	99.8	99.8	99.5
Mg#	73.8	79.6	71.0	66.1	64.1	66.1	66.8	66.9	75.1	74.0	76.0	60.4
Trace element (ppm)												
Sc	28.6	36.4	47.0	42.5	27.6	27.6	30.0	29.0	41.3	35.0	37.7	46.8
Ti	1555	1349	1955	3358	836.2	924.4	916.2	893.2	2150	1848	2074	2866
V	185.6	149.6	255.8	261.6	129.9	139.5	143.3	142.0	243.8	231.0	228.4	321.4
Cr	699.2	2486.0	691.0	757.4	966.6	960.8	876.0	1012.8	887.6	640.0	763.6	159.5
Co	41.3	71.4	40.7	52.5	42.7	45.4	45.7	47.7	40.3	33.5	34.1	36.7
Ni	140.4	449.8	125.7	196.4	109.4	109.8	99.1	115.2	189.3	140.6	179.2	56.9
Cu	126.0	1.7	46.8	43.9	1.8	1.5	8.5	6.4	22.7	9.8	8.8	32.3
Zn	83.4	72.1	64.1	65.1	73.2	78.9	74.9	85.0	33.5	27.2	32.1	71.4
Ga	9.5	10.1	10.2	12.7	10.5	10.5	9.8	10.1	9.2	8.9	8.7	14.3
Rb	1.8	1.6	6.5	3.2	0.6	0.7	0.8	0.8	20.5	19.4	26.2	1.3
Sr	131.4	186.5	78.3	77.4	45.0	36.3	30.6	30.9	123.3	112.8	129.9	123.3
Y	7.9	6.4	7.7	13.2	9.6	9.2	5.4	6.6	11.1	9.4	10.3	12.1
Zr	32.4	33.3	11.7	39.4	28.5	31.5	31.4	29.2	16.8	14.1	16.3	39.7
Nb	1.2	1.1	0.4	0.5	0.9	1.0	1.1	1.0	1.3	1.1	1.3	0.7
Cs	0.1	0.4	0.5	0.0	0.3	0.2	0.2	0.2	0.8	0.5	1.0	0.0
Ba	21.9	33.5	37.7	44.3	4.8	5.1	6.7	6.5	41.7	49.4	39.6	28.4
La	1.9	2.3	1.1	2.5	1.4	1.2	1.2	1.2	1.9	1.6	1.7	3.5
Ce	5.6	6.1	2.7	7.2	4.0	3.8	3.7	3.6	4.8	4.0	4.4	9.5
Pr	0.8	0.8	0.4	1.1	0.6	0.6	0.6	0.6	0.7	0.6	0.6	1.4
Nd	3.6	3.8	1.7	5.7	3.1	3.0	2.6	2.8	3.1	2.6	2.9	6.6
Sm	1.0	1.0	0.6	1.8	1.0	1.0	0.7	0.8	0.9	0.8	0.8	2.0
Eu	0.3	0.3	0.1	0.6	0.3	0.3	0.2	0.2	0.3	0.3	0.3	0.7
Gd	1.2	1.1	0.9	2.1	1.3	1.3	0.8	1.0	1.2	1.1	1.2	2.3
Tb	0.2	0.2	0.2	0.4	0.2	0.2	0.1	0.2	0.2	0.2	0.2	0.4
Dy	1.3	1.2	1.3	2.3	1.3	1.4	0.9	1.0	1.7	1.4	1.5	2.6
Ho	0.3	0.3	0.3	0.5	0.3	0.3	0.2	0.2	0.4	0.3	0.4	0.6
Er	0.8	0.7	0.9	1.5	0.8	0.9	0.5	0.6	1.2	1.0	1.1	1.7
Tm	0.1	0.1	0.1	0.2	0.1	0.1	0.1	0.1	0.2	0.2	0.2	0.3
Yb	0.9	0.7	1.0	1.4	0.8	0.9	0.5	0.6	1.3	1.1	1.2	1.7
Lu	0.1	0.1	0.2	0.2	0.1	0.1	0.1	0.1	0.2	0.2	0.2	0.3
Hf	0.8	0.8	0.4	1.0	0.7	0.8	0.7	0.7	0.4	0.4	0.4	1.3
Ta	0.1	0.1	0.0	0.0	0.1	0.1	0.1	0.1	0.1	0.1	0.1	0.1
Pb	1.8	1.6	4.2	2.9	0.5	0.4	0.6	0.6	1.0	0.7	0.9	2.2
Th	0.4	0.4	0.3	0.4	0.7	0.7	0.7	0.6	0.3	0.3	0.3	0.2
U	0.3	0.3	0.1	0.2	0.2	0.2	0.2	0.2	0.0	0.0	0.1	0.2

Ank = ankaramite, HMBA = high-Mg basaltic andesite, HAA = high-Al andesite; LK-Lajishankou, XX-Xiongxian, CP-Chapu, ZB-Zhaba, SHN-Sihaning, MC-Machang, YCT-Yaocaotai and YJ-Yongjing.

Table 2. Continued

Sample	13QLS-68	13QLS-7	13QLS-7	13QLS-7	13QLS-12	13QLS-12	13QLS-13	LJ15-2	LJ15-3	LJ15-3	LJ15-4	LJ15-42
Rock type	Ank	Ank	Ank	Ank	HMBA	HMBA	HMBA	HMBA	HMBA	HMBA	HMBA	HMB
Location	XX	XX	XX	XX	YJ	YJ	YJ	ZB	ZB	ZB	ZB	ZB
Major element (wt. %)												
SiO <sub>2</sub>	48.75	48.63	48.00	49.18	53.81	52.45	51.75	55.60	54.63	49.91	55.62	55.28
TiO <sub>2</sub>	0.74	0.74	0.77	0.76	0.94	0.99	1.01	0.95	0.78	1.21	0.81	0.81
Al <sub>2</sub> O <sub>3</sub>	11.48	10.36	10.70	10.96	13.71	13.99	13.11	15.91	14.56	17.46	14.68	15.26
Fe <sub>2</sub> O <sub>3t</sub>	10.19	9.35	10.13	10.27	8.93	9.20	9.21	6.82	5.62	7.44	5.82	6.21
MnO	0.18	0.20	0.19	0.18	0.22	0.36	0.19	0.13	0.11	0.11	0.10	0.11
MgO	15.05	15.34	15.62	14.95	8.05	8.56	7.37	7.27	6.66	7.25	7.36	8.31
CaO	8.99	9.99	9.63	9.21	6.37	7.62	8.44	4.73	6.70	8.19	5.75	5.42
Na <sub>2</sub> O	1.94	2.06	2.19	1.82	2.74	2.04	2.43	2.47	5.00	3.82	3.69	2.94
K <sub>2</sub> O	0.82	0.86	0.39	0.72	1.34	0.95	2.81	2.36	0.46	1.19	2.18	2.12
P <sub>2</sub> O <sub>5</sub>	0.39	0.40	0.43	0.40	0.32	0.30	0.27	0.20	0.19	0.40	0.20	0.20
LOI	1.69	2.51	2.46	2.25	2.84	2.57	2.41	3.51	5.20	3.55	3.66	3.33
Total	100.2	100.4	100.5	100.6	99.3	99.0	99.0	99.9	99.9	100.5	99.9	100.0
Mg#	77.02	77.02	78.23	77.23	67.8	68.5	65.1	71.3	73.4	69.4	74.7	75.7
Trace element (ppm)												
Sc	37.4	37.5	41.7	38.9	40.4	49.8	43.9	28.4	26.7	24.1	26.5	27.2
Ti	4466	4632	4998	4780	5635	5932	6080.1	7000	5626	7644	5870	5562
V	206.8	203.0	223.4	211.4	245.2	341.2	299.4	190.7	158.8	154.9	170.2	166.0
Cr	1294.8	1126.2	1341.0	1270.2	419.4	501.4	481.6	253.2	442.8	339.8	435.0	449.8
Co	52.5	50.0	55.6	56.3	61.6	46.3	42.1	38.9	35.9	37.9	38.1	38.7
Ni	340.4	312.0	377.4	352.0	77.9	72.8	114.2	106.9	195.7	186.6	198.5	195.8
Cu	53.5	56.8	79.0	66.8	35.5	186.8	59.0	46.0	67.1	67.3	56.3	40.3
Zn	65.3	61.0	66.5	67.6	129.8	87.1	76.1	181.6	110.9	60.2	60.0	60.8
Ga	13.2	12.1	14.1	14.1	15.8	18.0	17.2	18.5	17.8	20.5	17.0	16.4
Rb	15.2	12.3	7.6	14.1	49.8	26.4	47.8	121.5	8.8	15.9	33.5	46.2
Sr	225.8	221.4	150.8	289.0	270.2	307.0	350.8	386.4	253.6	867.2	370.8	399.0
Y	14.7	15.4	16.4	15.9	20.5	21.1	22.3	22.1	16.3	21.3	17.8	16.5
Zr	76.6	81.8	86.6	81.8	90.3	87.2	94.1	148.3	116.1	181.6	121.2	116.1
Nb	12.4	13.0	13.5	12.8	11.9	12.4	12.0	12.4	14.5	30.9	15.3	14.4
Cs	1.5	1.2	1.0	1.7	2.3	1.5	0.4	3.1	0.7	1.8	1.2	1.6
Ba	351.0	464.6	198.7	326.8	431.8	289.4	643.2	1219.6	123.8	452.6	842.8	636.4
La	17.0	18.9	17.7	18.5	17.0	15.8	14.6	28.5	27.0	41.6	28.5	27.3
Ce	37.5	41.4	40.4	41.0	34.7	34.5	30.2	58.5	51.0	81.6	54.7	52.0
Pr	4.5	5.0	5.0	5.0	4.1	4.1	3.7	7.2	5.8	9.8	6.2	5.9
Nd	17.4	18.9	19.6	19.1	16.8	16.7	15.3	26.4	21.0	35.9	22.2	21.4
Sm	3.7	4.0	4.2	4.0	3.9	3.8	3.7	5.3	4.1	6.5	4.4	4.2
Eu	1.2	1.2	1.3	1.3	1.2	1.2	1.2	1.6	1.4	2.1	1.6	1.4
Gd	3.5	3.7	4.0	3.8	4.0	3.7	3.8	5.0	3.9	5.7	4.2	4.0
Tb	0.5	0.5	0.6	0.6	0.6	0.6	0.6	0.8	0.6	0.8	0.6	0.6
Dy	2.9	3.0	3.3	3.2	3.8	3.5	3.6	4.4	3.4	4.4	3.6	3.4
Ho	0.6	0.6	0.7	0.6	0.8	0.7	0.7	0.9	0.7	0.9	0.8	0.7
Er	1.6	1.6	1.7	1.7	2.2	2.1	2.1	2.5	2.0	2.5	2.1	2.0
Tm	0.2	0.2	0.2	0.2	0.3	0.3	0.3	0.4	0.3	0.4	0.3	0.3
Yb	1.4	1.4	1.5	1.5	2.0	1.8	1.9	2.2	1.8	2.3	1.9	1.8
Lu	0.2	0.2	0.2	0.2	0.3	0.3	0.3	0.3	0.3	0.4	0.3	0.3
Hf	1.7	1.9	2.0	1.9	2.4	2.2	2.4	3.5	2.7	3.7	2.9	2.8
Ta	0.8	0.8	0.8	0.8	0.7	0.7	0.7	0.8	1.1	1.7	1.0	0.9
Pb	2.8	3.9	4.6	4.2	3.6	6.5	8.5	9.2	14.9	21.0	19.3	14.5
Th	2.4	2.6	2.7	2.6	4.6	4.3	3.1	8.1	6.6	8.0	7.1	6.6
U	0.8	0.8	0.9	0.8	0.7	0.8	0.7	2.3	2.3	2.4	2.4	2.2

Ank = ankaramite, HMBA = high-Mg basaltic andesite, HAA = high-Al andesite; LK-Lajishankou, XX-Xiongshan, CP-Chapu, ZB-Zhaba, SHN-Sihaning, MC-Machang, YCT-Yaocaotai and YJ-Yongjing.



1  
2  
3  
4  
5  
6  
7  
8  
9  
10  
11  
12  
13  
14  
15  
16  
17  
18  
19  
20  
21  
22  
23  
24  
25  
26  
27  
28  
29  
30  
31  
32  
33  
34  
35  
36  
37  
38  
39  
40  
41  
42  
43  
44  
45  
46  
47  
48  
49  
50  
51  
52  
53  
54  
55  
56  
57  
58  
59  
60

Table 2. Continued

Sample	LJ15-166	LJ15-167	16LJ-27	16LJ-32	13QLS16	13QLS17	13QLS58	13QLS61	13QLS86	13QLS89	13QLS92	13QLS95	13QLS100
Rock type	HMBA	HMBA	HMBA	HMBA	HAA	HAA	HAA	HAA	HAA	HAA	HAA	HAA	HAA
Location	YJ	YJ	XX	CP	MC	MC	XX	XX	CP	CP	CP	CP	YJ
Major element (wt.%)													
SiO <sub>2</sub>	51.24	53.11	54.63	49.61	49.10	54.52	51.49	55.56	60.19	60.55	52.81	48.65	54.76
TiO <sub>2</sub>	1.03	0.93	0.62	0.60	0.76	0.78	0.92	0.83	0.82	0.53	0.84	0.74	0.57
Al <sub>2</sub> O <sub>3</sub>	15.94	12.91	14.26	11.74	18.72	17.90	19.17	16.38	18.00	18.70	18.78	23.06	20.82
Fe <sub>2</sub> O <sub>3t</sub>	9.55	9.57	7.69	10.51	9.71	9.15	8.46	8.57	6.92	4.98	8.28	8.73	7.11
MnO	0.33	0.19	0.14	0.17	0.16	0.11	0.14	0.14	0.11	0.09	0.09	0.17	0.13
MgO	8.40	8.80	7.53	9.86	5.48	3.63	4.63	2.86	2.19	1.14	1.63	3.92	2.97
CaO	7.35	10.47	7.73	12.52	6.52	3.94	8.79	6.12	2.26	2.83	9.79	4.36	6.75
Na <sub>2</sub> O	3.04	1.62	4.16	1.27	5.07	6.59	3.41	5.44	6.84	4.78	5.99	7.40	3.85
K <sub>2</sub> O	0.70	0.61	0.77	0.93	0.86	0.37	0.86	1.48	0.11	1.69	0.01	0.28	0.99
P <sub>2</sub> O <sub>5</sub>	0.33	0.28	0.13	0.14	0.20	0.21	0.17	0.19	0.36	0.17	0.26	0.15	0.23
LOI	2.45	1.76	1.63	2.19	2.91	2.22	0.96	2.01	1.61	3.36	1.79	2.59	1.92
Total	100.4	100.3	99.3	99.5	99.5	99.4	99.0	99.6	99.4	98.8	100.3	100.1	100.1
Mg#	67.2	68.2	69.5	68.6	56.8	48.1	56.0	43.8	42.4	34.7	31.5	51.2	49.3
Trace element (ppm)													
Sc	44.7	44.8	26.8	52.0	35.1	32.8	39.4	17.4	15.1	11.3	21.4	25.2	16.5
Ti	6839	6414	3664	3486	4884	5102	5494	5279	5360	3570	5624	4902	3802
V	266.5	291.4	197.9	295.6	266.2	259.6	312.6	202.3	100.2	11.1	154.0	248.0	134.6
Cr	449.9	503.4	310.2	434.8	108.3	99.9	63.9	26.5	5.1	4.4	25.0	19.9	58.5
Co	50.5	41.5	32.6	48.3	25.6	24.5	31.5	20.6	10.9	4.9	21.4	27.5	17.4
Ni	76.5	72.1	87.6	87.1	38.4	35.5	22.5	14.9	3.6	2.8	18.7	12.9	24.6
Cu	27.9	145.5	6.7	66.5	72.3	74.8	46.3	9.4	10.7	19.2	14.4	14.1	28.0
Zn	90.8	82.4	64.4	57.7	77.0	76.6	74.3	63.8	63.1	46.2	51.2	76.7	66.3
Ga	17.7	17.3	14.8	11.8	17.9	18.0	19.4	14.8	13.3	17.5	17.7	17.3	18.5
Rb	20.5	17.7	15.3	14.9	8.7	5.0	22.7	28.8	1.5	39.0	0.4	4.3	23.4
Sr	430.8	651.4	458.6	472.6	396.2	398.6	406.2	402.1	145.0	135.3	99.5	390.6	1154.2
Y	21.2	20.1	13.3	14.0	13.8	14.3	21.2	18.7	29.2	42.4	19.0	21.8	15.2
Zr	97.7	90.1	51.5	47.0	91.9	99.5	61.8	78.2	175.7	264.4	82.2	92.3	69.9
Nb	13.7	12.2	4.2	4.3	13.2	14.4	5.6	5.6	24.2	46.2	11.6	6.4	10.6
Cs	1.8	0.6	2.1	1.8	0.7	0.4	2.4	2.7	0.1	1.2	0.0	0.2	1.6
Ba	296.8	269.0	259.0	342.2	326.8	138.2	254.8	288.0	51.1	235.6	26.2	234.6	360.2
La	18.2	18.1	9.3	9.8	13.7	13.0	7.9	7.0	21.8	33.6	10.8	13.0	19.4
Ce	35.8	35.0	20.0	21.4	28.8	27.4	17.9	17.3	47.5	68.5	23.6	27.3	40.2
Pr	4.4	4.2	2.6	2.7	3.3	3.3	2.4	2.2	5.7	8.0	3.0	3.3	4.7
Nd	17.6	16.8	10.4	11.1	12.6	12.3	10.5	9.7	21.9	29.7	12.0	13.3	17.5
Sm	4.1	3.9	2.4	2.8	2.8	2.7	2.8	2.7	5.1	6.7	3.0	3.3	3.6
Eu	1.3	1.3	0.8	0.8	1.0	0.9	1.0	1.0	1.3	1.4	1.0	1.0	1.2
Gd	4.6	4.4	2.4	2.9	2.8	2.7	3.1	3.1	5.4	6.9	3.3	3.6	3.3
Tb	0.8	0.7	0.4	0.4	0.4	0.4	0.5	0.5	0.9	1.2	0.5	0.6	0.5
Dy	4.6	4.4	2.2	2.5	2.5	2.5	3.2	3.3	5.2	7.3	3.3	3.8	2.9
Ho	1.0	1.0	0.5	0.5	0.5	0.5	0.7	0.7	1.1	1.6	0.7	0.8	0.6
Er	2.7	2.6	1.3	1.4	1.5	1.6	1.9	2.1	3.2	4.7	2.0	2.4	1.7
Tm	0.4	0.4	0.2	0.2	0.2	0.2	0.3	0.3	0.5	0.7	0.3	0.4	0.2
Yb	2.5	2.5	1.2	1.2	1.4	1.5	1.8	1.9	3.1	4.9	1.9	2.4	1.6
Lu	0.4	0.4	0.2	0.2	0.2	0.2	0.3	0.3	0.5	0.8	0.3	0.4	0.2
Hf	2.9	2.7	1.2	1.1	2.3	2.5	1.7	1.8	3.9	6.1	2.0	2.4	1.7
Ta	1.1	0.8	0.2	0.2	0.8	0.9	0.3	0.4	1.8	2.8	0.7	0.5	0.7
Pb	7.2	10.5	3.0	3.5	7.1	10.8	1.8	3.9	4.3	6.4	2.3	5.3	13.3
Th	5.3	4.7	1.5	2.6	2.5	2.6	1.2	1.2	5.8	8.7	2.0	3.4	4.0
U	1.6	1.2	0.4	0.6	0.8	0.9	0.3	0.5	1.6	2.1	0.3	1.3	1.1

Ank = ankaramite, HMBA = high-Mg basaltic andesite, HAA = high-Al andesite; LK-Lajishankou, XX-Xiongxiang, CP-Chapu, ZB-Zhaba, SHN-Sihaning, MC-Machang, YCT-Yaocaotai and YJ-Yongjing.

Table 2. Continued.

Sample	13QLS103	13QLS123	LJ15-70	LJ15-109	12LJ-13	12LJ-14	12LJ-15	Lj-3	Lj-4	Lj-5	12LJ-05	LJ15-52	LJ15-53
Rock type	HAA	HAA	HAA	HAA	Sanukite	Sanukite	Sanukite	Sanukite	Sanukite	Sanukite	Sanukite	Sanukite	Sanukite
Location	YJ	YJ	SHN	YCT	ZB	ZB	ZB	ZB	ZB	ZB	ZB	ZB	ZB
Major element (wt.%)													
SiO <sub>2</sub>	51.14	60.44	54.38	58.14	54.51	55.53	60.73	54.93	56.87	55.70	63.61	64.81	65.83
TiO <sub>2</sub>	0.55	0.78	0.79	0.70	0.76	0.77	0.68	0.71	0.73	0.77	0.52	0.44	0.60
Al <sub>2</sub> O <sub>3</sub>	19.36	16.17	17.32	18.94	13.53	13.87	12.51	13.10	14.16	14.47	14.41	13.75	15.40
Fe <sub>2</sub> O <sub>3t</sub>	7.66	7.06	8.16	7.42	6.66	6.49	5.67	7.08	6.75	7.50	3.44	3.58	4.23
MnO	0.15	0.11	0.11	0.15	0.07	0.06	0.05	0.07	0.05	0.06	0.05	0.05	0.08
MgO	4.03	2.39	2.67	3.50	6.20	6.32	4.67	6.96	5.43	7.23	2.58	2.36	2.88
CaO	6.06	4.54	5.61	0.66	5.26	5.50	5.06	5.23	5.95	3.65	2.81	4.05	2.15
Na <sub>2</sub> O	3.12	3.01	2.73	7.68	2.42	2.49	2.19	2.83	2.73	3.11	4.96	3.08	3.73
K <sub>2</sub> O	4.06	1.89	0.91	0.10	1.55	1.64	1.24	1.25	1.28	1.17	1.20	1.04	2.60
P <sub>2</sub> O <sub>5</sub>	0.24	0.16	0.13	0.39	0.25	0.25	0.22	0.21	0.22	0.22	0.19	0.17	0.20
LOI	3.03	2.22	7.15	1.90	7.94	6.23	5.96	6.97	5.20	5.44	5.09	6.38	2.05
Total	99.4	98.8	99.9	99.6	99.2	99.1	99.0	99.3	99.4	99.3	98.9	99.7	99.7
Mg#	55.1	44.1	43.2	52.4	68.4	69.4	65.8	69.6	65.2	69.2	63.5	60.6	61.4
Trace element (ppm)													
Sc	16.2	20.5	29.9	5.6	22.0	21.6	19.7	22.2	21.4	24.0	11.1	9.8	13.4
Ti	3670	4681	5580	4486	5048	4960	4498	5420	5380	5886	3508	3422	4330
V	145.2	198.3	244.6	10.7	164.0	164.4	145.6	194.0	193.3	207.6	92.1	82.1	115.8
Cr	90.0	105.8	12.9	2.0	444.2	421.6	384.4	500.2	460.8	521.8	88.7	68.6	90.4
Co	20.9	23.4	26.0	6.2	21.1	20.0	16.8	29.3	25.3	22.6	7.0	13.7	11.9
Ni	23.4	34.2	9.7	1.4	135.6	125.9	110.5	138.7	127.0	130.1	16.7	19.1	25.5
Cu	37.1	34.7	69.8	25.7	25.9	210.6	300.0	95.5	461.2	318.6	3.3	15.4	12.5
Zn	60.9	76.5	66.3	125.5	48.6	42.4	33.9	61.5	51.2	52.4	30.6	101.7	119.1
Ga	17.1	20.6	18.7	20.1	18.1	19.1	17.0	18.2	19.3	20.9	19.4	18.3	20.1
Rb	74.1	66.2	21.1	1.1	63.5	86.1	61.0	72.7	74.9	70.6	70.9	50.3	63.7
Sr	569.6	649.8	274.0	250.0	283.2	416.0	264.2	279.6	346.4	274.4	241.2	412.2	498.0
Y	18.0	17.5	19.4	36.4	13.9	16.3	15.1	15.9	14.2	13.8	12.8	10.3	15.2
Zr	108.3	145.8	79.2	278.0	138.1	150.6	135.5	130.0	133.8	134.3	143.0	144.6	161.9
Nb	15.4	14.2	4.7	36.2	22.0	21.9	20.2	21.1	21.0	22.1	21.9	20.8	24.9
Cs	0.6	2.0	1.4	0.3	3.5	2.4	3.9	2.3	3.0	2.9	4.1	3.0	2.1
Ba	748.0	599.4	278.2	142.9	613.4	995.6	255.2	391.8	316.6	334.6	226.6	139.6	1088.6
La	18.6	21.6	6.4	39.6	40.7	37.6	31.6	36.3	27.8	26.5	25.5	32.5	37.8
Ce	36.7	44.7	15.2	80.2	73.4	68.3	59.5	67.8	52.0	50.0	46.5	58.7	68.7
Pr	4.2	5.3	2.2	9.8	7.8	7.5	6.7	7.4	5.7	5.5	5.1	6.2	7.4
Nd	15.3	20.2	9.8	37.0	27.5	27.3	25.0	26.9	21.4	20.0	19.1	20.9	25.7
Sm	3.3	4.0	2.7	7.5	4.5	4.8	4.4	4.6	3.9	3.5	3.5	3.4	4.6
Eu	1.0	1.1	0.7	2.2	1.3	1.4	1.2	1.3	1.2	1.0	1.0	1.0	1.5
Gd	3.3	3.5	3.3	7.5	3.6	4.1	3.8	3.9	3.4	3.1	3.1	2.9	4.0
Tb	0.5	0.5	0.6	1.2	0.5	0.5	0.5	0.5	0.5	0.4	0.4	0.4	0.6
Dy	3.2	2.9	4.0	7.4	2.7	3.1	2.8	3.0	2.6	2.5	2.4	2.2	3.3
Ho	0.7	0.6	0.9	1.7	0.5	0.6	0.5	0.6	0.5	0.5	0.5	0.5	0.7
Er	2.0	1.7	2.7	4.9	1.5	1.7	1.5	1.7	1.4	1.5	1.3	1.3	1.8
Tm	0.3	0.2	0.4	0.8	0.2	0.2	0.2	0.2	0.2	0.2	0.2	0.2	0.3
Yb	1.9	1.5	2.7	5.2	1.4	1.6	1.4	1.5	1.3	1.4	1.2	1.4	1.8
Lu	0.3	0.2	0.4	0.8	0.2	0.2	0.2	0.2	0.2	0.2	0.2	0.2	0.3
Hf	2.7	3.5	2.3	7.0	3.6	3.8	3.5	3.0	3.1	3.1	3.8	4.2	4.6
Ta	1.0	0.8	0.3	2.5	1.4	1.4	1.3	1.3	1.3	1.3	1.5	1.6	2.1
Pb	10.5	15.5	4.9	6.2	3.5	3.5	3.6	2.0	2.8	1.4	4.4	12.7	14.1
Th	4.7	6.9	1.1	7.1	10.1	8.9	8.0	6.6	6.9	7.1	8.0	12.0	14.0
U	1.5	1.2	0.5	1.7	1.8	2.1	2.1	1.9	2.0	2.0	2.0	2.8	3.3

Ank = ankaramite, HMBA = high-Mg basaltic andesite, HAA = high-Al andesite; LK-Lajishankou, XX-Xiongxiang, CP-Chapu, ZB-Zhaba, SHN-Sihaning, MC-Machang, YCT-Yaocaotai and YJ-Yongjing.

Table 2. Average electron microprobe analyses of Cpx for Lajishan-Yongjing arc volcanics.

Sample	n	SiO <sub>2</sub>	TiO <sub>2</sub>	Al <sub>2</sub> O <sub>3</sub>	Cr <sub>2</sub> O <sub>3</sub>	FeO <sub>T</sub>	MnO	MgO	CaO	Na <sub>2</sub> O	K <sub>2</sub> O	total	Si	Al(□)	Al(□)	Ti	Cr	Fe <sup>3+</sup>	Fe <sup>2+</sup>	Mn	Mg	Ca	Na	K	sum	Wo	En	Fs	Ac	Mg#
13QLS68-1	3	53.27	0.13	1.75	0.85	3.67	0.14	17.48	22.15	0.22	0.00	99.65	1.95	0.05	0.02	0.00	0.02	0.02	0.10	0.00	0.95	0.87	0.02	0.00	4.01	44.45	48.79	5.97	0.78	0.91
13QLS68-2	10	52.70	0.29	2.17	0.62	4.33	0.13	16.83	22.36	0.22	0.01	99.66	1.93	0.07	0.03	0.01	0.02	0.03	0.11	0.00	0.92	0.88	0.02	0.00	4.01	45.03	47.16	7.00	0.82	0.90
13QLS68-3	4	52.74	0.22	2.18	0.74	3.90	0.12	16.90	21.94	0.25	0.00	98.99	1.94	0.06	0.04	0.01	0.02	0.01	0.11	0.00	0.93	0.87	0.02	0.00	4.00	44.73	47.94	6.40	0.93	0.89
13QLS68-4	3	52.07	0.43	2.93	0.66	4.67	0.15	16.06	22.01	0.29	0.00	99.27	1.92	0.08	0.05	0.01	0.02	0.01	0.13	0.00	0.88	0.87	0.02	0.00	4.00	45.25	45.95	7.73	1.08	0.87
13QLS68-5	7	53.11	0.22	2.24	0.79	4.08	0.12	16.65	22.30	0.21	0.01	99.74	1.94	0.06	0.04	0.01	0.02	0.01	0.12	0.00	0.91	0.87	0.02	0.00	4.00	45.39	47.14	6.68	0.79	0.89
13QLS68-6	6	52.61	0.35	2.63	0.64	4.56	0.14	16.37	22.29	0.24	0.00	99.84	1.93	0.07	0.04	0.01	0.02	0.01	0.13	0.00	0.90	0.88	0.02	0.00	4.00	45.33	46.33	7.45	0.88	0.88
13QLS72-1	5	51.74	0.45	3.45	0.62	4.66	0.11	15.76	22.02	0.25	0.20	99.26	1.91	0.09	0.06	0.01	0.02	0.02	0.13	0.00	0.87	0.87	0.02	0.01	4.01	45.78	45.50	7.78	0.94	0.87
13QLS72-3	3	52.49	0.30	2.37	0.63	4.51	0.16	16.50	22.01	0.21	0.01	99.19	1.94	0.06	0.04	0.01	0.02	0.01	0.13	0.00	0.91	0.87	0.02	0.00	4.00	44.93	46.85	7.43	0.79	0.87
13QLS72-7	2	52.31	0.31	2.79	0.90	4.08	0.16	16.41	22.14	0.27	0.00	99.35	1.92	0.08	0.05	0.01	0.03	0.01	0.12	0.00	0.90	0.87	0.02	0.00	4.00	45.41	46.82	6.79	0.99	0.88
13QLS72-9	5	52.94	0.24	2.04	0.50	4.26	0.13	16.73	22.19	0.20	0.01	99.23	1.95	0.05	0.04	0.01	0.01	0.01	0.12	0.00	0.92	0.87	0.01	0.00	4.00	45.04	47.26	6.95	0.75	0.88
13QLS124-1	10	50.08	0.66	3.29	0.26	8.18	0.23	15.31	19.56	0.27	0.02	97.87	1.90	0.10	0.04	0.02	0.01	0.05	0.21	0.01	0.86	0.79	0.02	0.00	4.02	40.85	44.47	13.66	1.03	0.81
13QLS124-2	6	49.69	0.71	3.44	0.13	9.01	0.27	15.11	18.85	0.30	0.00	97.50	1.89	0.11	0.05	0.02	0.00	0.05	0.23	0.01	0.86	0.77	0.02	0.00	4.02	39.57	44.13	15.15	1.15	0.79
13QLS124-3	6	51.84	0.37	2.01	0.56	5.40	0.17	16.69	21.12	0.22	0.01	98.37	1.93	0.07	0.02	0.01	0.02	0.03	0.14	0.01	0.93	0.84	0.02	0.00	4.01	43.02	47.28	8.91	0.80	0.87
LJ15-42-1	2	53.02	0.38	2.47	0.90	3.85	0.12	17.29	21.91	0.28	0.01	100.21	1.93	0.07	0.04	0.01	0.03	0.01	0.10	0.00	0.94	0.85	0.02	0.00	4.00	44.23	48.53	6.24	1.01	0.90
LJ15-42-2	2	52.39	0.43	3.19	1.06	4.06	0.11	16.93	21.58	0.33	0.00	100.05	1.91	0.09	0.05	0.01	0.03	0.02	0.11	0.00	0.92	0.84	0.02	0.00	4.00	44.06	48.10	6.64	1.22	0.90
LJ15-42-3	2	53.34	0.38	2.26	0.01	5.17	0.24	17.43	21.04	0.18	0.01	100.04	1.95	0.05	0.04	0.01	0.00	0.00	0.15	0.01	0.95	0.82	0.01	0.00	4.00	42.23	48.66	8.46	0.66	0.86
LJ15-42-4	2	53.07	0.26	2.26	0.79	3.77	0.14	17.25	22.00	0.27	0.01	99.80	1.94	0.06	0.04	0.01	0.02	0.01	0.10	0.00	0.94	0.86	0.02	0.00	4.00	44.42	48.46	6.15	0.97	0.90
LJ15-42-5	2	53.12	0.32	2.55	1.00	3.70	0.10	17.23	21.84	0.30	0.01	100.15	1.93	0.07	0.04	0.01	0.03	0.01	0.10	0.00	0.93	0.85	0.02	0.00	4.00	44.29	48.61	6.01	1.10	0.90
LJ15-42-6	2	52.89	0.31	2.49	0.86	3.91	0.13	17.31	21.79	0.31	0.00	99.98	1.93	0.07	0.04	0.01	0.02	0.02	0.10	0.00	0.94	0.85	0.02	0.00	4.01	43.97	48.58	6.35	1.11	0.91
LJ15-42-7	2	52.42	0.41	3.15	1.08	3.70	0.09	16.76	22.17	0.26	0.00	100.02	1.91	0.09	0.05	0.01	0.03	0.01	0.11	0.00	0.91	0.87	0.02	0.00	4.00	45.34	47.67	6.05	0.95	0.90
LJ15-42-8	2	52.98	0.35	2.66	0.85	3.82	0.16	16.91	21.84	0.25	0.00	99.81	1.93	0.07	0.05	0.01	0.02	0.00	0.11	0.00	0.92	0.85	0.02	0.00	4.00	44.65	48.08	6.35	0.93	0.89
LJ15-42-9	3	52.37	0.50	3.12	0.87	4.07	0.12	16.73	22.05	0.27	0.01	100.10	1.91	0.09	0.05	0.01	0.03	0.02	0.11	0.00	0.91	0.86	0.02	0.00	4.00	44.94	47.43	6.66	0.98	0.89
LJ15-42-10	3	52.71	0.31	2.71	1.04	3.92	0.11	17.17	21.64	0.30	0.00	99.92	1.92	0.08	0.04	0.01	0.03	0.01	0.11	0.00	0.93	0.85	0.02	0.00	4.00	43.98	48.54	6.38	1.09	0.90
LJ15-42-11	1	52.84	0.32	3.11	1.24	3.59	0.12	16.67	21.96	0.33	0.00	100.18	1.92	0.08	0.06	0.01	0.04	0.00	0.11	0.00	0.90	0.86	0.02	0.00	4.00	45.14	47.67	5.96	1.23	0.89
LJ15-42-12	2	52.58	0.44	2.90	1.03	4.12	0.19	16.69	21.86	0.29	0.00	100.08	1.92	0.08	0.04	0.01	0.03	0.00	0.12	0.01	0.91	0.85	0.02	0.00	4.00	44.65	47.43	6.87	1.05	0.88
LJ15-42-13	2	53.08	0.29	3.38	0.52	4.68	0.18	16.74	21.01	0.44	0.00	100.30	1.93	0.07	0.07	0.01	0.01	0.00	0.14	0.01	0.91	0.82	0.03	0.00	4.00	42.97	47.65	7.77	1.63	0.87

Table 3. Whole-rock Rb–Sr and Sm–Nd isotope compositions for the Lajishan-Yongjing arc volcanics.

Sample no.	Rock type	T ( Ma)	Rb	Sr	$^{87}\text{Rb}/^{86}\text{Sr}$	$^{87}\text{Sr}/^{86}\text{Sr}$	2 $\sigma$	$I_{\text{Sr}}(\text{TMa})$	Sm	Nd	$^{147}\text{Sm}/^{144}\text{Nd}$	$^{143}\text{Nd}/^{144}\text{Nd}$	2 $\sigma$	$f_{\text{Sm}/\text{Nd}}$	$^{143}\text{Nd}/^{144}\text{Nd}(t)$	$\epsilon_{\text{Nd}}(0)$	$\epsilon_{\text{Nd}}(t)$
LJ15-01	Boninite	450	1.5	494.0	0.0088	0.704924	0.000006	0.7049	1.3	4.0	0.19	0.512801	0.000005	-0.03	0.512237	-7.8	3.48
LJ15-12	Boninite	450	17.6	171.4	0.2964	0.706957	0.000004	0.7051	1.9	6.8	0.17	0.512989	0.000018	-0.13	0.512488	-2.9	8.39
LJ15-13	Boninite	450	3.1	140.4	0.0638	0.706051	0.000009	0.7056	0.9	3.2	0.18	0.512740	0.000012	-0.10	0.512220	-8.1	3.17
LJ15-14	Boninite	450	0.4	261.2	0.0043	0.704805	0.000005	0.7048	2.4	6.4	0.22	0.513127	0.000006	0.14	0.512467	-3.3	7.98
LJ15-108	Boninite	450	4.0	152.0	0.0763	0.706052	0.000007	0.7056	1.3	4.3	0.18	0.512679	0.000010	-0.09	0.512151	-9.5	1.80
12LJ-07	Boninite	450	41.3	85.9	1.3583	0.713346	0.000017	0.7046	0.9	2.9	0.18	0.512752	0.000019	-0.06	0.512209	-8.4	2.94
12LJ-09	Boninite	450	55.5	122.0	1.2838	0.712350	0.000018	0.7041	1.0	3.6	0.18	0.512772	0.000014	-0.10	0.512253	-7.5	3.80
13QLS-68	Ankaramite	450	15.2	225.8	0.1942	0.706281	0.000010	0.7050	3.7	17.4	0.13	0.512578	0.000010	-0.35	0.512200	-8.5	2.78
13QLS-70	Ankaramite	450	12.3	221.4	0.1611	0.706210	0.000006	0.7052	4.0	18.9	0.13	0.512556	0.000012	-0.36	0.512184	-8.9	2.46
LJ15-40	HMBA	450	33.5	370.8	0.2615	0.706338	0.000010	0.7047	4.4	22.2	0.12	0.512524	0.000005	-0.40	0.512175	-9.0	2.27
LJ15-42	HMBA	450	46.2	399.0	0.3347	0.706750	0.000009	0.7046	4.2	21.4	0.12	0.512461	0.000002	-0.40	0.512115	-10.2	1.11
LJ15-166	HMBA	450	17.7	651.4	0.0784	0.705760	0.000007	0.7053	3.9	16.8	0.14	0.512522	0.000003	-0.28	0.512107	-10.4	0.95
16LJ-27	HMBA	450	15.3	458.6	0.0967	0.705711	0.000007	0.7051	2.4	10.4	0.14	0.512531	0.000003	-0.28	0.512113	-10.2	1.07
13QLS-100	HAA	450	23.4	1154.2	0.0586	0.705336	0.000007	0.7050	3.6	17.5	0.12	0.512565	0.000003	-0.37	0.512197	-8.6	2.70
13QLS-103	HAA	450	74.1	569.6	0.3759	0.707711	0.000006	0.7053	3.3	15.3	0.13	0.512526	0.000002	-0.34	0.512145	-9.6	1.69
LJ15-53	Sanukite	450	63.7	498.0	0.3695	0.709438	0.000006	0.7071	4.6	25.7	0.11	0.512086	0.000003	-0.45	0.511769	-17.0	-5.66
LJ15-54	Sanukite	450	79.0	432.4	0.5284	0.710103	0.000008	0.7067	4.1	24.9	0.10	0.512244	0.000007	-0.50	0.511952	-13.4	-2.07
16LJ-55	Sanukite	450	39.8	388.4	0.2965	0.709206	0.000008	0.7073	4.4	25.2	0.10	0.512180	0.000005	-0.47	0.511871	-15.0	-3.66
16LJ-69	Sanukite	450	31.4	257.8	0.3516	0.708843	0.000007	0.7066	3.5	19.7	0.11	0.512170	0.000003	-0.46	0.511857	-15.2	-3.94
12LJ13	Sanukite	450	63.5	283.2	0.6335	0.710690	0.000017	0.7066	4.5	27.5	0.10	0.512174	0.000014	-0.48	0.511871	-15.0	-3.66
12LJ15	Sanukite	450	61.0	264.2	0.6524	0.710295	0.000018	0.7061	4.4	25.0	0.11	0.512215	0.000012	-0.43	0.511884	-14.7	-3.39
LJ15-76	Sediments	450	97.4	106.3	2.6487	0.726746	0.000006	0.7098	3.7	19.9	0.11	0.512045	0.000002	-0.43	0.511714	-18.0	-6.73
LJ15-77	Sediments	450	112.8	234.0	1.3937	0.718771	0.000006	0.7098	5.1	28.0	0.11	0.512004	0.000006	-0.44	0.511679	-18.7	-7.40

Note:

(1)  $I_{\text{Sr}} = {}^{87}\text{Sr}/{}^{86}\text{Sr} - {}^{87}\text{Rb}/{}^{86}\text{Sr} \times (e^{\lambda_{\text{Rb}}t} - 1)$ , where  $\lambda_{\text{Rb}} = 1.3972 \times 10^{-11} \text{ year}^{-1}$  (IUPAC; Villa et al., 2015);(2)  $\epsilon_{\text{Nd}}(t) = \{({}^{143}\text{Nd}/{}^{144}\text{Nd} - {}^{147}\text{Sm}/{}^{144}\text{Nd} \times (e^{\lambda_{\text{Sm}}t} - 1)) / ({}^{143}\text{Nd}/{}^{144}\text{Nd})_{\text{CHUR}} - ({}^{147}\text{Sm}/{}^{144}\text{Nd})_{\text{CHUR}} \times (e^{\lambda_{\text{Sm}}t} - 1)\} \times 10,000$ , where  $\lambda_{\text{Sm}} = 6.54 \times 10^{-12} \text{ year}^{-1}$ ;  $({}^{143}\text{Nd}/{}^{144}\text{Nd})_{\text{CHUR}} = 0.512638$ ;  $({}^{147}\text{Sm}/{}^{144}\text{Nd})_{\text{CHUR}} = 0.1967$  (Jacobsen & Wasserburg, 1984);

(3) HMBA=High-Mg basaltic andesite; HAA=High-Al andesite

Table 4: In situ zircon O isotopic data for the Lajishan-Yongjing island arc volcanics

Sample	$O^{16}/O^{18}_{Mean}$	$d^{18}O (‰)_{ZIR}$	$\pm 2s$	$d^{18}O (‰)_{WR}$	$\pm 2s$
LJ15-01@1	0.002023	6.97	0.13	7.84	0.13
LJ15-01@2	0.002022	6.70	0.14	7.58	0.14
LJ15-01@3	0.002024	7.47	0.14	8.34	0.14
J15-01@4	0.002023	7.20	0.15	8.08	0.15
LJ15-01@5	0.002019	5.82	0.17	6.69	0.17
LJ15-01@6	0.002018	4.66	0.26	5.53	0.26
LJ15-01@7	0.002024	7.61	0.17	8.49	0.17
LJ15-01@8	0.002026	8.63	0.14	9.50	0.14
LJ15-01@9	0.002023	7.35	0.14	8.22	0.14
LJ15-01@10	0.002024	7.59	0.21	8.46	0.21
LJ15-01@11	0.002023	7.20	0.27	8.08	0.27
LJ15-01@12	0.002023	7.13	0.19	8.00	0.19
LJ15-01@13	0.002023	7.06	0.20	7.93	0.20
LJ15-01@14	0.002022	6.57	0.31	7.44	0.31
LJ15-01@15	0.002023	7.09	0.16	7.97	0.16
LJ15-01@16	0.002024	7.43	0.21	8.30	0.21
LJ15-01@17	0.002023	7.17	0.16	8.04	0.16
LJ15-01@18	0.002023	7.22	0.19	8.09	0.19
LJ15-01@19	0.002023	6.96	0.16	7.84	0.16
LJ15-01@20	0.002023	7.21	0.15	8.08	0.15
LJ15-70@1	0.002019	5.73	0.12	6.56	0.12
LJ15-70@2	0.002021	6.85	0.18	7.68	0.18
LJ15-70@3	0.002015	3.86	0.35	4.68	0.35
LJ15-70@4	0.002026	9.33	0.20	10.16	0.20
LJ15-70@5	0.002020	6.04	0.09	6.86	0.09
LJ15-70@6	0.002020	5.96	0.21	6.79	0.21
LJ15-70@7	0.002018	5.40	0.19	6.23	0.19
LJ15-70@8	0.002019	5.74	0.26	6.57	0.26
LJ15-70@9	0.002020	6.09	0.21	6.92	0.21
LJ15-70@10	0.002019	5.74	0.19	6.57	0.19
LJ15-70@11	0.002019	5.77	0.12	6.60	0.12
LJ15-70@12	0.002019	5.61	0.18	6.44	0.18
LJ15-70@13	0.002016	4.16	0.26	4.98	0.26
LJ15-70@14	0.002019	5.81	0.14	6.64	0.14
LJ15-70@15	0.002019	5.88	0.22	6.71	0.22
LJ15-70@16	0.002020	6.04	0.08	6.87	0.08
LJ15-70@17	0.002020	5.96	0.17	6.79	0.17
LJ15-70@18	0.002020	6.02	0.19	6.85	0.19
LJ15-70@19	0.002020	6.00	0.28	6.83	0.28
LJ15-70@20	0.002019	5.81	0.25	6.64	0.25
LJ15-70@21	0.002020	6.24	0.20	7.06	0.20
LJ15-70@22	0.002019	5.80	0.20	6.63	0.20

Note:  $\delta^{18}O_{WR} = \delta^{18}O_{Zir} + 0.0612 (wt. \% SiO_2) - 2.5$  (Valley et al., 2005)